BATCH REACTORS FOR SCALABLE HYDROGEN PRODUCTION

A Dissertation
Presented to
The Academic Faculty

by

David Lee Damm

In Partial Fulfillment
Of the Requirements for the Degree
Doctor of Philosophy in the
School of Mechanical Engineering

Georgia Institute of Technology

August 2008

BATCH REACTORS FOR SCALABLE HYDROGEN PRODUCTION

Approved by:

Dr. Andrei G. Fedorov, Advisor
School of Mechanical Engineering
Georgia Institute of Technology

Dr. Srinivas Garimella
School of Mechanical Engineering
Georgia Institute of Technology

Dr. William J. Koros
School of Chemical & Biomolecular Engineering
Georgia Institute of Technology

Dr. William J. Wepfer
School of Mechanical Engineering
Georgia Institute of Technology

Dr. Timothy C. Lieuwen
School of Aerospace Engineering
Georgia Institute of Technology

Date Approved: July 6, 2008

The acquisition of any knowledge is always of use to the intellect, because it may thus drive out useless things and retain the good. For nothing can be loved or hated unless it is first known.

-Leonardo da Vinci

ACKNOWLEDGEMENTS

I would like to acknowledge the support and guidance of my advisor, Dr. Andrei Fedorov, throughout both this project and my graduate career. He has been an inspiration, mentor, and friend.

Financial support for this project was provided by the Department of Defense through the National Defense Science and Engineering Graduate (NDSEG) fellowship program, and by the Georgia Institute of Technology through a “Creating Energy Options” grant.

TABLE OF CONTENTS

LIST OF TABLES

LIST OF FIGURES

SUMMARY

A novel batch reactor concept is proposed for the catalytic production of hydrogen in distributed and portable applications. In the proposed CHAMP (CO_2/H_2 Active Membrane Piston) reactor, a batch of hydrocarbon or synthetic fuel is held in the reaction chamber where it reacts, or breaks apart, producing hydrogen. Simultaneously, the hydrogen is separated from the mixture by permeation through an integrated selective membrane. These processes proceed to the desired level of completion at which point the reaction chamber is exhausted and a fresh batch of fuel mixture brought in. Unique to the CHAMP reactor is the ability to precisely control the residence time, as well as the ability to compress the reaction chamber dynamically, or mid-cycle, in order to increase the instantaneous hydrogen yield rate.

Reactor models were developed in order to study the performance characteristics and optimize the design and operation of the CHAMP reactor. First, the ideal limits of performance (in the absence of transport limitations) were contrasted with those for continuous flow designs. Then, a coupled transport-kinetics model is employed to quantify the effects of mass transport limitations on reactor performance and search the design parameter space for optimal points. Two modes of operation are studied: fixed-volume mode wherein the piston is stationary and constant-pressure mode in which the rate of compression matches the permeation of hydrogen through the membrane. Finally, to validate these numerical models and confirm the understanding of the key operating principles, test reactors were built and experimentally characterized.

CHAPTER 1

INTRODUCTION

Hydrogen is an attractive fuel for portable and distributed power plants, be they hydrogen-fed internal combustion engines [1] or vehicular or residential fuel cells [2], because of its high energy density per molecule and environmentally benign reaction products (water). Hydrogen made from carbon-neutral energy sources [3-7], or with centralized CO_2 sequestration [8,9] could be an important pathway to mitigation of distributed CO_2 emissions. Additionally, the high theoretical efficiency of fuel cells has potential to improve energy utilization [10-12]. However, the existing technical barriers to onboard hydrogen storage [13] provide motivation to use a high volumetric density (i.e., liquid) energy carrier that is efficient to store, easy to transport, and convenient to refuel the vehicle. For instance in military and space applications, energy-dense onboard power supply systems that meet stringent weight, volume, and power criteria are highly prized—both figuratively and literally (e.g. the recent $1 million DoD "wearable power" contest [14]).

Distributed power applications such as automobiles, generators, and certain industrial processes make up a very large component of the energy consumption and CO_2 emissions globally [15]. In a conceptual analysis, Damm & Fedorov [16] proposed the concept of a sustainable carbon economy as a solution for the mitigation of greenhouse gas, CO_2, emissions from this sector (see Appendix A). In the proposed framework liquid fuels would be processed locally to produce hydrogen for use in the power plant, while simultaneously the byproduct carbon dioxide would be captured rather than emitted to the atmosphere. Such a system would 1) provide a feasible near-term solution via

collection and sequestration of CO_2 in permanent repositories, as well as, 2) potentially enable a long-term sustainable energy future by carrying primary renewable energy in the form of a synthetic liquid fuel for use in transportation/distributed applications. A key enabling component of this system is the onboard or onsite fuel reformer which takes a liquid hydrocarbon or synthetic fuel and converts it into hydrogen for subsequent use in the power plant without dilution of the CO_2 exhaust stream. Therefore, development of a fuel processor for production of hydrogen at relatively small-scales (<100kW) is the subject of the present work.

I begin in Chapter 2 by reviewing the state-of-the-art in small-scale catalytic production of hydrogen, which has proven to be much more problematic than simple miniaturization of mature, industrial-scale technologies. The difficulties are, arguably, fundamental in nature, including 1) poor utilization of the fuel, catalyst, and active membrane surface area, due to disparate process timescales, 2) the inability to manage transport losses in sequential, uni-functional, and shrinking components, and 3) mismatch between transient power demand and the steady-state, continuous-flow fuel processor. Having established this background to the problem in Chapter 2, I proceed, in Chapter 3, to propose a novel reactor concept which operates in a fundamentally different manner than the traditional steady, continuous flow systems.

CHAMP ($\underline{C}O_2/\underline{H}_2$ $\underline{A}$ctive $\underline{M}$embrane $\underline{P}$iston) technology [17] is a novel concept which enables precise control of reaction conditions leading to an enhanced rate of hydrogen production (fuel for the power plant) and an enriched CO_2 (greenhouse pollutant) exhaust stream amenable to capture. In the proposed reactor, a discrete amount or batch of fuel mixture is brought into the reaction chamber and held there as long as

necessary to achieve the desired performance targets. As the mixture is held there, reactor conditions are dynamically controlled to ensure that 1) *reaction* conditions are optimal, thereby maintaining an elevated reaction rate even as fuel is consumed, and 2) conditions are favorable for *separation* of reaction products (either H_2, or CO_2, or both) through the integrated, selectively-permeable membrane(s). When both reaction and separation have reached a desired level of completion, the remaining mixture is exhausted out of the reaction chamber, and a fresh batch of fuel is brought in. Several embodiments and methods of operation are presented in Chapter 3 as well as supporting equilibrium calculations for membrane-integrated reactors and a regenerative processing scheme that results in 100% fuel utilization or conversion to hydrogen.

Among the many configurations discussed in Chapter 3, the simplest embodiment of the CHAMP concept is a piston-in-cylinder configuration, which lends itself well to an in-depth study of the design, operation, and performance of this class of reactors. In Chapter 4, idealized kinetic reactor models, neglecting heat and mass transfer limitations, allow the ideal limits of performance to be calculated and contrasted with continuous-flow (CF) designs [18]. In addition to the fundamental performance aspects, several practical features are linked to the capability to dynamically control the reactor volume, mid-cycle if necessary, to favorably enhance the hydrogen production rate.

Having thus placed the CHAMP reactor in context, relative to its CF competition, a detailed, coupled, transport-kinetics model is developed and analyzed in Chapter 5. This 1-D model is computationally-efficient enough to allow a parametric study of the reactor operating space. The analysis shows the effects of various geometric and system design parameters on the rate limiting step for achieving maximum hydrogen output.

Understanding the limiting processes and transitions from one to another, is a pre-requisite for optimizing the design and operation of a real reactor.

Finally, to validate the modeling and analysis, and to demonstrate its practical operation, I report in Chapter 6 on the experimental characterization of a test-rig reactor that was built and tested. Two very different sets of experiments were conducted; the first provided snapshots of the contents of the reactor at various times throughout a cycle, and the second provided continuous measurements of hydrogen output (separated through the membrane) over the course of operation of a cycle. These data sets validate the understanding of the key operating principles of the reactor, as well as verify the adequacy of the developed model for correctly coupling the multiple interacting physical processes to accurately predict the hydrogen yield.

In light of the conceptual development, modeling, and experimental work reported here, I conclude this thesis with Chapter 7 by outlining the recommended directions of future efforts and defining the areas requiring further development.

CHAPTER 2

STATE-OF-THE-ART IN FUEL PROCESSING

2.1 Overview of catalytic hydrogen production

Production of hydrogen by processing of carbon based fuels (either naturally occurring or synthetic) at relatively small-scales (<100kW) has been the subject of a growing number of studies in recent years. The fuels receiving the most attention are usually methane, methanol, ethanol, and gasoline. The most commonly studied methods for catalytic processing of fuel to produce hydrogen are partial oxidation, steam reforming, and autothermal reforming. While all of these fuels and processing schemes have well-documented advantages and disadvantages [12,19-23], the added constraint of capturing the byproduct CO_2, rather than exhausting it to the atmosphere, makes steam reforming of methanol particularly attractive for automotive, mobile, or distributed applications [16,24]. This is because methanol contains a relatively high hydrogen/carbon ratio, the reaction can be carried out at fairly low temperatures over readily available catalysts, and after separation or utilization of hydrogen, the reformate stream is highly enriched in CO_2 and amenable to capture.

In the proposed system [16], methanol would be synthesized from recycled CO_2 using renewable primary energy inputs. However, in the near term, methanol is readily available from commercial manufacturers and the existing supply infrastructure could be expanded. Although well-to-wheels analysis of a methanol-based transportation system (e.g. [10-12]) does not show it to be the most efficient alternative to petroleum, it is attractive for applications where capture of the byproduct CO_2 is a concern (not only in

transportation). Therefore, this thesis is primarily focused on steam reforming of methanol as a means for producing hydrogen at the point of use.

2.2 Steam reforming of methanol

The steam reforming of methanol (first reported in 1921 by Christiansen [25]) produces hydrogen via the endothermic reaction:

$$CH_3OH + H_2O \rightleftharpoons 3H_2 + CO_2 \qquad \Delta H = 49.2 \quad kJ/mol \tag{2.1}$$

This typically occurs over copper and zinc oxide-based catalysts ($Cu/ZnO/Al_2O_3$) at moderate temperature (200 – 300 °C) and pressure (near ambient). These conditions and catalysts also favor methanol decomposition:

$$CH_3OH \rightleftharpoons 2H_2 + CO \qquad \Delta H = 90.4 \quad kJ/mol \tag{2.2}$$

albeit at a much slower rate. The concentration of carbon monoxide in the product stream is influenced heavily by the reversible water gas shift reaction:

$$CO + H_2O \rightleftharpoons H_2 + CO_2 \qquad \Delta H = -41.2 \quad kJ/mol \tag{2.3}$$

and can be of major concern, especially in PEM fuel cells which require CO < 10 ppm [26,27].

At these elevated temperatures the endothermic, reverse WGS reaction [Eq. (2.3)] causes the equilibrium CO concentration in the product mixture to be too high (1 - 4%) for the PEM fuel cells to tolerate. One approach to address this problem is the use of a second reactor stage, which is designed to operate at lower temperature (100 – 150 °C) over a catalyst that favors the conversion of CO into CO_2 via the WGS reaction, followed by a third stage to preferentially oxidize the CO to acceptable levels. Alternatively, the hydrogen can be purified by separation via a hydrogen selective membrane—either as an additional processing step in a separate unit, or integrated into the reactor. Finally, after

cleanup or membrane separation, the purified hydrogen is sent to the fuel cell or internal combustion engine or a gas turbine where it is consumed to produce electrical or mechanical power.

2.3 Continuous flow reactor technology

Technology for large scale steam reforming of methanol is quite mature and most reactors are of the fixed catalyst bed type, operated in a steady-state, continuous-flow regime. In a typical configuration [28], fuel mixture is fed into a heated bed of catalyst pellets and the residence time of the fuel in the reactor (controlled by adjusting the flowrate) is made sufficiently long to ensure a high level of conversion of fuel into products. The reactor design is usually optimized to maximize the gas hourly space velocity (GHSV), or throughput, while minimizing the pressure drop (pumping power). To meet these criteria, relatively large catalyst pellets with low effectiveness factors (typically 0.001- 0.01 according to [28]) are used, and as a result the reaction is heat and mass transfer limited, with large temperature gradients throughout because of the strongly endothermic nature of the reaction and poor effective thermal conductivity of the packed bed. Because these reactors are designed for optimal operation at steady-state, they usually require very long start-up or shut-down time and have a very narrow range of optimal fuel flow rates. The nature of the design trade-offs and fundamental performance limitations characteristic to these large scale systems do not change significantly as the systems are miniaturized. At the same time, the relative impacts of system inefficiencies and losses, which often scale with surface area to volume ratio, become more pronounced as the size of the system shrinks.

Particularly in mobile applications, where size and weight considerations are of utmost importance, the catalyst must be used effectively and reactor volume must be minimized, while still maintaining high levels of fuel utilization, sufficient power output, and efficient operation. Additionally, rapid transients, and efficient operation across a wide power range is required. Sequential processes carried out in uni-functional components must be avoided because this contributes to excessive balance-of-plant weight, volume, and transport losses. These special requirements have so far resulted in the failure of efforts to miniaturize industrial-scale fuel processors for small-scale applications (particularly for transportation). However, these failures have encouraged research into multiple variations on the traditional packed bed design, such as microchannel reactors with wall-coated catalysts [29-33], and plate-fin or heat exchanger type reactors with excellent heat transfer characteristics [34-38]. System integration and design of multi-functional components has also received much attention, particularly "membrane reactors" which integrate selectively-permeable membranes into the reaction chamber for simultaneous reaction enhancement and product separation/purification [26,39-44].

2.4 Membrane reactors

The key operating principle of a membrane reactor is to enhance the reaction rate and shift the reaction equilibrium in a favorable direction by selectively removing reaction product(s) from the reaction chamber via permeation through a membrane [20]. In the case of steam reforming of methanol for fuel cell applications, hydrogen removal not only improves the reaction yield but also provides an enriched (or purified) hydrogen stream for use in the fuel cell. Various types of hydrogen-selective membranes [20,45-

48] are suitable for use in membrane reactors including microporous alumina (high permeability, poor selectivity), zeolites (moderate permeability and selectivity), perovskites (low permeability, high selectivity), and dense metallic membranes (relatively high permeability, and potentially infinite selectivity). The material selection and design of the membrane must be such that it is mechanically robust, provides sufficient permeability and selectivity, with minimal pressure drop across the membrane, maximum active surface area for permeation, and minimal degradation of performance under reaction conditions. Palladium and palladium alloy membranes [49-51] provide many of these characteristics (including infinite selectivity to hydrogen), and are a promising (although expensive) technology for use in onboard hydrogen generating membrane reactors.

These recent innovations notwithstanding, the "tradeoff between reactor size and fuel utilization" [52] has remained a fundamental barrier to sizing a fuel reformer for transportation applications where both size and efficiency requirements are very strict. Figure 2.1 is a highly typical example from the literature [39] that shows methanol conversion vs. time factor for traditional reactors (TR) and membrane reactors (MR) at several temperatures. While conversion is certainly improved in the membrane reactor, the ideal conversion is still only approached asymptotically—with the practical implication that incremental improvements in fuel utilization come at the expense of greatly diminished specific power. Therefore, I conclude that even though advanced reactor designs, such as membrane reactors, are pushing the performance limits further than ever, the old paradigm still dictates that "one must sacrifice productivity [power] to achieve higher hydrogen yield [efficiency] and vice-versa" [52].

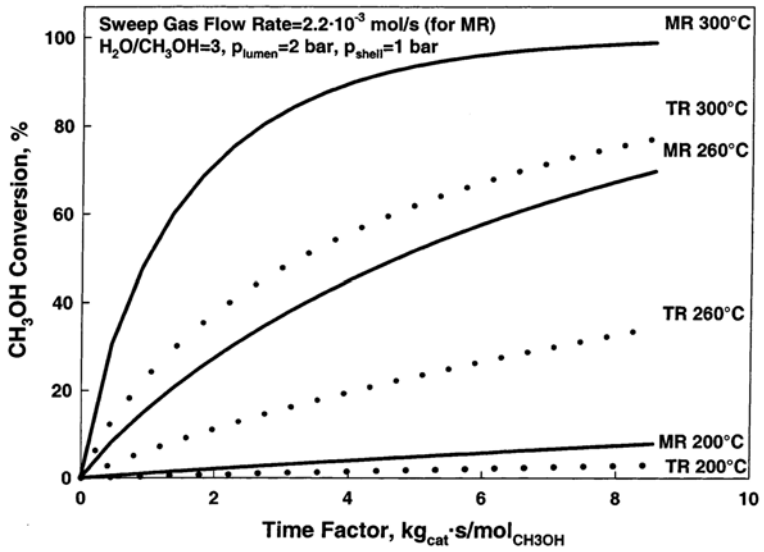

Figure 2.1. Methanol conversion vs. time factor for various operating temperatures (MR-membrane reactor, TR-traditional reactor, reproduced from [39]).

2.5 Unsteady-state reactors

Forced, unsteady-state operation (FUSO) of reactors is an approach that has been studied for many years [53,54] because, in principle, it avoids many of the limitations mentioned above that are consequences of steady-state operation. For example, Kaisare et al. [55-57], studied a reverse-flow reactor for autothermal reforming of methane. The direction of flow through the reactor channel was alternated at a frequency that exploited the mismatch between characteristic time scales for flow, reaction, and heat and mass transport. Significant improvements in hydrogen yield and thermal management were demonstrated, with the only added expense being that of more complicated external process controls and a periodic or unsteady product stream.

An underlying principle of FUSO operation is that rather than forcing the system to operate in a continuous-flow manner (simply for the sake of achieving steady-state operation), the flowrate, direction of flow, temperature, and pressure can be manipulated

to keep the mixture under optimal process conditions at all times and at every location within the reactor. Building on this principle, a new class of reactors—transient batch reactors for hydrogen generation—which extends the concept of FUSO to its logical conclusion has been developed.

Batch reactors can be seen as an opposite to the CF reactors. However, upon closer examination of ideas underlying unsteady-flow reactors, the batch reactor can be viewed as an extension of the FUSO concept. In this thesis, I examine these ideas on an example of the catalytic production of hydrogen in a novel batchwise-operated membrane reactor. Strictly speaking, a batch membrane reactor is not a closed system due to the removal of reaction products. However, the mode of operation is batchwise (rather than continuous flow), therefore it will be referred to in this thesis as a "batch" reactor. After a brief discussion in Chapter 3 of the conceptual design and operation, I formulate a simplified mathematical model for determining the ideal limits of batch reactor performance, and compare and contrast these results with a comparable continuous-flow reactor.

CHAPTER 3

CHAMP REACTION TECHNOLOGY

3.1 Motivation for batch reactors

Conceptually, the ideal batch (membrane) reactor takes in the reactant mixture, maintains the mixture at ideal conditions for reaction and selective-permeation to take place, and after a desired amount of time, expels the unwanted byproducts. The reactor should hold the fuel in intimate contact with the catalyst at the prescribed temperature and pressure. Simultaneously, permeation of the desired product (hydrogen) through the membrane shifts the reaction equilibrium towards more products (higher conversion) while providing a purified product stream. As fuel begins to be depleted, the rate of hydrogen production slows down, and as hydrogen is removed from the reaction mixture via separation, the rate of permeation also decreases. As this occurs, timely compression of the reaction chamber can be used to increase the concentration of remaining fuel and hydrogen, providing an additional driving force for both the reaction and permeation processes. Thus the productivity of the reactor is maintained at an elevated level for more rapid completion of the cycle. Once a sufficient amount of hydrogen has been produced and separated (relative to the ideal limit) the cycle is complete and the reactor is ready for discharge and replenishment. The remaining unseparated mixture is enriched with byproduct CO_2 which can be removed and stored, allowing the balance of the exhaust stream to be recycled back in with the fuel intake [16]. CHAMP ($\underline{C}O_2/\underline{H}_2$ $\underline{a}$ctive $\underline{m}$embrane $\underline{p}$iston) reactor technology is an embodiment of this concept [17]. To illustrate the design, operation, and ideal performance characteristics of transient batch reactors I

describe several CHAMP reactor configurations and analyze the most basic one using steam reforming of methanol as an example.

3.2 Baseline embodiment of the CHAMP concept

A basic embodiment defining the most important principles underlying the CHAMP reactor concept is the piston-in-cylinder configuration shown in Figure 3.1. The space between the top of the piston and the cap of the cylinder forms the reaction chamber and its volume is controlled by moving the piston. On the face of the piston is a thin, porous catalyst coating, and in the cap of the cylinder is a selective membrane for hydrogen separation. The reactor operates on a multi-stroke cycle. The piston starts at the top and moves down, drawing in fresh reactants through an intake valve. The intake valve closes and the reaction proceeds forward upon reagent contact with the catalyst layer with simultaneous removal of hydrogen through the permeable membrane. As the reaction is close to completion and reactants become depleted, the piston moves up, compressing the mixture, increasing the reaction and permeation rates. Once the reaction and permeation are sufficiently complete, the exhaust valve is opened and the piston pushes the remaining mixture (mainly pre-concentrated CO_2) out of the chamber.

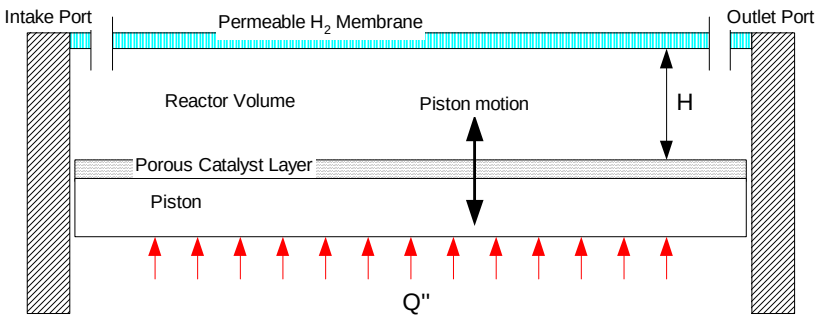

Figure 3.1. Piston/cylinder configuration of the CHAMP reactor

3.3 Additional embodiments

While this simple design is useful for the fundamental analysis of the reactor operation and performance, it is not the only possible configuration or necessarily the most practical one. Several configurations and their corresponding methods of operation are described below.

3.3.1 Piston/Cylinder Assembly

Here, the cylinder (Figure 3.2) features a high aspect ratio and sufficient mechanical strength to withstand operating pressures and temperatures. The cylinder interior walls are coated with a mixture or a layered structure of catalysts appropriate for the fuel reforming reaction at the optimal temperature and for the water gas shift (WGS) reaction at lower temperatures (100 - 150 °C). The critical dimension of the cylinder, the slit thickness (A), is made small enough to ensure that diffusive gas phase species transport from the bulk to the catalyst walls is as fast as possible. The high aspect ratio design also results in a very high specific (per unit volume of the reactor) surface area of the catalyst, thus maximizing the power density (and throughput per unit volume) of the reactor.

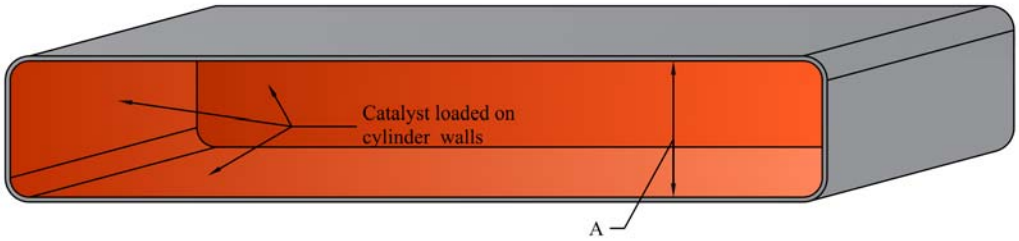

Figure 3.2 High aspect ratio cylinder (reaction chamber).

The piston (Figure 3.3) fits snugly into the cylinder and is constructed of a porous material with sufficient mechanical strength and durability at expected operating

temperatures and pressures. The exterior walls of the piston including its face are encased in highly selective and thin (~*μm* scale) CO_2/H_2 permeable membrane, which is not permeable to CO or H_2O. (See US Patent #6,099,621 and ref. [26] for examples of a CO_2 and H_2 selective membrane, and refs. [58-60] for description and application of H_2 selective membranes.) On the exterior of the piston there may also be a network of very small, communicating gas flow channels or grooves (shown straight in Figure 3.3 for illustration purposes only) in order to enhance the mixture contact area with the piston membrane for selective removal of the CO_2 and H_2 from the reacting mixture during each reaction step. Within the piston are flow channels to provide efficient removal of the permeate.

The assembled piston and cylinder form two distinct reactor domains and pathways for the reactions to take place. The first is the bulk reaction chamber which is the volume between the face of the piston and the "top" (intake end) of the cylinder. Here, the reaction mixture interacts intimately with the catalyst on the cylinder walls and with the CO_2/H_2 selective membrane covering the face of the piston. The second domain is the network of the flow microchannels formed by the cylinder walls and the micro grooves on the piston. Reaction mixture flowing through these channels is simultaneously exposed to catalyst on the inside of the cylinder wall and the CO_2/H_2 selectively permeable membrane on the exterior surface of the piston.

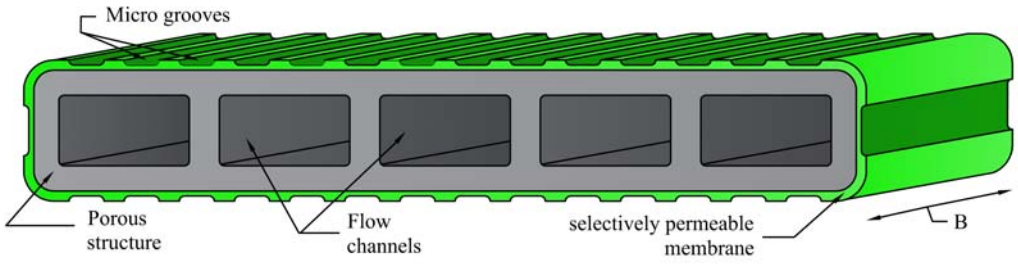

Figure 3.3 Membrane piston (cutaway view) composed of a porous substrate coated with a H_2/CO_2 selective membrane. The piston is closed at one end, seeing the "bulk" reaction chamber, and open at the other end where the desired reaction products are collected.

CO_2 + H_2 selective membrane integrated with the piston

Stroke 1: Intake

The first stroke (Figure 3.4) fills the reaction chamber (cylinder) with a methanol and water vapor mixture. Ideally, the water/carbon ratio of the mixture is unity, but in practice this ratio needs to be optimized for various operating conditions. The walls of the reaction chamber are loaded with a catalyst or a mixture of catalysts that are highly active for fuel reforming/decomposition at intermediate temperatures (e.g., ~250 °C for methanol) and water gas shift (WGS) reaction at lower temperatures (~ 120 °C). During this stroke, both valves are open.

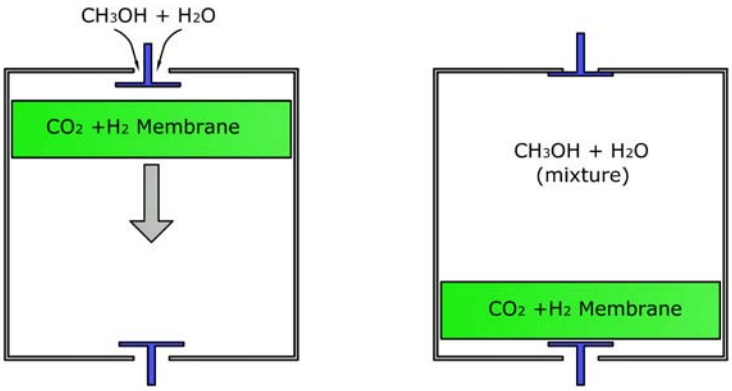

Figure 3.4 Intake stroke: the reaction chamber is filled with fuel/water vapor mixture.

Stroke 2: Compression

With both valves closed, the piston starts at the bottom (Figure 4.5) and moves up, compressing the mixture. Compression of the mixture raises the temperature, which is favorable for the endothermic steam reforming and decomposition reactions [Eqs. (2.1)

and (2.2)]. If needed, heat may be added to maintain the optimal operating temperature. High pressure in the reaction chamber forces permeation of H_2 and CO_2 through the selectively-permeable membrane integrated with the piston, and these products are collected on the backside of the piston. Since the piston motion is controlled, the speed of the compression process can be made to match the rate of permeation to achieve enhanced yield.

A portion of the mixture that has not had sufficient time to react in the "bulk" reaction domain of the cylinder (above the piston) has a route for passage around the edges of the piston via the network of microchannels (see Figure 3.2) where it remains in contact with the cylinder wall-deposited catalyst and thus further converted to products. Simultaneously, H_2 and CO_2 are separated from the mixture as they are being produced in the microchannels by permeation through the membrane into the part of the cylinder where H_2 and CO_2 are being collected. Because the reactions are endothermic, temperature will gradually decrease in the flow direction (opposite to the direction of the piston motion). At these lower temperatures, the thermodynamic conditions become favorable for the WGS reaction to proceed at a significant rate. This results in further generation of hydrogen and conversion of CO into CO_2. Taking advantage of simultaneous removal of H_2 and CO_2 from the mixture, the reaction equilibrium is shifted and enhanced conversion of CO into CO_2 is achieved. At the outlet of the microchannel network only residual amounts of H_2 and CO_2 that did not permeate across the membrane remain.

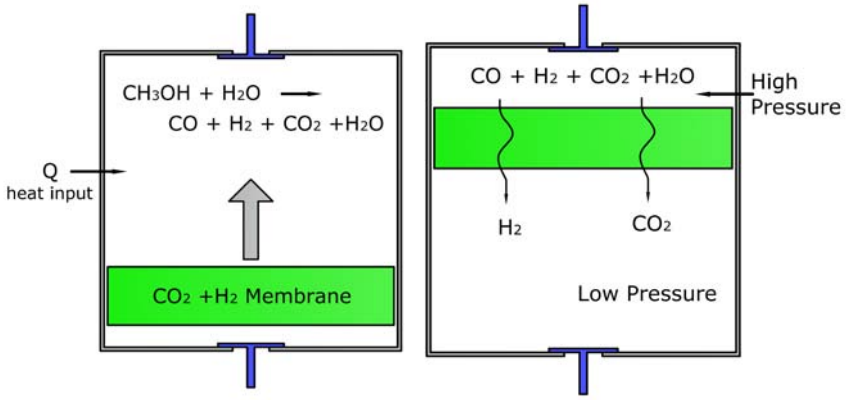

Figure 3.5 Compression stroke: as fuel decomposition proceeds, H_2 and CO_2 are produced and immediately removed through the selective membrane, shifting the reaction equilibrium towards the desired products.

Stroke 3: Expansion

With the piston near the top of the cylinder and a pure mixture of H_2 and CO_2 at the backside of the piston, the bottom valve is opened (Figure 3.6) and the piston moves down. The H_2+CO_2 mixture is pushed out through the valve to a collection chamber or directly to the fuel cell. The bottom part of the cylinder is structurally designed in such a way that it can accommodate the topography of the piston's hollow-structure with minimal dead volume present when the piston reaches the end of the expansion stroke. Further, the expansion of the remaining mixture in the reaction chamber (above the piston) lowers the temperature to approximately 120 °C. This is a thermodynamically favorable condition for the water gas shift (WGS) reaction which is exothermic (heat releasing and therefore favored at reduced temperature). If needed the chamber could be further cooled externally to achieve the optimal temperature for the WGS reaction.

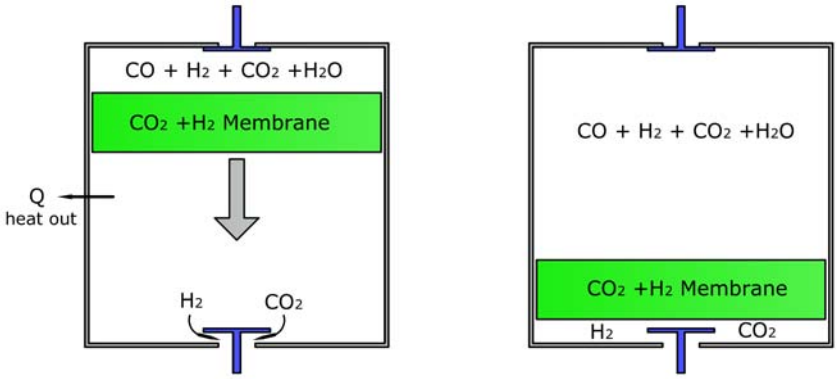

Figure 3.6 Expansion and product discharge stroke: temperature drops as the mixture expands and heat is removed, creating conditions favorable for water gas shift reaction.

Stroke 4: Final CO Cleanup

The bottom valve is closed, the piston is initially near the bottom of the cylinder, and a mixture of CO, H_2O, and residual H_2 and CO_2 is in the reaction chamber above the piston (see Figure 3.7). The piston moves up and the WGS reaction proceeds while the mixture is being compressed. The elevated pressure drives permeation of H_2 and CO_2 across the membrane shifting the equilibrium of the WGS reaction towards the desired products (i.e., from CO and H_2O to H_2 and CO_2). The compression process can be made to proceed at the optimal speed, which matches rate of permeation of products. Further, the un-reacted mixture proceeds along the path around the edges of the piston in a similar manner to that described in Stroke 2 above. When the piston reaches the top of the cylinder, all of the CO has been converted to CO_2, and all of the H_2 and CO_2 have permeated through the membrane and now reside at the backside of the piston. The system is now ready to complete the cycle (i.e. return to Stroke 1), wherein the top valve will be opened and the piston will move down, bringing in fresh reactants and sending the products (H_2 and CO_2) out to the collection chamber or directly to the fuel cell.

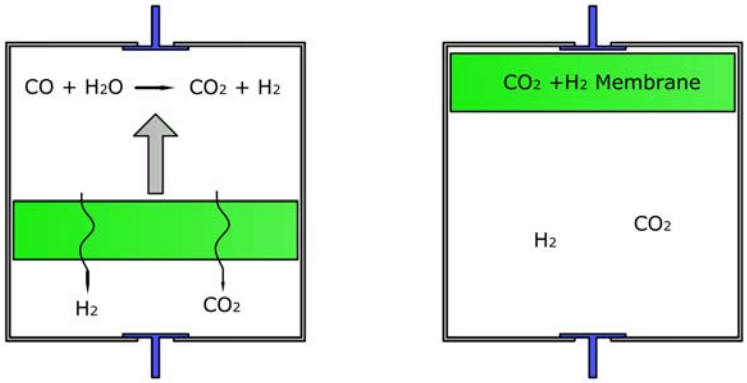

Figure 3.7 CO cleanup (via WGS) stroke: the mixture is compressed, forcing the removal of H_2 and CO_2 from the reaction chamber through the piston-integrated selective membrane, shifting the equilibrium towards the products, i.e. consumption of CO

Alternative 2-Stroke Operation

An alternative, mode of operation is a two-stroke cycle. The first stroke is the same as Stroke 1 in the 4-stroke cycle described above. The second stroke is the compression stroke, which proceeds until all of the initial reagents are converted into H_2 and CO_2 and removed from the reaction chamber of the cylinder through the piston-integrated selective membrane or around the sides of the piston through the membrane/reactor micro-channels. At the completion of the second stroke, the reaction chamber is empty and the system is ready for Stroke 1 again, wherein the H_2 and CO_2 behind the piston are discharged out to the fuel cell through the valve at the bottom of the cylinder.

H_2 selective membrane integrated with the piston

In another embodiment, the membrane piston is selectively permeable to H_2 only. The operation sequence and the cycle are very similar to that previously described for the CO_2 + H_2 selective membrane with several variations indicated in Figures 3.8 – 3.11.

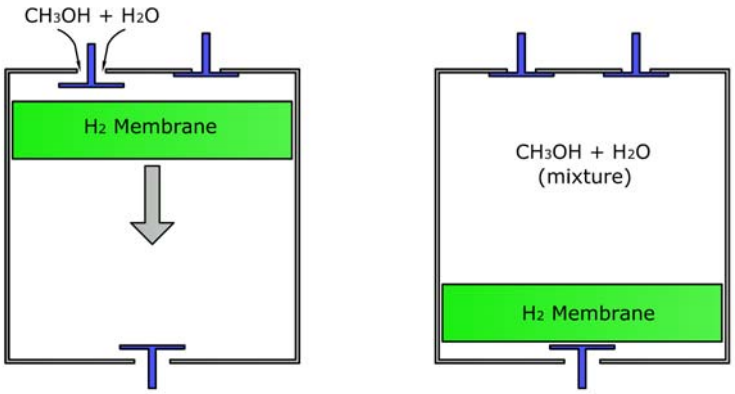

Figure 3.8 Intake stroke: the reaction chamber is filled with fuel/water vapor mixture through the intake valve. The second valve at the top of the cylinder remains closed.

In particular, during the compression stroke (Figure 3.9), only H_2 permeates the membrane, resulting in potentially pure H_2 on the backside of the piston. During the expansion stroke (Figure 3.10), pure H_2 is pushed out of the cylinder through the open valve at the bottom, either to a collection chamber or directly to the fuel cell power plant. The final CO cleanup stroke (Figure 3.11) results in conversion of CO to CO_2 via the WGS reaction and effectively separates the products as H_2 permeates the membrane and CO_2 remains at the top of the cylinder in the bulk reaction chamber. The CO_2 is pushed out of the cylinder through an open valve at the top of the cylinder (in this embodiment there are two valves at the top of the cylinder, one for intake of reactants and one for removal of CO_2). The system is ready to begin the next cycle (i.e. return to Stroke 1), wherein the top intake valve will be opened and the piston will move down, bringing in fresh reactants and sending H_2 out to the collection chamber or directly to the fuel cell.

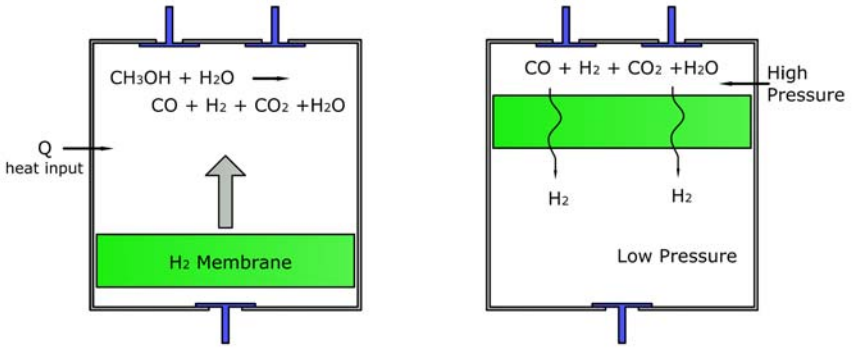

Figure 3.9 Compression stroke: as the reaction proceeds, H_2 and CO_2 are produced and H_2 is immediately removed through the membrane, shifting the reaction equilibrium towards the desired products and leading to enhanced conversion.

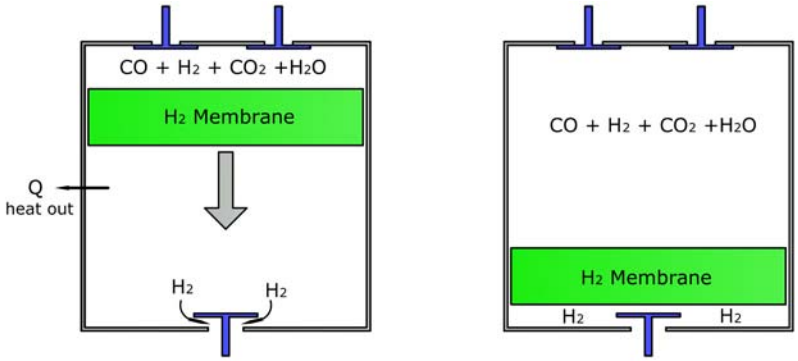

Figure 3.10 Expansion and product discharge stroke: temperature drops as the mixture expands and heat is removed, creating conditions favorable for water gas shift reaction.

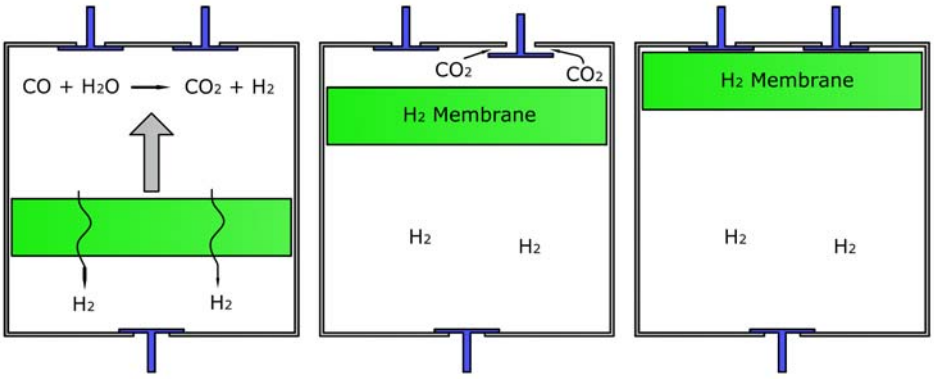

Figure 3.11 CO cleanup (via WGS) stroke: the mixture is compressed, forcing the removal of H_2 from the reaction chamber through the piston-integrated selective membrane, resulting in cleanup of CO. The remaining CO_2 in the reaction chamber is pushed out through the exhaust valve at the top of the cylinder.

CO_2 selective membrane integrated with the piston

An additional embodiment of the proposed reactor is that of a membrane piston which is permeable to mostly CO_2. The operation sequence and the cycle are identical to the case described above with the H_2 selective membrane, except that domains for CO_2 and H_2 collection are switched in Figures 3.8 - 3.11. During the compression stroke (Figure 3.9), mostly CO_2 rather than H_2 permeates the membrane, resulting in mostly CO_2 on the backside of the piston. During the expansion stroke (Figure 3.10), CO_2 is pushed out of the cylinder through the open valve at the bottom. The final CO cleanup stroke (Figure 4.11) results in conversion of CO to CO_2 (via the WGS reaction), and effectively separates the products as CO_2 permeates the membrane and H_2 remains at the top of the cylinder in the bulk reaction chamber. The H_2 is pushed out of the cylinder through an open valve at the top of the cylinder. The system is ready to begin the next cycle (i.e. return to Stroke 1), wherein the top intake valve will be opened and the piston will move down, bringing in fresh reactants and sending CO_2 out to the collection chamber for sequestration.

3.3.2 Multiple pistons and/or reaction chambers

In addition to the configurations described above, with single cylinder and single piston, additional embodiments utilize multiple pistons inside a single cylinder, multiple pistons and reaction chambers, or different cylinders for each reaction step. For example, Figure 3.12 shows a configuration with two pistons: one is selectively permeable to H_2 and another one is selectively permeable to CO_2. The pistons move in opposite directions enabling a 2 or 4 stroke cycle with reagent intake, compression, reaction, product separation, and discharge. The sequence of operations and cycle descriptions are very

similar to those described above, with minor variations depending on the configuration that is selected.

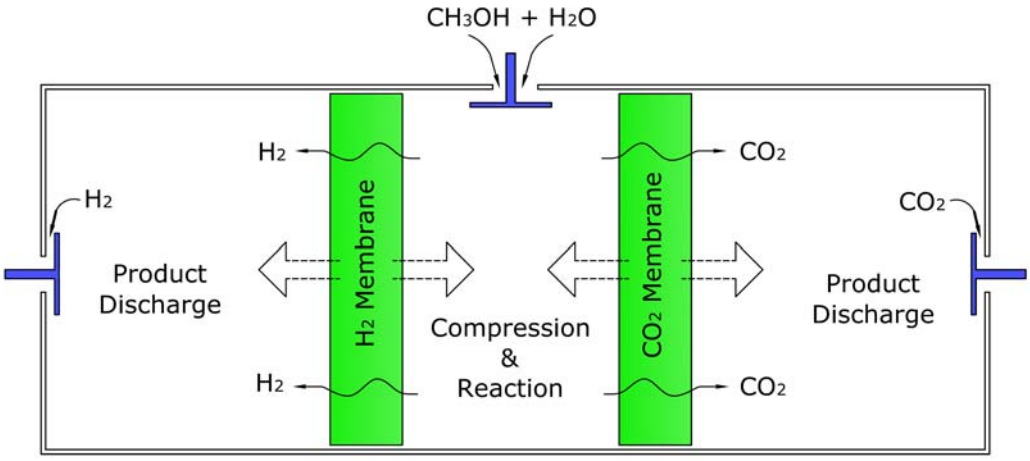

Figure 3.12 Dual piston configuration utilizing counter-directional motion of an H_2 selective membrane integrated piston and CO_2 selective membrane integrated piston inside a single cylinder

3.3.3 Flexible actuated diaphragm piston

Additionally, rather than using a piston, the reaction chamber compression could be accomplished via an actuated, flexible or "flapping" diaphragm, simplifying the sealing issues, as illustrated in Figure 3.13. In this configuration, two distinct chambers are present—one for steam reforming with a hydrogen-selective integrated membrane, and the other for water gas shift with a CO_2-selective integrated membrane. The reactors operate in two steps, 1) intake of reactants, and 2) simultaneous reaction, permeation, and compression, followed by exhaust. The two reactors can cycle in or out of phase and could be integrated into a single unit. Figure 3.14 also illustrates "regenerative" operation [16] in which the final exhaust is recycled back into the fuel stream. In this configuration 100% fuel utilization is achieved and the products are separated hydrogen and CO_2 streams.

The first design embodiment of the flexible actuated piston/diaphragm CHAMP reactor is shown in Figure 3.13. The reactor consists of two similarly designed planar high-aspect ratio chambers featuring high specific (per unit volume) surface area: a steam-reforming, hydrogen-selective membrane reactor unit (on the left in Fig. 3.13), and a water-gas-shift, CO_2-selective membrane reactor unit (on the right in Fig. 3.13). The two chambers are in fluidic communication with each other. Each unit has a flexible, externally controlled diaphragm or a piston which enables the desired operating pressure inside the chamber. The piston/diaphragm can be actuated (moved up/down) using electrostatic, electromagnetic, hydraulic, or other methods, possibly using edge-integrated bellows coupling to provide a complete seal. The internal walls of each reactor chamber and piston are coated by the catalysts which enable the specific reaction to proceed.

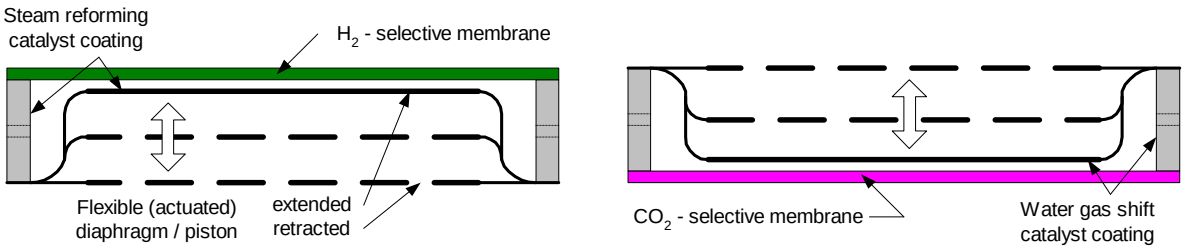

Figure 3.13 Membrane reactors for hydrogen and CO_2 production and separation.

The reactor operates in a two step repeating sequence (cycle) as shown in Figure 3.14. The first step is the intake of fuel and water by the reforming/hydrogen reaction chamber (left in Figure 3.14), and the intake of residual reforming reaction products from the WGS/CO_2 reaction chamber after completion of the previous cycle (see dashed line in Figure 3.14 showing direction of the reagent flow). The diaphragms are initially in the extended position and begin to retract drawing in the reactants. At the end of this step,

the diaphragms are in their fully retracted position, reactants are in the reaction chambers, and the respective reactions begin to proceed.

In step 2, the reactions proceed to completion as the diaphragms slowly compress the mixture at the rate required by the reaction and permeation processes. Simultaneously, hydrogen is permeating through the hydrogen selective membrane on the left, and CO_2 is permeating through the membrane on the right. The hydrogen is captured and either stored or sent directly to the power plant. The CO_2 is captured and stored until it can be properly disposed of. As the reaction and separation proceed simultaneously, the diaphragm extends as necessary compressing the mixture to maintain an increased pressure and thus enhance permeation. Finally, when the reactions and permeation processes approach the equilibrium state, the remaining products are pushed out of the chambers and the system is ready to return to the first step.

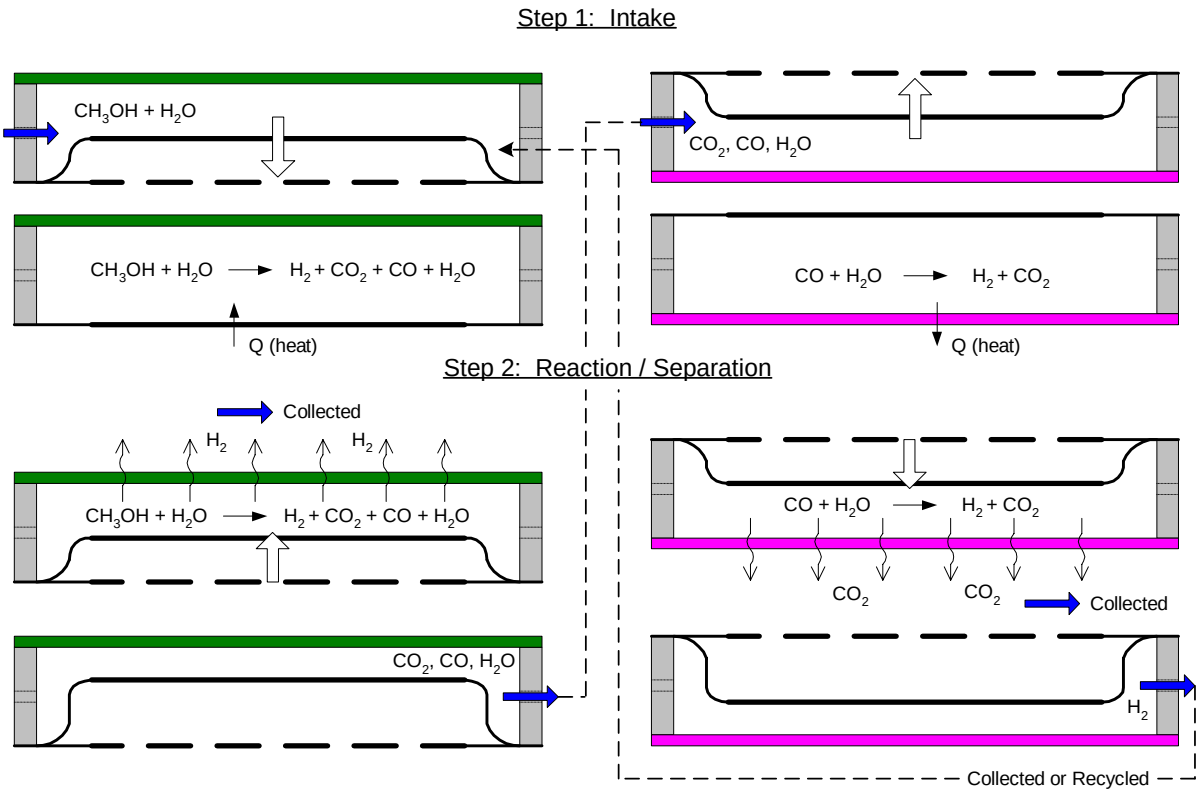

Figure 3.14 Operation of the flexible piston (diaphragm) - membrane reactor consisting of two fluidically-communicating chambers. Reforming, or hydrogen reaction chamber is on the left; and water-gas shift WGS/CO_2 reaction chamber is on the right.

In the present embodiment the two reactors operate in-phase, both performing similar operations at the same time in a one-to-one cycle. The exhaust stream from the hydrogen reactor becomes the intake stream for the CO_2 reactor on the next cycle, and the exhaust from the CO_2 reactor can be recycled back into the fuel stream on the next cycle. Ideally, only pure hydrogen remains after water gas shift in the CO_2 reactor. In reality, the reaction and separation processes will be non-ideal, and the remaining mixture will contain methanol, H_2, CO, and CO_2 which should be recycled for full recovery. In general, however, the two reactor chambers (reforming/hydrogen and WGS/CO_2) may or may not operate in phase or via the one-to-one cycle. That is, the phase-shifted operation may be more optimal under certain conditions, as well as one or more WGS/ CO_2

reaction chambers may be needed to operate in conjunction with a single reforming/ hydrogen chamber (and vice versa) to achieve the best performance. This is determined by the relative magnitude of characteristic time scales for the reforming and WGS reactions as well as H_2 and CO_2 separation processes for any given fuel. The capability for external control of the diaphragm motion should allow one to operate the system in an optimal mode.

Another design embodiment of the flexible actuated piston/diaphragm CHAMP reactor takes advantage of the fact that the two independently-controlled reacting units of the reactor (i.e., reforming/hydrogen and WGS/CO_2) could be timed to operate in-phase and in a one-to-one cycle. The diaphragm is modified to operate in a bi-directional mode, wherein it may extend in either direction (up or down), thus changing the volume/pressure in both a membrane reaction chamber "in front" as well as a collection chamber "behind" each unit of the reactor. The two reactor units are integrated into a single unit via inter-connected passageways and valves between the reaction and collection chambers. The operation is similar to that previously described but with several modifications as shown in Figures 3.15 - 3.17.

The combined cycle begins with the intake stroke (Figure 3.15), wherein the diaphragm within the reforming unit (left side) moves into its "up" position. During this up-stroke, the unreacted/unseparated mixture from the collection chamber of the WGS unit shown on the right, and a fresh mixture of fuel and water vapor from the intake, is drawn into the collection chamber at the bottom of the reforming unit.

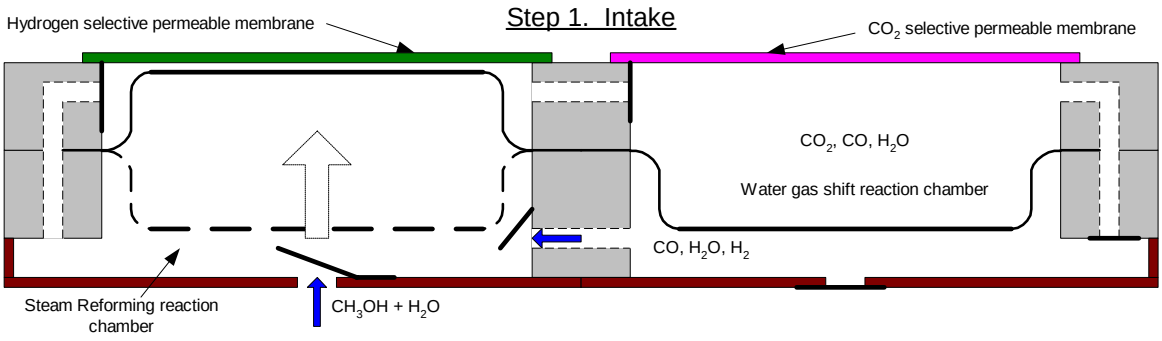

Figure 3.15 Intake stroke of the reforming unit. Fresh fuel and water vapor are drawn into the collection chamber at the bottom of the reforming unit.

In Step 2, the valves are closed and the diaphragm in the WGS reaction unit (right side) moves to the up position (Figure 3.16). During the upward motion of the piston, the WGS reaction ($CO+H_2O \rightarrow CO_2+H_2$) and CO_2 permeation occur simultaneously in the upper reaction chamber. Meanwhile in the reforming unit (left side), hydrogen is permeating through an H_2 selectively permeable membrane, and the steam reforming reaction is proceeding in both the upper "reaction" and lower "collection" chambers. When the reaction and permeation processes approach the desired state, a valve at the right connecting the upper reaction and lower collection chambers of the WGS unit opens and the mixture remaining in the WGS reaction chamber is sucked into the WGS collection chamber.

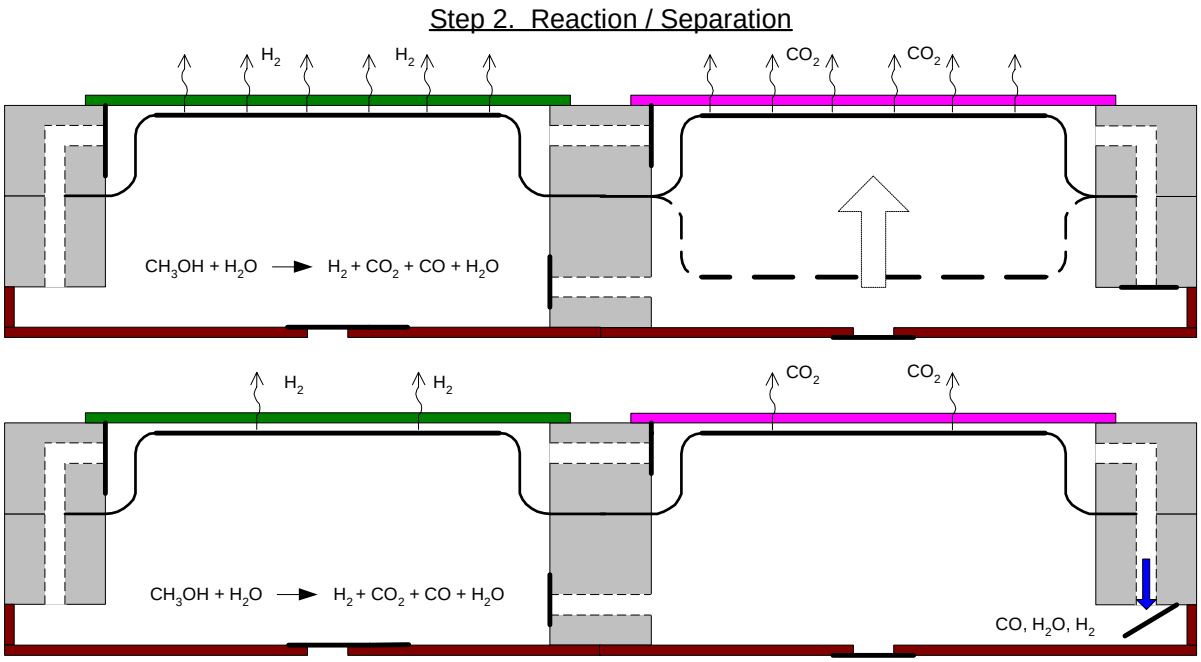

Figure 3.16 The reaction and separation stages.

Finally in Step 3, the system returns to its initial state to prepare for the next intake stroke. The diaphragm in the WGS/CO_2 reaction unit moves down, the valve connecting the reforming/hydrogen unit and the WGS/CO_2 unit opens up and the retentate mixture from the reforming/hydrogen unit is drawn into the reaction chamber of the WGS/CO_2 unit. Next, the valve between the two units closes, and the diaphragm in the reforming/hydrogen unit moves down, while opening the valve between the reaction and collection chambers of the reforming/hydrogen unit and pushing the reformate mixture from the lower collection chamber into the upper reaction chamber of this unit. The system has completed a cycle and is ready to proceed to the intake step shown in Figure 3.15.

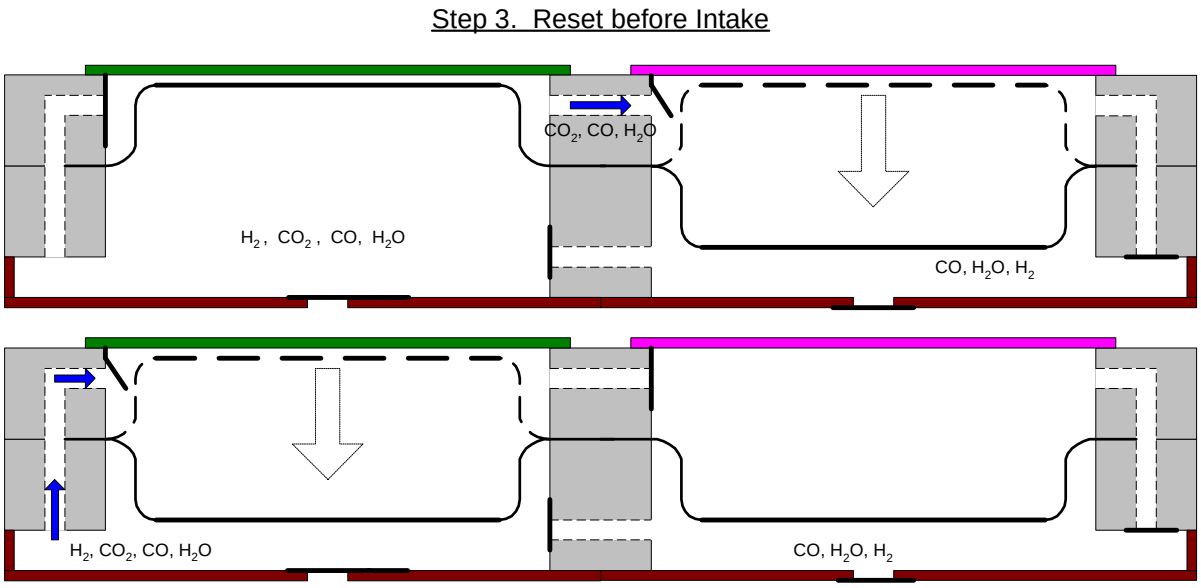

Figure 3.17 System is reset and prepared for the intake stroke.

3.4 Regenerative fuel processing

The regenerative CHAMP reactor just described achieves 100% fuel utilization as well as 100% separation/purification of both the hydrogen and byproduct CO_2 generated as reaction products. This is a significant development from a practical viewpoint, considering that it does not require that any of the individual steps in the process (steam reforming, hydrogen separation, WGS reaction, and CO_2 separation) operate at their ideal limit. Rather the individual steps should proceed as far as practically desirable and then the remaining unreacted or unseparated products are recycled back into the fuel stream to be used during the next cycle of the system. It should be noted that regenerative fuel processing described hereafter is not only applicable to the CHAMP (batch class of reactors), but yields similar benefits when implemented in typical continuous-flow reactors, as well.

3.4.1 System description

In typical state-of-the-art hydrogen-selective membrane reactors, only H_2 is separated from the reformate (products). Hydrogen separation via a selectively permeable membrane relies on a partial pressure difference of hydrogen across the membrane. As hydrogen is removed from the reformate mixture, both total pressure and H_2 concentration fall, leading to a precipitous drop in H_2 partial pressure. Because the H_2 partial pressure on the permeate side is not zero, some hydrogen will always be left on the retentate side. As discussed in Chapter 2, a trade-off occurs between minimizing the residence time of the mixture in the reactor (maximizing power output), and maximizing the percentage of hydrogen that is recovered (yield efficiency). The leftover retentate mixture is enriched in CO_2, yet still contains H_2 and CO—both valuable fuels. Small, incremental improvements in hydrogen recovery generally require large increases in system volume if one is to use the state-of-the-art process organization.

The high CO_2 concentration in this waste stream suggests that it would be feasible to separate a large percentage of the CO_2 (via a CO_2 selectively permeable membrane, following its liquefaction for storage, or other method) and then recycle the remaining valuable products (CO, H_2O, H_2) back into the fuel stream. This would result in complete fuel utilization as well as separating all of the byproduct CO_2 for sequestration and storage.

To demonstrate this capability and establish the ideal limit of how the reactor is expected to operate, a thermodynamic analysis of a methanol steam reforming, hydrogen-selective membrane reactor is carried out here. Several realistic scenarios are investigated using equilibrium calculations of the species concentrations, including CO_2

removal from the reformate and recycling of the remaining mixture (including H_2, CO, and CO_2) back into the fuel stream. It is demonstrated that the fuel mixture intake and composition can be adjusted according to the quantity and composition of the recycled products to establish periodic quasi-steady state operation of the reactor, wherein the fuel input and hydrogen recovery per cycle are constant. As one would expect, the hydrogen production per cycle is slightly lower than if no recycling took place; however, this comes with the tremendous benefit of wasting no fuel as compared to the case when valuable fuel components (e.g. H_2 and CO) are discharged in the exhaust.

3.4.2 Equilibrium Analysis

Ideally, in steam reforming of methanol (CH_3OH), one mole of CH_3OH and one mole of H_2O react to yield 3 moles of H_2 and one mole of CO_2. In reality, because of methanol decomposition and the water gas shift (WGS) reaction, the net steam reforming reaction is found by combining equations (2.1 – 2.3):

$$CH_3OH + H_2O \rightarrow (3\text{-}x)H_2 + (1\text{-}x)CO_2 + xCO + xH_2O \qquad (3.1)$$

where x is the fraction of carbon in the fuel that is oxidized to CO rather than CO_2 (via WGS or methanol decomposition). The equilibrium concentrations of reactants and products are calculated from the equilibrium reaction constants which depend on temperature. For illustrative purposes these calculations are carried out for the temperature range of 200–300 °C and pressure range of 1–10 atmospheres.

Methanol conversion (Figure 3.18) increases with temperature because the steam reforming reaction is endothermic, and decreases with increasing pressure (according to Le Chatlier's principle) because the number of moles of products exceeds the moles of

reactants by approximately 2:1. However, the pressure dependence is rather weak at elevated temperatures above 250 °C.

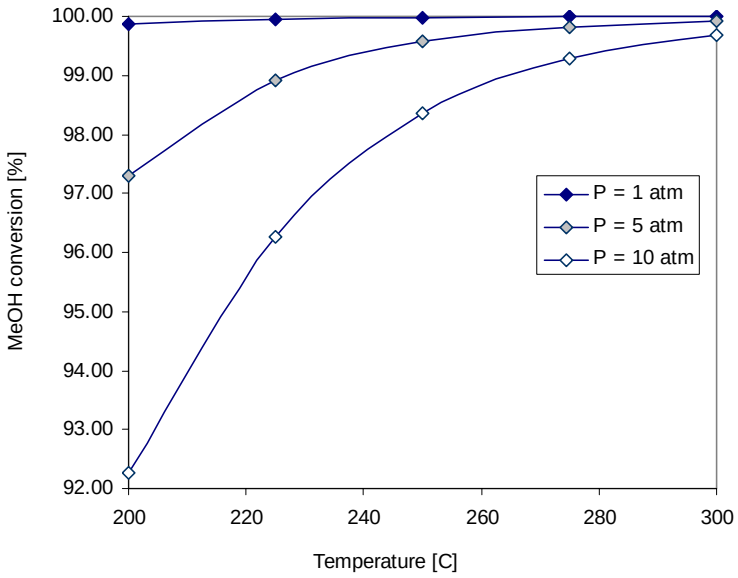

Figure 3.18 Equilibrium methanol conversion for various temperatures and pressures.

Hydrogen yield (Figure 3.19) is slightly less than ideal (3 moles of H_2 per mole of reactant) across the temperature and pressure ranges shown. Hydrogen yield decreases slightly with increasing temperature (for P = 1 atm) because it is consumed in the reverse WGS reaction ($CO_2+H_2 \rightarrow CO+H_2O$), which is favored at higher temperatures. At elevated operating pressures, hydrogen yield initially increases with temperature as methanol conversion increases, but then decreases at higher temperatures as the effects of the WGS reaction become more pronounced. Although hydrogen yield is high (more than 90% of the ideal limit), the hydrogen is not pure, but is mixed with 1 – 5 % CO, 15 – 20% CO_2, and trace amounts of unreacted CH_3OH.

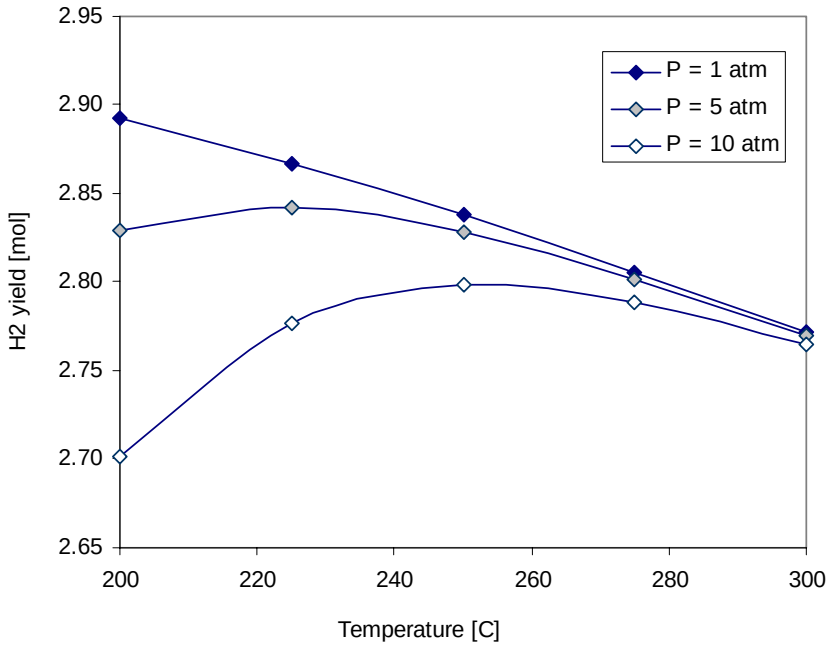

Figure 3.19 Equilibrium hydrogen yield (moles per mole of methanol) at various temperatures and pressures.

Reactions with Hydrogen separation

In the membrane reactor, hydrogen is separated from the products as the reaction is occurring. The amount of hydrogen removed depends on the partial pressure difference of hydrogen between the reaction and permeate sides. Thus, the partial pressure of hydrogen on the reaction side must always be greater than or equal to that on the permeate side. Equilibrium calculations of a hydrogen selective membrane reactor are carried out for several values of total operating pressure and with various permeate-side partial pressures, resulting in unseparated hydrogen remaining on the reaction (retentate) side after the reaction and permeation process reach equilibrium.

First, it is assumed that the permeate-side partial pressure is such that the retentate mixture contains 10% hydrogen (by mole fraction) at equilibrium. Table 3.1 shows the resulting mixture composition for various reactor temperatures and an operating pressure of 1 atm (Case 1) with and without hydrogen removal. Table 3.2

shows the results for an operating pressure of 10 atm (Case 2). Table 3.3 shows the results for an operating pressure of 5 atm but in this case (Case 3) the retentate mixture contains 20% hydrogen at equilibrium. Notice that the methanol conversion increases and CO decreases when hydrogen is removed due to the reaction equilibrium shift as hydrogen is separated from the mixture.

Table 3.1. Equilibrium composition of product stream with and without hydrogen separation (P = 1 atm)

Reactants [mol]		
CH_3OH	H_2O	Pressure [atm]
1.0	1.0	1.0

	Products [mol]					Meth Conversion	Products [mol fraction]				
Temp [C]	CH_3OH	H_2O	H_2	CO	CO_2	[%]	CH_3OH	H_2O	H_2	CO	CO_2
200	1.27E-03	0.10459	2.89287	0.10333	0.89541	99.873	3.18E-04	0.02616	0.72368	0.02585	0.22399
225	4.56E-04	0.13178	2.86731	0.13133	0.86822	99.954	1.14E-04	0.03295	0.71699	0.03284	0.21710
250	1.77E-04	0.16187	2.83778	0.16169	0.83813	99.982	4.43E-05	0.04047	0.70951	0.04043	0.20955
275	7.38E-05	0.19415	2.80571	0.19407	0.80585	99.993	1.84E-05	0.04854	0.70145	0.04852	0.20147
300	3.26E-05	0.22798	2.77195	0.22795	0.77202	99.997	8.16E-06	0.05700	0.69300	0.05699	0.19301

With hydrogen removal

	Products [mol]					Meth Conversion	Products [mol fraction]				
Temp [C]	CH_3OH	H_2O	H_2	CO	CO_2	[%]	CH_3OH	H_2O	H_2	CO	CO_2
200	4.96E-06	0.02145	0.11272	0.02145	0.97855	99.99950	4.37E-06	0.01891	0.09939	0.01891	0.86279
225	1.91E-06	0.02789	0.11509	0.02789	0.97211	99.99981	1.67E-06	0.02440	0.10069	0.02440	0.85050
250	7.89E-07	0.03523	0.11690	0.03523	0.96477	99.99992	6.85E-07	0.03058	0.10146	0.03058	0.83738
275	3.57E-07	0.04368	0.11974	0.04368	0.95632	99.99996	3.07E-07	0.03754	0.10292	0.03754	0.82199
300	1.68E-07	0.05282	0.12131	0.05282	0.94718	99.99998	1.43E-07	0.04499	0.10332	0.04499	0.80671

Table 3.2. Equilibrium composition of product stream with and without hydrogen separation (P = 10 atm)

Reactants [mol]		
CH_3OH	H_2O	Pressure [atm]
1.0	1.0	10.0

	Products [mol]					Meth Conversion	Products [mol fraction]				
Temp [C]	CH_3OH	H_2O	H_2	CO	CO_2	[%]	CH_3OH	H_2O	H_2	CO	CO_2
200	0.07728	0.14418	2.70127	0.06690	0.85582	92.272	0.02010	0.03749	0.70246	0.01740	0.22255
225	0.03747	0.14832	2.77674	0.11085	0.85168	96.253	0.00955	0.03779	0.70744	0.02824	0.21699
250	0.01647	0.16847	2.79860	0.15200	0.83153	98.353	0.00415	0.04247	0.70546	0.03832	0.20961
275	0.00717	0.19682	2.78884	0.18965	0.80318	99.283	0.00180	0.04938	0.69972	0.04758	0.20152
300	0.00323	0.22911	2.76444	0.22588	0.77089	99.677	0.00081	0.05737	0.69223	0.05656	0.19303

With hydrogen separation

	Products [mol]					Meth Conversion	Products [mol fraction]				
Temp [C]	CH_3OH	H_2O	H_2	CO	CO_2	[%]	CH_3OH	H_2O	H_2	CO	CO_2
200	5.24E-04	0.02203	0.11612	0.02151	0.97797	99.948	4.60E-04	0.01936	0.10202	0.01890	0.85926
225	1.95E-04	0.02811	0.11630	0.02795	0.97189	99.981	1.70E-04	0.02466	0.10162	0.02442	0.84922
250	7.97E-05	0.03535	0.11743	0.03527	0.96465	99.992	6.91E-05	0.03067	0.10187	0.03060	0.83680
275	3.54E-05	0.04362	0.11930	0.04359	0.95638	99.996	3.05E-05	0.03751	0.10259	0.03748	0.82239
300	1.69E-05	0.05290	0.12162	0.05288	0.94710	99.998	1.44E-05	0.04504	0.10355	0.04502	0.80637

Table 3.3. Equilibrium composition of product stream with and without hydrogen separation (P = 5 atm)

Reactants [mol]		
CH_3OH	H_2O	Pressure [atm]
1.0	1.0	5.0

	Products [mol]					Meth Conversion	Products [mol fraction]				
Temp [C]	CH_3OH	H_2O	H_2	CO	CO_2	[%]	CH_3OH	H_2O	H_2	CO	CO_2
200	2.70E-02	0.11649	2.82962	0.08954	0.88351	97.305	6.83E-03	0.02952	0.71707	0.02269	0.22389
225	1.08E-02	0.13616	2.84223	0.12536	0.86384	98.920	2.71E-03	0.03422	0.71442	0.03151	0.21713
250	4.35E-03	0.16352	2.82778	0.15918	0.83648	99.565	1.09E-03	0.04097	0.70848	0.03988	0.20958
275	1.83E-03	0.19480	2.80153	0.19297	0.80520	99.817	4.58E-04	0.04874	0.70103	0.04829	0.20148
300	8.14E-04	0.22826	2.77012	0.22744	0.77174	99.919	2.03E-04	0.05709	0.69281	0.05688	0.19301

With hydrogen separation

	Products [mol]					Meth Conversion	Products [mol fraction]				
Temp [C]	CH_3OH	H_2O	H_2	CO	CO_2	[%]	CH_3OH	H_2O	H_2	CO	CO_2
200	7.51E-04	0.03270	0.25883	0.03195	0.96730	99.925	5.81E-04	0.02532	0.20041	0.02474	0.74896
225	2.84E-04	0.04190	0.26184	0.04162	0.95810	99.972	2.17E-04	0.03214	0.20084	0.03192	0.73488
250	1.15E-04	0.05254	0.26421	0.05243	0.94746	99.989	8.73E-05	0.03990	0.20065	0.03982	0.71954
275	5.07E-05	0.06474	0.26872	0.06469	0.93526	99.995	3.80E-05	0.04895	0.20152	0.04851	0.70138
300	2.37E-05	0.07812	0.27255	0.07810	0.92188	99.998	1.75E-05	0.05784	0.20179	0.05782	0.68253

Of particular interest is the hydrogen recovered (separated) per mole of fuel and water vapor. Calculations show that, in the limit of chemical equilibrium, between 2.7 and 2.9 moles of hydrogen are produced. However, the hydrogen is mixed with CO_2 and CO. Figure 3.20 shows the production of separated hydrogen for the three membrane reactor cases just mentioned. The first two cases are for reactors operating at 1 and 10

atmospheres of total pressure. The results are virtually indistinguishable because the hydrogen content of the remaining retentate mixture (at equilibrium) is the same (10%) in both cases. In the third case this percentage is doubled (20%) resulting in a lower yield of pure, separated hydrogen (because more is left behind in the "exhaust" stream).

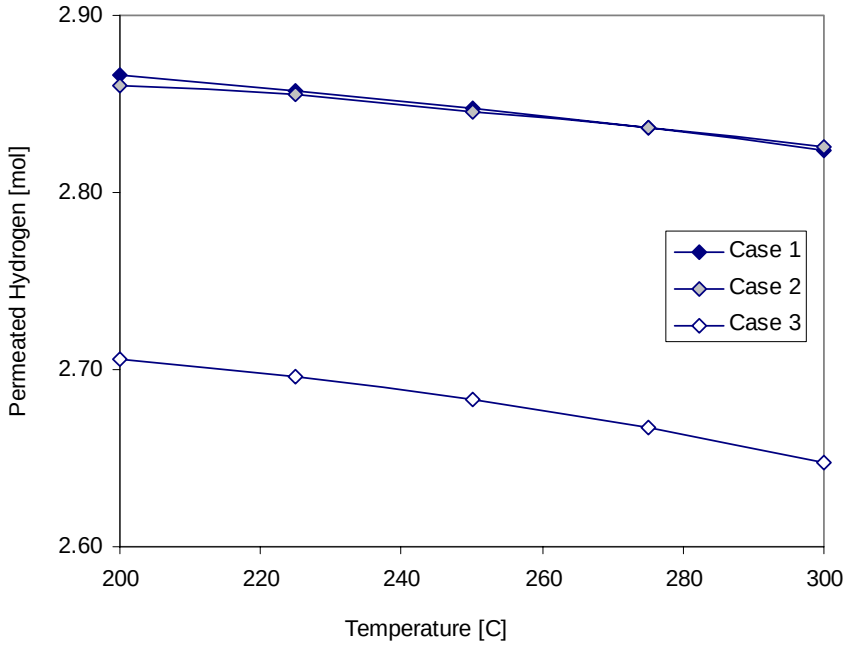

Figure 3.20 Pure (separated) hydrogen produced per mole of methanol and water, for various operating pressures and various values of hydrogen content remaining in the retentate mixture. (Case 1: 1 atm pressure, 10% hydrogen on low side; Case 2: 10 atm pressure, 10% hydrogen on low side; Case 3: 5 atm pressure, 20% hydrogen on low side)

CO_2 Removal

The mixture that remains, after steam reforming and hydrogen separation processes are complete, is enriched in CO_2 (see Tables 3.1 - 3.3). For illustrative purposes, it is assumed the CO_2 is separated by liquefaction. The saturation pressure of pure CO_2 at 15 °C is 50 bars (see Figure A.6). By raising the pressure to 100 bars, and cooling the present mixture to 15 °C, CO_2 will condense out of the gas phase leaving behind a mixture that is saturated with CO_2 vapor in equilibrium with the liquid phase (in

this case, 50% CO_2 vapor). In practice, the temperature would only be brought as low as ambient. Because the density of the liquid (or super critical) CO_2 depends on temperature, the liquefaction system would be designed for the highest expected ambient temperature. The required pressure may be higher than that used in this example, and the volume of the storage tank for the collected CO_2 would be adjusted accordingly. The balance of the gas phase mixture is H_2 and CO. (Water vapor and methanol will be condensed to liquid under these conditions.) This mixture is now ready to be recycled back into the fuel stream of the regeneratively-operated reactor.

Product Recycle

Because the recycled stream contains hydrogen, carbon monoxide, and carbon dioxide, the fuel stream composition must be adjusted accordingly. The quantity of methanol is reduced so that the total carbon (CH_3OH, CO, and CO_2) in the fuel mixture remains at 1 mole (normalized by the reactor volume). The water vapor is reduced so that the ratio of unreacted carbon (CH_3OH and CO) to water vapor is 1:1. An example of the fuel stream composition (based on the results of calculations for Case 1 above) is shown in Table 3.4. Given this fuel mixture, the steam reforming and hydrogen membrane separation processes are simulated and the resulting equilibrium mixture composition is calculated.

Table 3.5 compares the results from an initially pure fuel mixture (Case A) and a fuel mixture that includes recycled products (Case B). The species concentrations of the resulting mixtures are virtually the same (within the rounding error of calculations) for both cases. This indicates that the process of recycle, reaction, hydrogen separation, and CO_2 removal could be repeated over and over in a quasi-steady fashion. However, the

recovered hydrogen (separated) per cycle is reduced by 15-20%. Thus, the power density of the reactor is reduced due to recycling. While this is generally an undesirable effect, it results in 100% fuel utilization and 100% CO_2 capture.

Table 3.4. Fuel mixture with recycled products

Total pressure 1.0 atm

	Reactants [mol]				
Temp [C]	CH_3OH	H_2O	H_2	CO	CO_2
200	0.84450	0.86595	0.11272	0.02145	0.13405
225	0.82917	0.85706	0.11509	0.02789	0.14294
250	0.81240	0.84763	0.11690	0.03523	0.15237
275	0.79289	0.83657	0.11974	0.04368	0.16343
300	0.77236	0.82518	0.12131	0.05282	0.17482

Table 3.5. Reaction product output without (A) and with (B) recycling

Total pressure 1.0 atm

	Products [mol]										Methanol Conversion [%]		Hydrogen Recovery [mol]	
Temp [C]	CH_3OH		H_2O		H_2		CO		CO_2					
	A	B	A	B	A	B	A	B	A	B	A	B	A	B
200	4.96E-06	5.15E-06	0.0215	0.0216	0.1127	0.1146	0.0215	0.0216	0.9786	0.9784	100.00	100.00	2.87	2.53
225	1.91E-06	1.95E-06	0.0279	0.0280	0.1151	0.1160	0.0279	0.0280	0.9721	0.9704	100.00	100.00	2.86	2.49
250	7.89E-07	7.86E-07	0.0352	0.0352	0.1169	0.1167	0.0352	0.0352	0.9648	0.9648	100.00	100.00	2.85	2.44
275	3.57E-07	3.50E-07	0.0437	0.0435	0.1197	0.1187	0.0437	0.0435	0.9563	0.9565	100.00	100.00	2.84	2.38
300	1.68E-07	1.67E-07	0.0528	0.0528	0.1213	0.1210	0.0528	0.0528	0.9472	0.9473	100.00	100.00	2.82	2.32

3.5 Conclusions

The CHAMP reactor has several interesting features that provide motivation for the continued study of this fuel processing technology:

- First, the residence time of the mixture and volume of the reaction chamber can be controlled precisely by the user.
- Second, the reactor is operating in a transient mode and each reaction step is forced to proceed in the direction that favors maximum hydrogen production by imposing non-equilibrium chemistry conditions as needed.

- Third, the reactor is scalable. Individual reactor units are optimized for size, throughput, and operating conditions as dictated by the optimal chemistry of the process. Multiple reactors can be then stacked and operated in tandem (in, out, or with a time-shift of phase with each other) to produce a continuous stream of products at a desired rate matched to the end-use application. Based on the required hydrogen generation rate, only the necessary number of reactor units needs to operate at any given time, and if the power demand changes, fewer or a greater number of reactors can immediately be brought on (or off) line to provide the required flow of hydrogen.
- Finally, steam reforming provides the capability to pre-concentrate and separate not only hydrogen but also carbon dioxide as the only two products of the fuel processing sequence. Thus, one more extra step may be added downstream of the reactor to sequester the carbon dioxide via either liquefaction or an appropriate chemical reaction. This also enables regenerative processing, applicable to both batch and continuous flow reactors, which avoids the loss of residual fuel products by recycling the exhaust.

To develop and analyze the operation of a real reactor requires transient modeling of the coupled transport, reaction kinetics, separation, and volume compression processes. In the next chapter I analyze an ideal kinetic model of the CHAMP reactor, and in Chapter 5 expand this model to include the effects of mass transport limitations on the rate of hydrogen production.

CHAPTER 4

TRANSIENT BATCH VS CONTINUOUS FLOW REACTORS

Establishing the limit of ideal reactor performance is the first step in designing and optimizing a real or working reactor. Here a mathematical model of an idealized transient batch reactor is formulated and a one-to-one comparison is made with an ideal, plug-flow, wall-coated reactor model of comparable size and hydrogen output. In this analysis heat and mass transport limitations are neglected (although not negligible in real reactors) so that the ideal limits of performance may be established.

4.1 Ideal CHAMP reactor model

The analyzed configuration (see Figure 4.1) is a "slit" reactor with a high aspect ratio in the directions normal to H. The lower, moving wall is coated with a porous catalyst layer of porosity, ε, and thickness, d (zone 1). The bulk reactor chamber is of variable height, $H(t)$, initially H_0 (zone 2). In this example, the upper surface is a hydrogen-selective, palladium-silver (Pd-Ag) alloy or similar dense membrane of thickness, δ (zone 3). The partial pressure of hydrogen outside the membrane (permeate side) is maintained at a reference value.

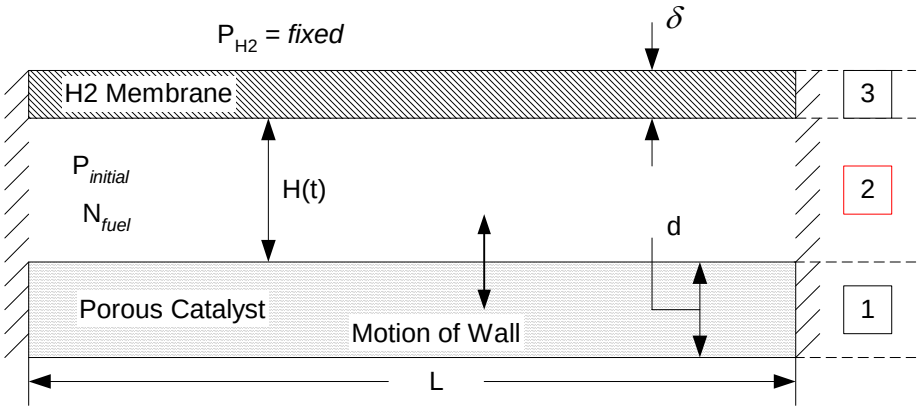

Figure 4.1 CHAMP reactor geometry and major domains

4.1.1 Model formulation

The governing equations are derived by considering the molar balance for a control volume that encloses the entire reactor. In the absence of transport limitations, the rate of change of number of moles of any given species within the reactor is equal to the rate of production or consumption (via reactions) minus the rate of permeation through the membrane, or,

$$\frac{dN_i}{dt} = \sum_j \dot{R}_{ij} - \dot{J}_i \tag{4.1}$$

where, N_i is the number of moles of species *i* within the reaction chamber, $\dot{R}_{ij}$ is the rate of production of species *i* via the j^{th} reaction, and $\dot{J}_i$ is the permeation rate of species *i* through the membrane.

The steam reforming, methanol decomposition, and water gas shift reactions proceed at the intrinsic rates (r_{SR}, r_d, and r_{WGS}, respectively) given by the kinetic model of Peppley et al. [61] described in section 4.3. The rate of permeation of hydrogen across the *Pd-Ag* membrane is diffusion limited and obtained by application of Sievert's law [51]; it depends on the thickness of the membrane, δ, the membrane permeability, D_m,

and the difference in hydrogen partial pressure between the retentate (reaction) side, $P_D^{1/2}$, and permeate side, $P_{D,\infty}^{1/2}$. Because of the assumption of idealized, infinitely fast mixing, the concentrations of all species are uniform throughout the reaction chamber. Isothermal conditions are assumed in the reactor: the temperature of the thin catalyst layer is maintained by external heating, the fuel mixture is brought in at the temperature of the catalyst, and the temperature of the thin membrane is maintained, for example, by preheating the sweep gas. The practical implications of this assumption are discussed in Section 4.5.3. Table 4.1 lists the set of model equations for each of the five species considered: A – methanol, B – water vapor, C – carbon dioxide, D – hydrogen, and F – carbon monoxide.

The reactor is initially filled with N_{fuel} moles of fuel mixture (per unit depth) consisting of methanol and water vapor at a 1:1 ratio with initial pressure, $P_{initial}$,

$$N_{fuel} = \frac{P_{initial}\left(H_0 + \varepsilon d\right)L}{RT} \quad \left[\frac{mol}{m}\right] \tag{4.2}$$

where R is the universal gas constant and T is the absolute temperature (assuming ideal gas behavior). The initial conditions for each species are,

$$N_{A,0} = N_{B,0} = 0.5N_{fuel}; \quad N_{C,0} = N_{D,0} = N_{F,0} = 10^{-6}N_{fuel}; \tag{4.3}$$

The small initial amounts of carbon dioxide, hydrogen, and carbon monoxide are provided to avoid singularities in the experimentally-obtained kinetic expressions [86].

The size of the reaction chamber, H, (and the total pressure, P) is variable and controlled dynamically by moving the lower wall (piston) up or down. Once the reactions and permeation processes have proceeded sufficiently near to equilibrium, the cycle is finished and the reaction chamber is emptied and returned to its initial state.

4.1.2 Performance assessment

Several parameters are used to quantify the performance of the reactor. The conversion of fuel to products is given by the parameter

$$\chi(t) = 1 - N_A / N_{A,0} \tag{4.4}$$

which increases from 0 at initial time, to nearly 1 at full conversion (equilibrium). One possible criterion for completion of a cycle is that conversion has reached *x*% of its equilibrium value. The total quantity of hydrogen that has permeated through the membrane is the hydrogen yield, given in moles (per unit depth)

$$Y = \int_{t=0}^{t=\tau} L \frac{D_m}{\delta} \left(P_D^{1/2} - P_{D,\infty}^{1/2} \right) dt \quad \left[\frac{mol}{m} \right] \tag{4.5}$$

The cycle-averaged hydrogen yield rate is defined as, $\dot{Y} = Y / \tau$ (where τ is the residence time). Equally important, the hydrogen yield efficiency provides the ratio of hydrogen yield achieved to the "ideal" quantity of hydrogen that could be generated. According to Eq. (2.1), the ideal hydrogen yield is equal to three times the initial quantity of methanol, so the hydrogen yield efficiency is simply $\gamma = Y / 3N_{A,0}$. Once this value has reached *x*% of its equilibrium value the cycle is complete. Note that the equilibrium value of this ratio is less than 100% due to the formation of CO and the nonzero reference hydrogen partial pressure on the permeate side of the membrane.

Table 4.1. Ideal species conservation equations for the CHAMP and CF reactor designs

Species	Model Equations (CHAMP)	Model Equations (CF)
CH_3OH	$\frac{dN_A}{dt} = \rho_{cat} d\ L\left(-r_{sr} - r_d\right)$	$\frac{d\dot{N}_A}{dz} = \rho_{cat} d\left(-r_{sr} - r_d\right)$
H_2O	$\frac{dN_B}{dt} = \rho_{cat} d\ L\left(-r_{sr} - r_{wgs}\right)$	$\frac{d\dot{N}_B}{dz} = \rho_{cat} d\left(-r_{sr} - r_{wgs}\right)$
CO_2	$\frac{dN_C}{dt} = \rho_{cat} d\ L\left(r_{sr} + r_{wgs}\right)$	$\frac{d\dot{N}_C}{dz} = \rho_{cat} d\left(r_{sr} + r_{wgs}\right)$
H_2	$\frac{dN_D}{dt} = \rho_{cat} d\ L\left(3r_{sr} + r_{wgs} + 2r_d\right) - L\frac{D_m}{\delta}\left(P_D^{1/2} - P_{D,\infty}^{1/2}\right)$	$\frac{d\dot{N}_D}{dz} = \rho_{cat} d\left(3r_{sr} + r_{wgs} + 2r_d\right) - \frac{D_m}{\delta}\left(P_D^{1/2} - P_{D,\infty}^{1/2}\right)$
CO	$\frac{dN_F}{dt} = \rho_{cat} d\ L\left(r_d - r_{wgs}\right)$	$\frac{d\dot{N}_F}{dz} = \rho_{cat} d\left(r_d - r_{wgs}\right)$
total pressure: $P_{Tot}(t) = \frac{N_{Tot}(t)RT}{\left(H(t) + \varepsilon d\right)L}$		mixture velocity: $U(z) = \frac{\dot{N}_{Tot}(z)RT}{P_{Tot}\left(H_0 + \varepsilon d\right)}$

4.2 Ideal Continuous flow (CF) reactor model

The ideal case considered here is virtually the same as described above except that the reactor is operated at steady-state in a continuous flow fashion (plug flow), rather than in a batch-wise mode. Again, the configuration is a "slit" reactor (see Figure 4.2), the lower wall is coated with a porous catalyst layer of porosity, ε, and thickness, d (zone 1), and the bulk reactor chamber is of height, H_0 (zone 2). The upper surface is a hydrogen-selective membrane of thickness, δ (zone 3). The partial pressure of hydrogen outside the membrane (permeate side) is maintained at a fixed reference value. The primary dimensions of the reactor, H and L, are fixed. The residence time is defined as the length of time that the mixture remains in the flow channel, during which time the reactions and permeation processes proceed at steady-state.

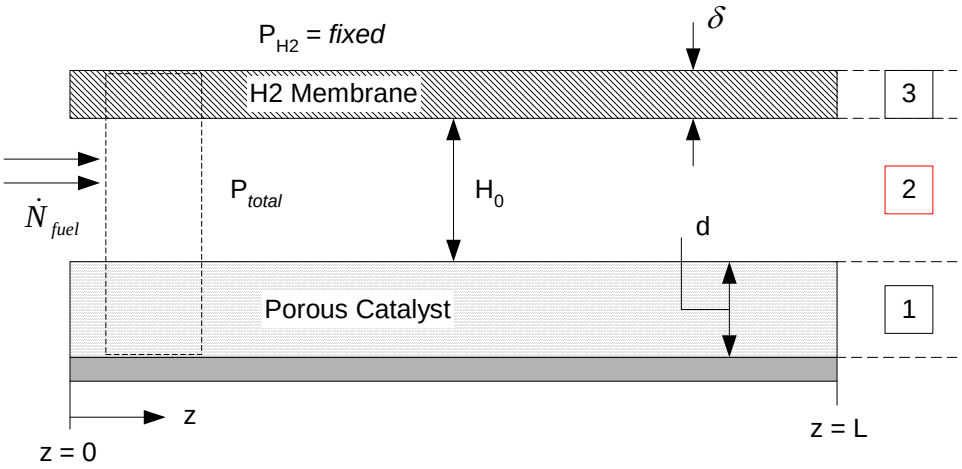

Figure 4.2 Schematic drawing of the analyzed plug-flow reactor

4.2.1 Model formulation

In the absence of transport limitations, the governing plug-flow conservation equations are derived by considering a molar balance for the control volume shown in Figure 4.2 (dashed lines). The rate of change of molar flow rate of any given species is equal to the rate of production or consumption (via reactions) minus the rate of permeation through the membrane, or,

$$\frac{d\dot{N}_i}{dz} = \sum_j \dot{R}_{ij} - \dot{J}_i \tag{4.6}$$

where $\dot{N}_i$ is the molar flow rate of species i and the reaction and permeation rate expressions were defined previously. The model equations for each of the five component species are listed in Table 4.1.

At the inlet, $\dot{N}_{fuel}$ moles of fuel mixture consisting of methanol and water vapor in a 1:1 ratio is introduced into the reactor which is maintained at a uniform total pressure, P_{Tot}. The molar flow rate (per unit depth), at the inlet is

$$\dot{N}_{fuel} = \frac{P_{tot}\left(H_0 + \varepsilon d\right)U_0}{RT} \quad \left[\frac{mol}{m \cdot s}\right] \tag{4.7}$$

Where, U_0 is the molar average velocity at the inlet. Because the pressure in the reactor is assumed constant (neglecting pressure drop) [51], the molar average velocity of the mixture, $U(z)$, varies along the length of the channel in order to maintain conservation of mass (this expression is given in Table 4.1). The boundary condition for molar flow rate of each species at the inlet is,

$$\dot{N}_{A,0} = \dot{N}_{B,0} = 0.5\dot{N}_{fuel}; \quad \dot{N}_{C,0} = \dot{N}_{D,0} = \dot{N}_{F,0} = 10^{-6}\dot{N}_{fuel}; \tag{4.8}$$

4.2.2 Performance assessment

The parameters that characterize CF reactor performance are similar to that of the CHAMP reactor. The conversion of fuel to products is given by the parameter

$$\chi(z) = 1 - \dot{N}_A / \dot{N}_{A,0} \tag{4.9}$$

which increases from 0 at the inlet, to nearly 1 at full conversion (equilibrium). With a fixed reactor length, *L*, and fixed inlet flow rate, conversion will reach *x*% of its equilibrium value at the outlet of the flow channel. The total molar flow rate of hydrogen permeating through the membrane at steady-state is the hydrogen yield rate, given in moles per second (per unit depth),

$$\dot{Y} = \int_{z=0}^{z=L} \frac{D_m}{\delta}\left(P_D^{1/2} - P_{D,\infty}^{1/2}\right)dz \quad \left[\frac{mol}{m\ s}\right] \tag{4.10}$$

Equally important, the hydrogen yield efficiency provides the ratio of hydrogen permeation rate to the "ideal" rate of hydrogen generation, $\gamma = \dot{Y}/3\dot{N}_{A,0}$. This parameter will reach *x*% of its equilibrium value by the time the flow reaches the end of the channel.

4.3 Reaction mechanisms and kinetic model

Numerous kinetic studies and kinetic models for methanol steam reforming are available in the literature [30,61-67], and these vary widely in their assumption of primary reaction mechanisms, level of detail (complexity), and accuracy. For the present work, the kinetic model should also account for the formation of the byproduct CO via the methanol decomposition and water gas shift reactions [equations (2.2) and (2.3)], because this affects the amount of hydrogen being produced.

In a recent study by Peppley, et al. [86] a comprehensive kinetic model was developed that predicts these reaction rates based on experimental data obtained in the temperature range 160-260 °C, pressure range 1-35 bar, and methanol conversion ranging from approximately 4% to nearly 100% over Cu/ZnO/Al_2O_3 catalysts. The rate of steam reforming reaction is:

$$r_{sr} = \frac{k_{sr} K^*_{CH_3O^{(1)}} \left(p_A / p_D^{1/2} \right) \left(1 - p_D^3 p_C / K_{sr} p_A p_B \right) C_{S_1}^T C_{S_{1a}}^T}{\left(1 + K^*_{CH_3O^{(1)}} \left(p_A / p_D^{1/2} \right) + K^*_{HCOO^{(1)}} p_C p_D^{1/2} + K^*_{OH^{(1)}} \left(p_B / p_D^{1/2} \right) \right) \left(1 + K^{1/2}_{H^{(1a)}} p_D^{1/2} \right)} S_A \qquad (4.11)$$

The rate of the methanol decomposition reaction is:

$$r_d = \frac{k_d K^*_{CH_3O^{(2)}} \left(p_A / p_D^{1/2} \right) \left(1 - p_D^2 p_F / K_d p_A \right) C_{S_2}^T C_{S_{2a}}^T}{\left(1 + K^*_{CH_3O^{(2)}} \left(p_A / p_D^{1/2} \right) + K^*_{OH^{(2)}} \left(p_B / p_D^{1/2} \right) \right) \left(1 + K^{1/2}_{H^{(2a)}} p_D^{1/2} \right)} S_A \qquad (4.12)$$

The rate of the water gas shift reaction is:

$$r_{wgs} = \frac{k_{wgs} K^*_{OH^{(1)}} \left(p_F p_B / p_D^{1/2} \right) \left(1 - p_D p_C / K_{wgs} p_F p_B \right) \left(C_{S_1}^T \right)^2}{\left(1 + K^*_{CH_3O^{(1)}} \left(p_A / p_D^{1/2} \right) + K^*_{HCOO^{(1)}} p_C p_D^{1/2} + K^*_{OH^{(1)}} \left(p_B / p_D^{1/2} \right) \right)^2} S_A \qquad (4.13)$$

According to Peppley, the rate constants, k_{sr}, k_d, k_{wgs}, are calculated from Arrhenius expressions, $k_j = k_j^{\infty} \exp\left(-E_j / RT \right)$, where the pre-exponential constants and activation

energies are given in the Table 4.2. The equilibrium constants, K_i, are calculated from van't Hoff expressions, $K_i = \exp\left(\frac{\Delta S_i}{R} - \frac{\Delta H_i}{RT}\right)$, where the change in entropy and enthalpy values are given in the Table 4.3. Partial pressures of the individual species are calculated in units of *bar*. The surface area per unit volume of catalyst, S_A, is given in Table 4.4 in Section 4.5 The site concentrations, C_i^T, are $7.5x10^{-6}\,mol\,m^{-2}$ for Type 1 and Type 2 sites, and $1.5x10^{-5}\,mol\,m^{-2}$ for Type 1a and Type 2a sites [61].

Table 4.2. Parameters for calculation of rate constants

Rate Constant	$k_j^{\infty} \quad \left(m^2 s^{-1} mol^{-1}\right)$	$E_j \left(kJ\ mol^{-1}\right)$
k_{sr}	$7.4x10^{14}$	102.8
k_d	$3.8x10^{20}$	170.0
k_{wgs}	$5.9x10^{13}$	87.6

Table 4.3. Parameters for calculation of equilibrium constants

Equ. Constant	$\Delta S_i \left(J\ mol^{-1} K^{-1}\right)$	$\Delta H_i \left(kJ\ mol^{-1}\right)$
K_{sr}	177.0	49.2
K_d	219.0	90.4
K_{wgs}	-41.9	-41.2
$K^*_{CH_3O^{(1)}}$	-41.8	-20.0
$K^*_{OH^{(1)}}$	-44.5	-20.0
$K^*_{H^{(1a)}}$	-100.8	-50.0
$K^*_{HCOO^{(1)}}$	179.2	100.0
$K^*_{CH_3O^{(2)}}$	30.0	-20.0
$K^*_{OH^{(2)}}$	30.0	-20.0
$K^*_{H^{(2a)}}$	-46.2	-50.0

4.4 Numerical solution method

The model equations for the CHAMP reactor given in Table 4.1 were explicitly integrated forward in time. For example, the number of moles of methanol in the reactor at the *n +1* time step is approximated as

$$\frac{N_A^{(n+1)} - N_A^{(n)}}{\Delta t} = \rho_{cat} d\ L\left(-r_{sr} - r_d\right)^{(n)} \tag{4.14}$$

The rate expressions are highly non-linear initially, when the concentration of products is very small, therefore a short time step (0.001 s) was required in order to achieve time step independent results. For computational efficiency, this time step could be gradually increased to 0.01 s after several seconds of simulation time without affecting the results; however, simulations required only several minutes to run regardless.

The model equations for the CF reactor were integrated from the inlet to the outlet of the flow channel. In these equations, the steady-state flow rate of methanol, for example, at the *n +1* channel node is approximated as

$$\frac{\dot{N}_A^{(n+1)} - \dot{N}_A^{(n)}}{\Delta z} = \rho_{cat} d\ L\left(-r_{sr} - r_d\right)^{(n)} \tag{4.15}$$

Discretizing the channel into 20,000 uniformly spaced nodes ensured grid independent results. The implementation of the kinetic expressions was validated by setting the membrane permeability to zero and reproducing the results presented by Peppley et al. [61] in terms of methanol conversion versus weight of catalyst (W) to fuel flow rate (F) ratio (W/F). The Matlab code for solving both the CHAMP and CF ideal reactor models is included in the Appendix B.

4.5 Results and Discussion

4.5.1 Time evolution of species concentrations

Although an assessment of the reactor's hydrogen output is the ultimate goal, the details of the reaction kinetics provide a deeper understanding of how the reactor operates. A baseline case using the parameters given in Table 4.4 was established for the solution of the reactor models. The cases of reactors with and without hydrogen permeable membrane were solved under baseline conditions in order to illustrate the effects of product removal on mixture composition.

Table 4.4. Baseline parameters for reactor models and performance comparison

Model Parameters	**Value [*units*]**
Temperature, T	523 [K]
Initial (or total) Pressure, $P_{initial}$	101.3 [kPa]
Initial size of reactor, H_0	0.01 [m]
Length of reactor, L	0.10 [m]
Membrane permeability, D_{memb}	3.8×10^{-9} [mol / m s $Pa^{1/2}$]
Membrane thickness, δ	1×10^{-5} [m]
Low side partial pressure of hydrogen, P_D^{∞}	20.26 [kPa]
Effective thickness of catalyst layer, d	5×10^{-4} [m]
Density of catalyst, ρ_{cat}	1300 [kg/m^3]
Porosity of catalyst, ε	0.5 [-]
Specific surface area of catalyst, S_A	102×10^3 [m^2/kg]

The composition of the mixture in the reactor (without a membrane) as it evolves through time from the initial condition of pure methanol and water vapor to its equilibrium state is shown in Figure 4.3. Time is scaled by the weight of catalyst (W) and the fuel flow rate (F), also known as the weight to fuel ratio (W/F). Also shown in Figure 4.3 are the reaction rates for steam reforming, decomposition, and water gas shift (WGS). Steam reforming initially is the dominant reaction, the rate of methanol decomposition is nearly 2 orders of magnitude slower, and the water gas shift reaction

rate is negligible. As the concentrations of hydrogen and carbon dioxide become large, the WGS reaction reverses to produce carbon monoxide and water vapor $\left(H_2 + CO_2 \rightarrow H_2O + CO\right)$. With methanol becoming heavily depleted, the steam reforming reaction slows down, and the reverse WGS becomes the dominant reaction. At this point the reactor is a net consumer of hydrogen and is producing CO from CO_2—a highly unfavorable mode of operation—albeit at a very slow rate.

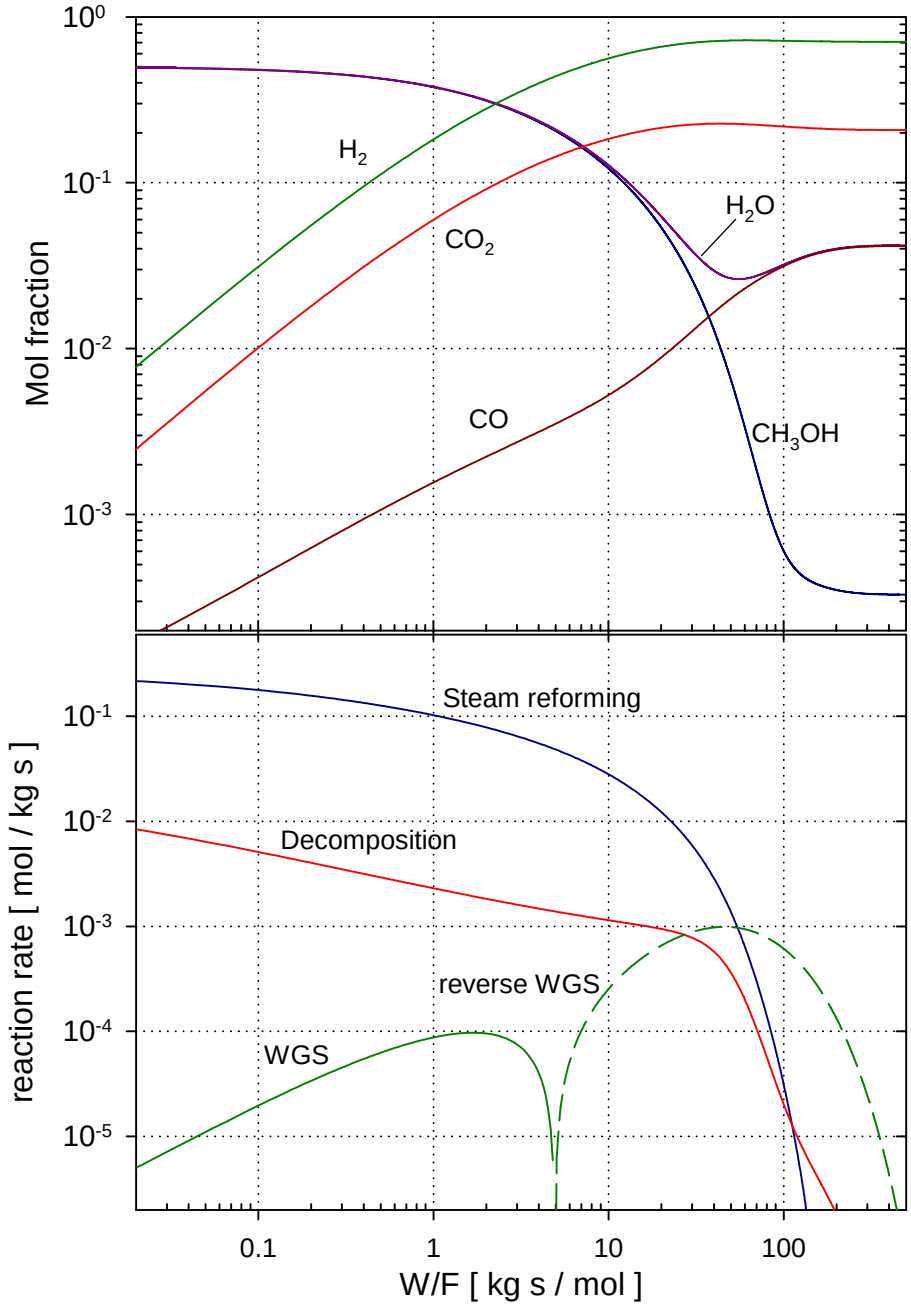

Figure 4.3. The transient evolution of the mixture composition in the CHAMP reaction chamber (no membrane) as reactants are converted to products. Also shown are the primary reaction rates. Temperature is 523 K, initial pressure is 1 atm, and all other parameters are baseline.

The effects of temperature on the equilibrium concentrations of the primary components in the methanol steam reforming, decomposition, and water gas shift system

[Eqs. (2.1) – (2.3)] are seen in Figure 4.4. At equilibrium, methanol has nearly completely disappeared (less than 0.1% remains). The reverse water gas shift reaction, $H_2 + CO_2 \rightarrow H_2O + CO \quad (\Delta H = 41.2\, kJ/mol)$, is endothermic and thus favors the products as temperature increases. This results in elevated CO concentrations at elevated temperatures (at equilibrium). Not only is this unfavorable for practical reasons (i.e. CO poisoning of catalysts), but it robs the hydrogen yield by consuming hydrogen to produce water vapor.

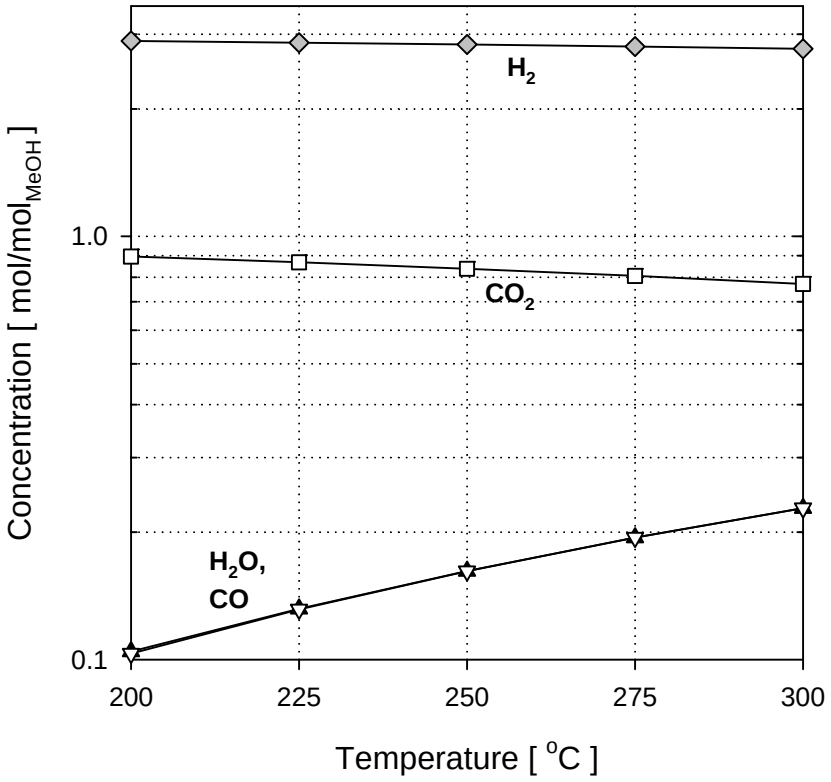

Figure 4.4 The equilibrium concentrations of CO, H_2O, CO_2, and H_2 given in moles per initial moles of methanol fuel (assuming an initial 1:1 mixture of methanol and water vapor) plotted versus temperature (P = 1 atm). Methanol (not shown) is less than 0.001 (mol/mol) for these temperatures.

In a membrane reactor, the removal of hydrogen tends to ameliorate this effect and keeps the reactions heading in the right direction. In Figure 4.5 the number of moles

of each species in the reactor, per mole of fuel initially present, is shown for a reactor with and without a membrane. This allows a clear comparison between the reactor without a hydrogen membrane (solid lines) and with a membrane (dashed lines) where the total concentration is affected by permeation.

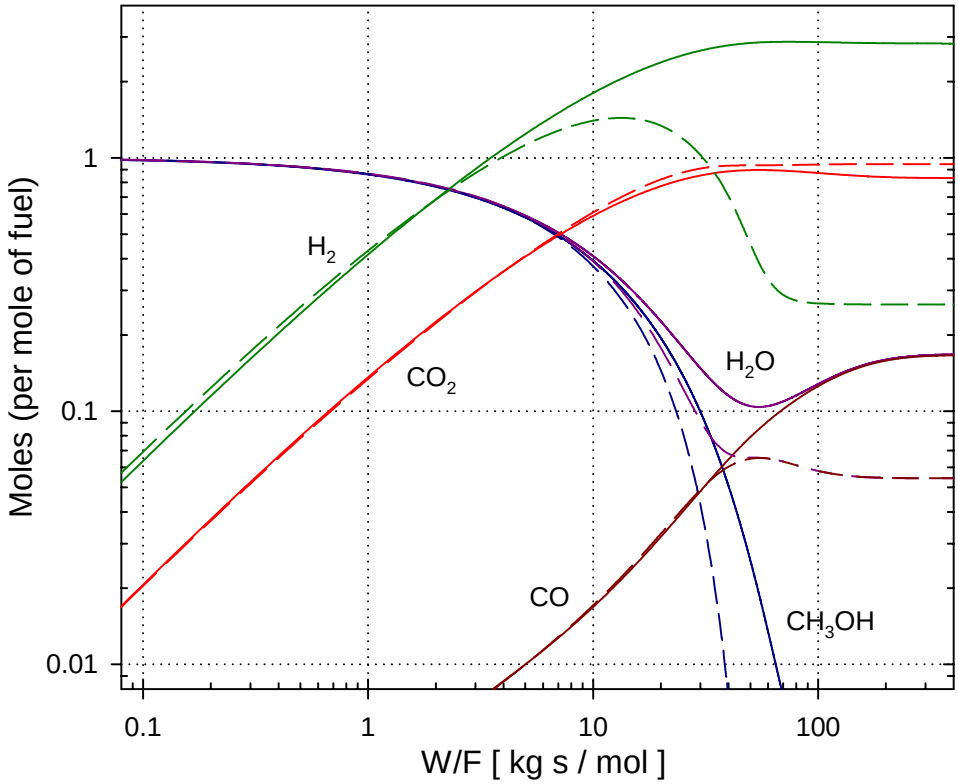

Figure 4.5. Concentration of each component in the reactor relative to the initial quantity of fuel (CH_3OH). The solid lines represent the reactor *without* a hydrogen permeable membrane, and the dashed lines are for the case *with* a membrane.

Initially (at very short times) there is little difference between the two reactors. The steam reforming reaction is still dominant and the WGS reaction reverses as previously described. However, a rising concentration of hydrogen in the reactor drives hydrogen permeation through the membrane and the hydrogen concentration eventually falls. This shift in the equilibrium of the reverse water gas shift reaction reverses it to the forward WGS reaction (see Figure 4.6). Now, CO is being converted to CO_2, and, as

illustrated in Figure 4.5, the CO produced (per mole of methanol) is reduced by nearly two-thirds as compared to the reactor without a membrane.

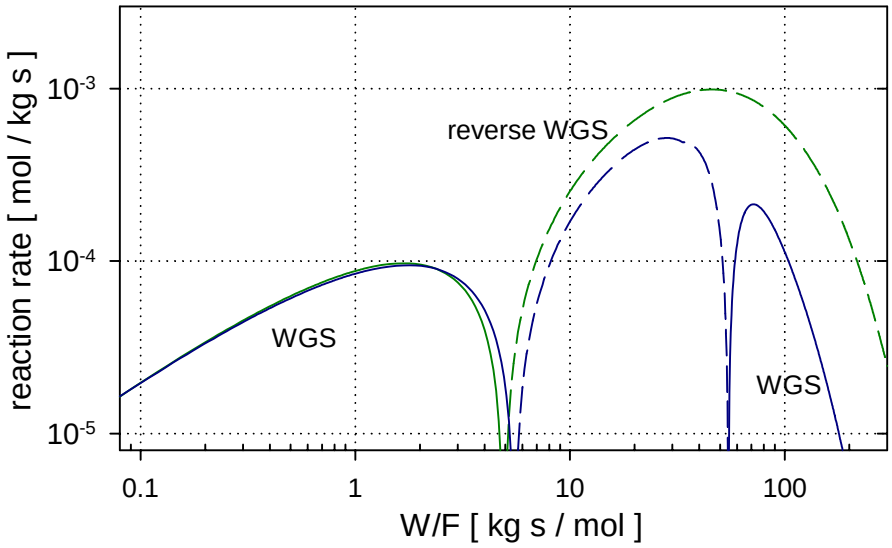

Figure 4.6 Water gas shift reaction rate in the reactor without membrane (upper lines) and with membrane (lower lines). The WGS reaction reverses (dashed lines) in both reactors, but in the membrane reactor, it reverses for a second time back to the forward direction—consuming CO rather than producing it.

Another important feature of Figure 4.5 is the point at which the hydrogen concentration levels off and approaches equilibrium (W/F > 100). Here the batch cycle would be terminated, the reaction chamber discharged, and a fresh batch of fuel brought in. In a well-designed CF reactor, this would correspond to the retentate mixture reaching the end of the flow channel. Qualitatively there is little difference in the transient evolution of the mixture composition and dominant reaction mechanisms for the CHAMP reactor vs. the CF reactor. However, significant differences between the two can be seen quantitatively in the ideal limits of performance assessed in the following section.

4.5.2 Ideal limits of conversion and hydrogen yield

For the baseline case of the ideal CHAMP reactor, the size of the reaction chamber, *H*, was held constant. The other model parameters are given in Table 4.4. The simulations proceed forward in time until conversion has reached at least 99% and the hydrogen yield approaches its theoretical maximum. For the given low-side hydrogen partial pressure of 0.2 atm and a *fixed* reactor volume, the maximum theoretical yield is 86.7%. However, the achievable yield is somewhat lower because of the formation of CO in the reactor. For example, as the hydrogen yield begins to level off (at approximately 84%), the ratio of moles of CO produced to initial moles of reagent mixture is approximately 3.3%. This corresponds to a CO mole fraction of 4.5% in the retentate mixture. The "missing" hydrogen remains in the reactor as water vapor.

Figure 4.7 shows methanol conversion and hydrogen yield efficiency vs. reactant mixture contact, or residence time. Because mass transport resistance between the catalyst layer and the membrane is neglected, the yield curve closely trails the conversion curve. Unlike continuous flow reactors, the pressure in the reaction chamber of the batch reactor is not constant over time but varies as shown in Figure 4.8. Initially, the pressure in the reactor increases because of the increasing number of moles [Eqs. (2.1) and (2.2)]. The pressure peaks when hydrogen production (due to reaction) matches its loss (due to permeation through the membrane). Thereafter, the pressure falls monotonically (dashed line) with continuous net removal of hydrogen approaching the equilibrium state.

In Figure 4.8 (dashed line), the total pressure in the reactor eventually falls below atmospheric pressure as the hydrogen partial pressure approaches its equilibrium value. Because the volume of the reaction chamber is variable, the external atmospheric

pressure could, in principle, move the piston forward maintaining no less than one atmosphere of pressure inside the reactor. This pressure profile is illustrated by the solid line in Figure 4.8, and provides an additional driving force for permeation—shortening the cycle time and increasing the hydrogen yield (solid line in Figure 4.7). With a fixed minimum total pressure of 1.0 atm in the reactor, the maximum theoretical yield is 91.7%. Again, the achievable yield is somewhat lower than this (~89%) because of the formation of CO in the reactor as previously described.

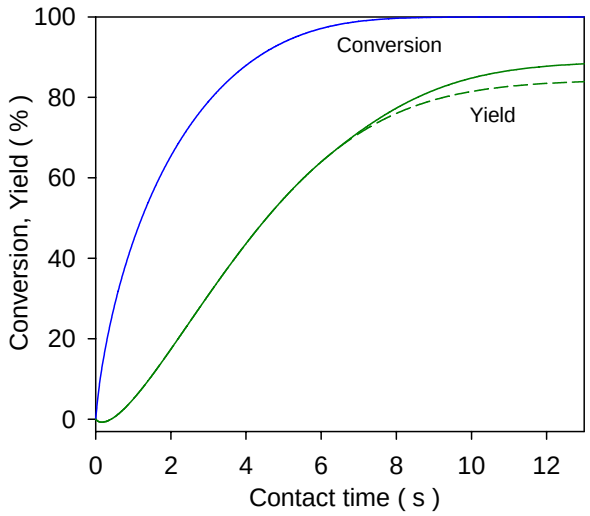

Figure 4.7 Conversion and hydrogen yield vs. contact time for the CHAMP reactor. The hydrogen yield improves slightly when the pressure in the reactor is maintained at no less than atmospheric pressure (solid line).

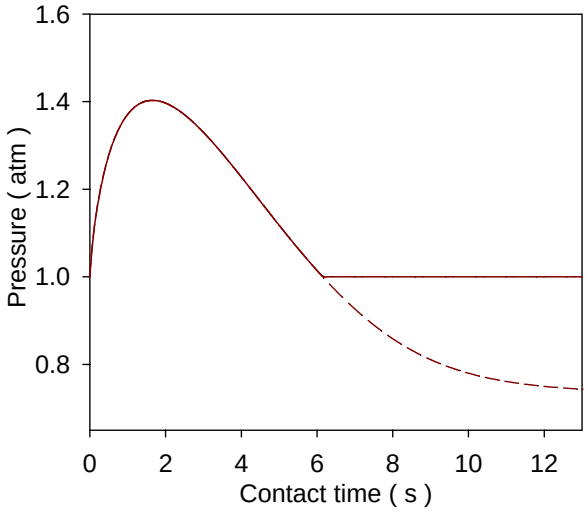

Figure 4.8 Total pressure vs. time in the CHAMP reactor. Atmospheric pressure outside the reactor can be used to keep the pressure inside the reaction chamber from falling (dashed line) below one atmosphere (solid line).

For the continuous flow reactor, the steady-state values of conversion and yield efficiency vary along the length of the channel (Figure 4.9). As mentioned, the pressure in the continuous flow reactor is approximately uniform along the length of the channel (neglecting viscous pressure drop), but the velocity varies to satisfy mass conservation. Figure 4.10 shows the velocity profile along the length of the channel for the same set of parameters given in Table 4.4. Here, the inlet velocity is set to give the same fuel "flow rate" as that in the batch reactor. The batch flow rate is defined as the initial amount of fuel (Eq. (4.2)) divided by the cycle or contact time.

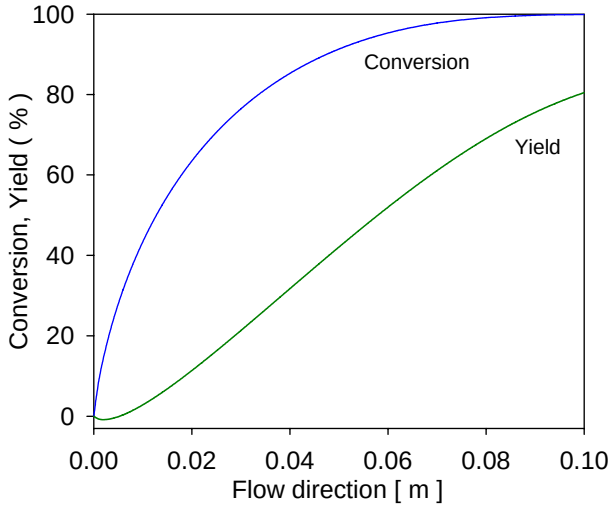

Figure 4.9 Variation in methanol conversion and hydrogen yield along the length of the CF plug-flow reactor

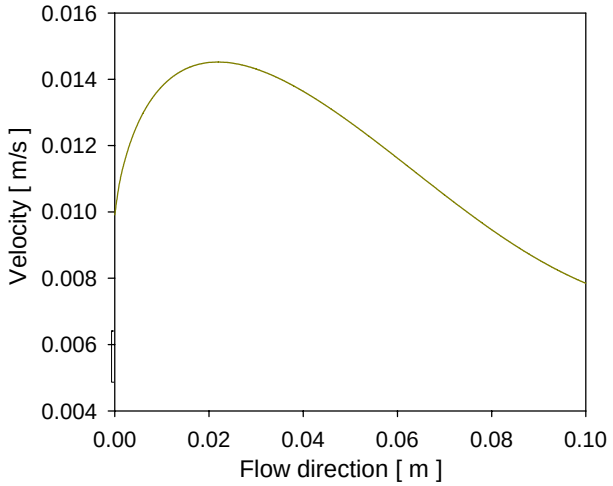

Figure 4.10 Variation of mixture velocity along the length of the CF reactor. The velocity initially increases due to hydrogen production by the reaction, and then decreases due to loss of hydrogen due to permeation through the membrane.

In the batch reactor, the increased pressure (Figure 4.8) due to the increasing number of moles of products is put to work in driving permeation through the membrane. In the CF reactor, this additional mechanical energy (pressure) results in the mixture accelerating down the channel—in essence working *against* the desired goal by shortening the residence time and diminishing permeation of hydrogen through the

membrane. This gives the CHAMP reactor a fundamental advantage over the continuous flow design, by trapping the mixture in the reaction chamber, and using the extra pressure to enhance permeation of hydrogen. Figure 4.11 shows a comparison of hydrogen yield efficiency for the batch and CF reactors for several membrane thicknesses (1, 10, and 50 μm). In the limit of a perfect membrane with zero transport resistance (zero thickness) the performance of both reactors converges.

For example, in the case of a 10 μm thick membrane, the cycle ended after ~10 seconds when 85% hydrogen yield had been achieved. This corresponds to a fuel "flow rate" (defined previously) of 2.366×10^{-3} mol/s (per unit depth). Applying this same fuel flow rate as an input to the CF reactor, with all other parameters held constant, results in a hydrogen yield efficiency of only 80.5% by the time the mixture reaches the end of the channel. To obtain the same hydrogen yield rate as in the batch reactor, the fuel flow rate, or consumption, in the CF reactor would have to be approximately 16% higher (2.745×10^{-3} mol/s) than what is used by CHAMP. Thus, more fuel is consumed for the same power output.

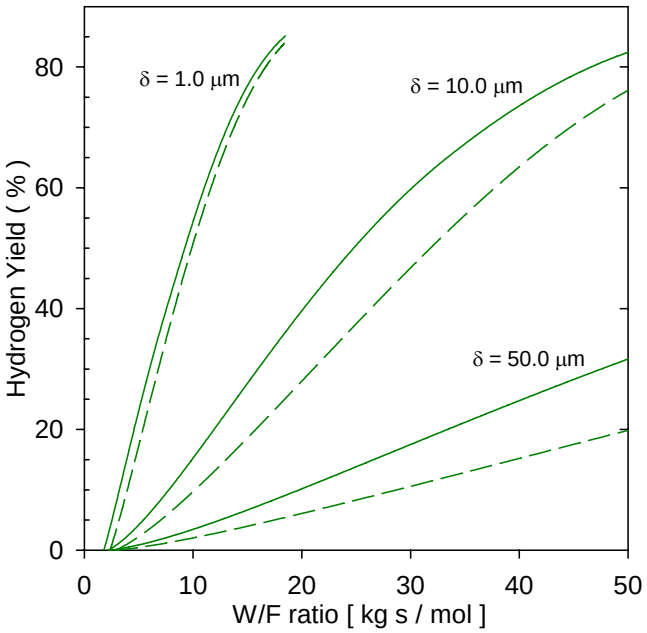

Figure 4.11 Hydrogen yield as a function of weight to fuel (W/F) ratio for the CHAMP (solid line) and continuous flow (dashed line) reactors. With increasing membrane thickness (i.e. increased resistance to permeation) the performance advantage of the CHAMP reactor becomes more pronounced.

For the baseline case just described, the partial pressure of hydrogen on the low side was maintained at 0.2 atm—either by a sweep gas, vacuum, or hydrogen consumption via an appropriate chemical reaction. Another possibility that can be envisioned is operating the reactor at elevated pressures with the permeate side comprising pure hydrogen at atmospheric pressure. Figure 4.12 compares the performance of both reactors (outfitted with the 10 μm thick membrane) when they are operated at 2, 4, and 8 atmospheres of total pressure. As previously described, the pressure in the batch reactor varies throughout the cycle: it starts at the prescribed pressure, increases to its maximum as hydrogen production peaks, then falls back to its initial value. As expected, with high operating pressure, permeation of hydrogen across the membrane is no longer the rate-limiting process and both reactors exhibit similar performance. At lower pressures, however, the CHAMP reactor advantage becomes

increasingly pronounced, because the batch reactor is able to trap the mixture rather than push it out of the open channel.

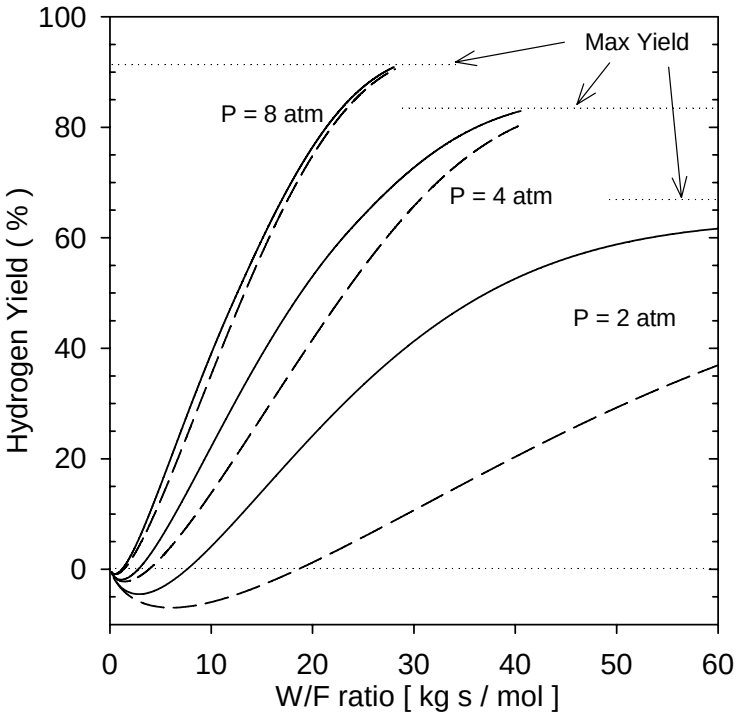

Figure 4.12 Comparison of hydrogen yield by CHAMP reactor (solid line) and CF reactor (dashed line) for various total operating pressures. The maximum yield is determined by the hydrogen partial pressure differential between the permeate and retentate sides of the membrane, which is proportional to the reactor total pressure (hydrogen pressure of 1 atm is assumed on the permeate side).

The difference in performance between the two reactors can be attributed to 1) the ability of the reactor to trap the mixture and control the residence time as required for reaction and, 2) use the increasing number of moles of products (resulting in an increased pressure) to drive permeation through the membrane. If there were no membrane resistance, or the permeation timescale was much faster than the reaction timescale, the CHAMP and CF reactor performances would be identical because as soon as hydrogen is produced, it is immediately removed from the reactor through the membrane. It is the

presence of a resistance to hydrogen transport across the membrane that handicaps the CF reactor, which wastefully allows the mixture to accelerate down the flow channel and out the exit without sufficient residence time for completion of reactions and permeation. If additional resistances (such as bulk gas phase diffusion) are present between the catalyst and the membrane, then more time elapses between production of hydrogen and permeation, and the CHAMP advantage over the CF reactor becomes even greater. Of course, the overall performance of both reactors will be diminished by transport limitations and this is discussed in Chapter 5.

4.5.3 Practical considerations

The results presented here for the idealized reactors can be considered ideal performance limits because 1) the catalytic reactions proceed at their intrinsic rates as predicted by the kinetic model, and 2) the separation of hydrogen is limited only by the intrinsic membrane permeability and the hydrogen partial pressure on either side of the membrane. In a real reactor, heat and mass transfer limitations exist, impeding these rates and penalizing the metrics of reactor performance. Hence, the goal of many traditional designs is to push the reactor performance toward the ideal limit by minimizing transport losses.

The CHAMP reactor has several interesting practical features due to its transient nature. Continuous flow reactors generally respond slowly to changes in operating conditions and only operate optimally at a single flow rate. In contrast, the CHAMP reactor can respond immediately to changing power demands if necessary. For example, the hydrogen yield can be increased mid-cycle simply by compressing the chamber with the piston to drive an increase in permeation without sacrificing fuel conversion

efficiency and hydrogen yield. While this requires additional work, it may be necessary and more optimal under specific circumstances, for example in response to changing power demands.

This is illustrated by Figure 4.13, which shows the hydrogen yield efficiency vs. contact time for the baseline CHAMP reactor case (Case 1, solid line) with no active compression of the piston. A second case (Case 2, dashed line) was run for the same operating conditions; however, three seconds into the cycle, the piston was driven forward at a constant rate of 1.5 mm/s until the end of the cycle. For both cases the simulation was terminated when the hydrogen yield reached 85%. As Figure 4.13 illustrates, the cycle time for Case 2 is approximately 28% shorter than Case 1.

The *gross* power output of the reactor in terms of hydrogen production, or $\dot{W}_{H_2}$, can be estimated by multiplying the rate of hydrogen production per unit surface area of membrane [mol/s-m^2] by the lower heating value (LHV) of hydrogen (119,950 kJ/kg, or 241,820 J/mol [41]). The power requirement for compressing the reacting mixture (per unit surface area of membrane) is $\dot{W}_P = P\frac{dH}{dt}$, or the product of the total pressure and piston velocity. Thus, the *net* power output of the reactor can be found by subtracting the power required for compression from the gross reactor hydrogen output.

Figure 4.14 clearly shows the increase in instantaneous rate of hydrogen permeation when the piston is driven forward during the cycle (Case 2). In practical terms, Case 2 represents the scenario in which the demand for hydrogen (load) increases and the CHAMP reactor is able to immediately respond by producing more hydrogen, mid-cycle. Notice from Figure 4.13 that this is achieved without sacrificing the desired level of hydrogen yield efficiency (85%). If this were attempted in a CF reactor by

increasing the fuel flow rate, hydrogen yield efficiency would necessarily decrease due to the reduced residence time and fuel would be wasted.

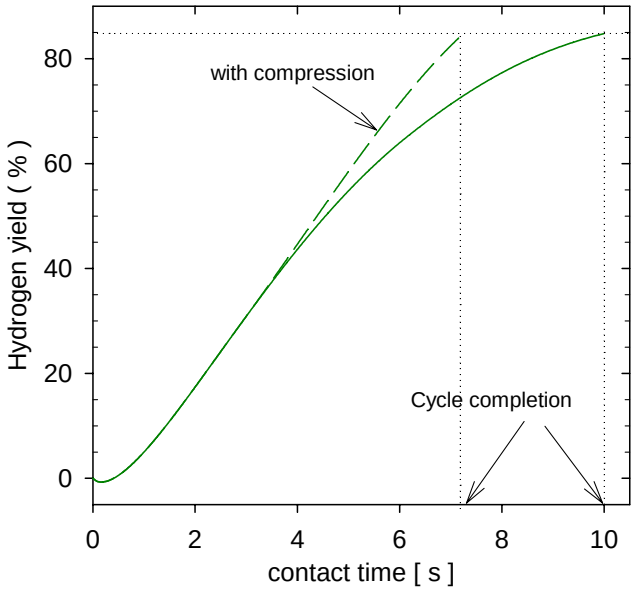

Figure 4.13. Hydrogen yield for the CHAMP reactor under baseline conditions. With active compression of the reaction chamber (Case 2, dashed line), the cycle time is shortened compared to Case 1 (solid line), resulting in rapid increase in rate of hydrogen production without sacrificing reaction yield or fuel conversion efficiency.

Of additional interest is the magnitude of the compression power penalty relative to the power output of the reactor. For Case 2, the power input was, on average, approximately 3% of the gross power output of the reactor. More informative is the ratio of marginal increase in gross power output (Case 2 minus Case 1) to power input required for mixture compression, or, $\frac{\Delta \dot{W}_{H_2}}{\dot{W}_P}$. This represents the "gain" or return on power input, and its value varies throughout the compression stroke as illustrated in Figure 4.15. A gain of much greater than 1 is desirable, especially in real power plants, where the plant power output is less than 100% of the LHV of hydrogen due to system inefficiencies.

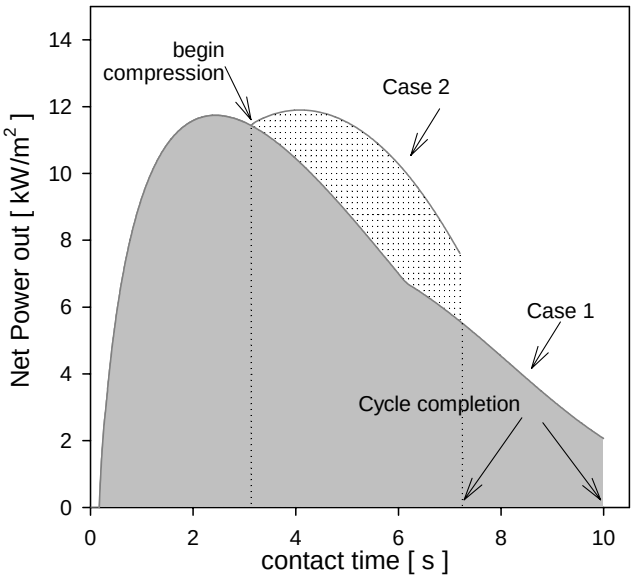

Figure 4.14 Net power output for the baseline case without active compression (Case 1), and the case with mid cycle volume compression by the piston moving at a constant speed (Case 2).

The penalty paid for this enhanced performance is seen in Figure 4.16 which shows the transient pressure profile for both cases. The pressure in the reactor for Case 2 (dashed line) increases dramatically as the chamber is compressed, rather than dropping off as in Case 1 (solid line). The limitation to how quickly hydrogen can be forced out of the reaction chamber, through the membrane, is the mechanical strength of the membrane and reactor, and its ability to withstand elevated pressures.

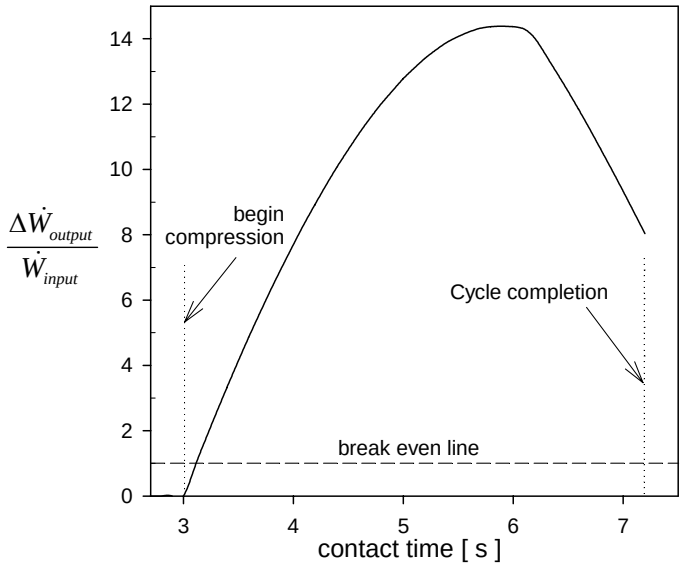

Figure 4.15 Power gain ratio for constant speed mid-cycle volume compression defined as marginal power output (Case 2 minus Case 1) divided by power input required for compression.

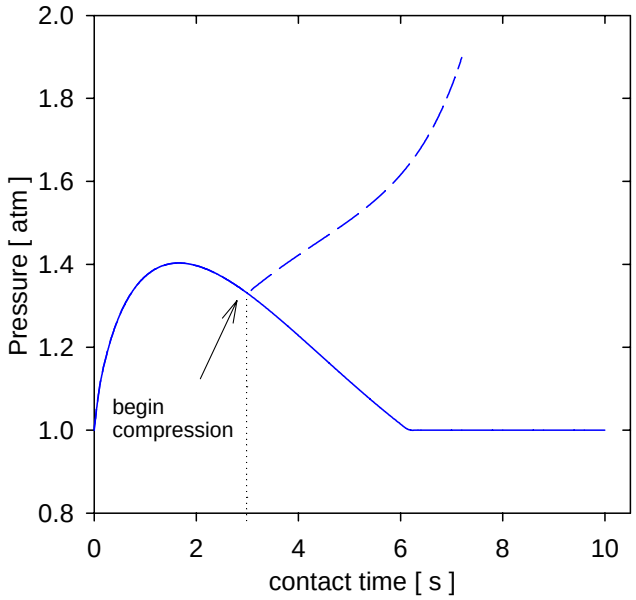

Figure 4.16 The pressure in the reaction chamber increases rapidly as the piston is driven forward (dashed line) during the cycle.

Another practical consideration is the ability to control the thermal conditions in the reactor by applying a time-varying heat source to the catalyst in a spatially uniform fashion, rather than a spatially-varying heat source along the length of the reactor as

necessary for CF operation. It is well-established in the literature [33,35,36] that for CF reactors it is required, but difficult to maintain a sufficiently high temperature near the inlet of the channel where the endothermic steam reforming reaction rate is highest (and consumes the most heat), without supplying too much heat further downstream. This is also because of the significantly higher heat transfer coefficient at the entrance of the reactor, where cold reagents are brought into the reactor. This leads to a non-isothermal environment for the catalytic reactions and diminishes the ability to precisely control the composition of the product stream (particularly the formation of CO, which is favored at higher temperatures).

On the other hand, in the CHAMP reactor, the heat source must be applied in a spatially-uniform fashion, and be controlled in the time domain to match the reaction rate and required heat load during each phase of the reaction cycle. The required heat input is calculated by multiplying the heat of reactions (given in equations (2.1) – (2.3)) and the reaction rates. For the baseline CHAMP reactor parameters, the profile of required heat input is shown in Figure 4.17. Initially, the input is very high and falls in an exponentlial fashion as the reaction rates slow down. For reference, the net power output of the reactor, originally shown in Figure 4.14, is also plotted on Figure 4.17. This transient profile of heat input is similar in shape to the spatial profile of heat input that would be required along the length of the CF reactor. The heat fluxes (< 1 W/cm^2) are modest in magnitude (for example, much lower than those found in thermal management of electronic packages) and practically manageable using combustion products' gas phase heat transfer or integrated electric heating.

In particular, the heat can be supplied by thin film electrical heaters (50 W/cm^2 strip heaters with millisecond response times are commercially available, or even more powerful resistive heaters micro-fabricated via metal deposition [72]) just below the catalyst, or by combustion of fuel and passage of the hot gases through heating channels in intimate contact with the catalyst layer [73]. If the catalyst layer is made sufficiently thin (e.g. 500 μm [61]), it remains nearly isothermal. Supplying the heat spatially as close as possible to the catalyst, and temporally matching the rate it is consumed will minimize its loss to the environment.

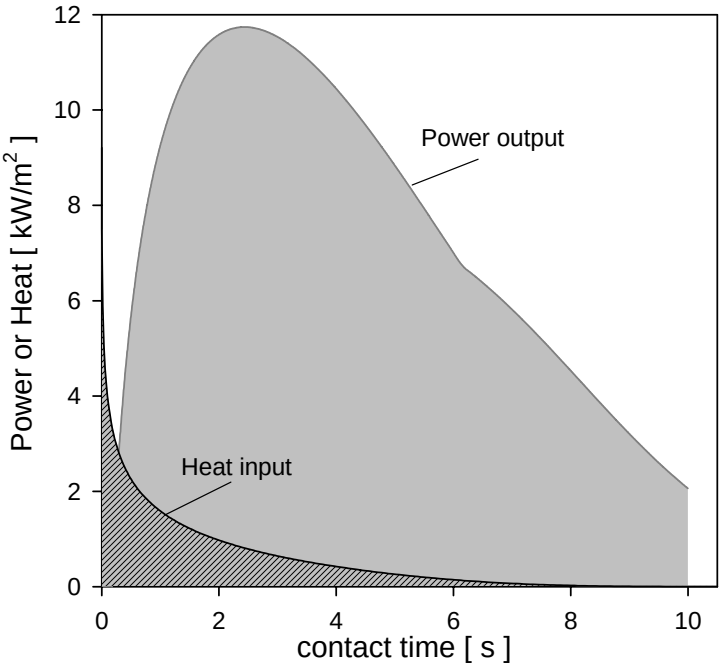

Figure 4.17 Transient profile of heat input required to match the rate of reactions. The power output is calculated by multiplying the rate of hydrogen production by the LHV of hydrogen.

4.6 Concluding remarks

Achieving the level of understanding necessary to identify the design rules for reactor optimization requires development of detailed modeling tools as discussed in the

following chapter. A comprehensive transport-reaction model of the CHAMP reactor was developed to account for interactions between mass transfer, the reaction kinetics, permeation through the membrane, and piston/wall motion that was discussed here. To compliment this theoretical effort, proof-of-concept experimental studies using a bench-top test setup are reported in Chapter 6, validating the theoretical results with test data.

CHAPTER 5

COMPREHENSIVE REACTOR MODEL FORMULATION, RESULTS, AND ANALYSIS

5.1 Model Description

A one-dimensional model of the basic embodiment of the CHAMP reactor was developed for simulating the operating cycle. Three distinct domains (see Figure 5.1) are considered in the reactor: 1) porous catalyst layer on face of piston, 2) reactor volume between the piston and membrane, and 3) hydrogen selective membrane.

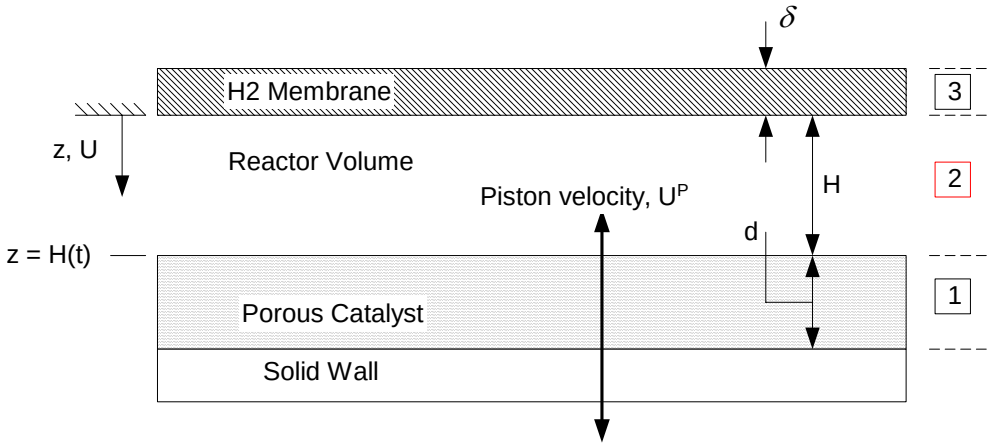

Figure 5.1 Major domains of the CHAMP reactor

5.1.1 Simplifying assumptions

To simplify the analysis for this modeling effort, the following assumptions were made:

- the thin porous catalyst layer is assumed to be isothermal (with sufficient heat supplied to maintain the reactions)
- through the use of the effectiveness factor [74], the catalyst layer can be treated as an impermeable boundary with the reactions occurring at the interface between domains 1 and 2 (Figure 5.1)

- the membrane is assumed to be isothermal, at the same temperature as the catalyst, with no external mass transfer limitations on the “permeate” (low pressure) side of the membrane
- permeation is at quasi steady-state, limited by diffusion through the metallic matrix, and is thus related to the hydrogen partial pressure difference across the membrane following Sievert’s law [51]
- uniform pressure in the reactor
- uniform mass diffusion coefficients for each species based on an “average” mixture composition

These simplifying assumptions allow the reactor to be treated as a single domain (2) with the reaction occurring at the boundary between domains 1 and 2 ($z = H$) and permeation of hydrogen occurring at the other wall ($z = 0$), which is impermeable to all other reaction species.

At the start of a cycle, the reaction chamber is initially filled with methanol and water vapor mixture. These species diffuse to the catalyst surface where they react to form hydrogen, carbon dioxide, and carbon monoxide according to Eqs. (2.1)-(2.3). Hydrogen can permeate in or out of the reactor through the membrane, depending on the direction of the driving force due to the difference between hydrogen partial pressure inside the membrane (at $z = 0$), and that on the permeate side. Piston motion up or down changes the volume, causing a local, proportional, change in the concentration of each species.

5.1.2 Governing equations

The continuity equation for each of the species within the reactor volume (Figure 5.1) is derived by balancing the time rate of change of moles of species *i*, and the net change in species flow rate through a fixed volume:

$$C_i A_c \Delta z\big|_{t+\Delta t} - C_i A_c \Delta z\big|_t = \left[N_i A_c\big|_z - N_i A_c\big|_{z+\Delta z} \right] \Delta t$$
$$\frac{\Delta C_i}{\Delta t} = -\frac{\Delta N_i}{\Delta z} \quad \rightarrow \quad \boxed{\frac{\partial C_i}{\partial t} + \frac{\partial N_i}{\partial z} = 0} \tag{5.1}$$

Here, C_i is the molar concentration of the species *i*, and N_i is the molar flux of species *i* with respect to a fixed-in-space coordinate frame [74]. (Care must be taken to differentiate between quantities that are defined relative to a fixed coordinate system, versus those quantities defined relative to a moving reference frame, such as the moveable face of the piston or the mixture average velocity (see Table 5.1)). The molar flux is defined as the product of the concentration and the molar average velocity of the species *i*, or, $N_i = C_i U_i$. This can also be written as the sum of diffusive and advective components,

$$N_i = J_i + C_i U \tag{5.2}$$

The advective component, $C_i U$, is the flux of species *i* due to the molar average velocity of the mixture, *U*, relative to a fixed reference frame. The diffusive component, J_i, is the molar flux of species *i* relative to a coordinate frame moving with velocity *U*, defined by Fick's law as,

$$J_i = -D_i \frac{\partial C_i}{\partial z} \tag{5.3}$$

The governing equations are obtained by substituting equations (5.2) and (5.3) into equation (5.1),

$$\frac{\partial C_i}{\partial t} + \frac{\partial \left(C_i U \right)}{\partial z} = D_i \frac{\partial^2 C_i}{\partial z^2} \tag{5.4}$$

where D_i is the mass diffusion coefficient for species *i* in the multi-component mixture found in the reaction chamber. The species being considered are A – methanol, B – water vapor, C – carbon dioxide, D – hydrogen, and F – carbon monoxide.

Table 5.1 List of Common Symbols

Symbol	Definition
N_T	Total molar flux of **mixture** relative to a **fixed-in-space** coordinate frame
N_i	Molar flux of **species, *i*,** relative to a **fixed-in-space** coordinate frame
N_i^*	Molar flux of **species, *i*,** relative to a **moving frame** (e.g. piston)
U	Total molar average velocity of **mixture** relative to **fixed** frame
U^*	Total molar average velocity of **mixture** relative to **moving frame**
U_i	Molar velocity of **species, *i*,** relative to **fixed-in-space** coordinate frame
U_P	Velocity of **piston** (boundary at z = H)

The boundary condition for each component at the surface of the membrane (z = 0) is most clearly expressed in terms of molar flux of each species, *i*, relative to the boundary, which happens to be fixed-in-space, using the coordinate system defined in Figure 5.1.

$$\begin{aligned} &N_A\left(z=0,t\right) = N_B\left(z=0,t\right) = N_C\left(z=0,t\right) = N_F\left(z=0,t\right) = 0 \\ &N_D\left(z=0,t\right) = -\frac{D_{memb}}{\delta}\left(P_D^{1/2}\left(z=0\right) - P_{D,\infty}^{1/2}\right) \end{aligned} \tag{5.5}$$

Substituting the definition of flux in Eq. (5.2) into the boundary conditions of Eq. (5.5) yields,

$$
\begin{aligned}
C_A U\big|_{z=0} - D_A \left.\frac{\partial C_A}{\partial z}\right|_{z=0} &= 0; \\
C_B U\big|_{z=0} - D_B \left.\frac{\partial C_B}{\partial z}\right|_{z=0} &= 0; \\
C_C U\big|_{z=0} - D_C \left.\frac{\partial C_C}{\partial z}\right|_{z=0} &= 0; \\
C_D U\big|_{z=0} - D_D \left.\frac{\partial C_D}{\partial z}\right|_{z=0} &= -\frac{D_{memb}}{\delta}\left(P_D^{1/2}\left(z=0\right) - P_{D,\infty}^{1/2}\right); \\
C_F U\big|_{z=0} - D_F \left.\frac{\partial C_F}{\partial z}\right|_{z=0} &= 0;
\end{aligned}
\tag{5.6}
$$

The boundary condition at the catalyst surface ($z = H$) is defined in terms of the flux of species, *i*, relative to the moveable boundary, due to the consumption (positive flux, relative to *z*) or production (negative flux) of a product via the reactions,

$$
N_i^*\left(z = H\left(t\right), t\right) = \sum_j \dot{R}''_{gen,i,j} \tag{5.7}
$$

As previously described in Chapter 4, the kinetic model of Peppley [61] gives the rates of reaction for steam reforming, r_{SR}, methanol decomposition, r_d, and water gas shift, r_{WGS}. Substituting the definition for flux, Eq. (5.2), into the boundary condition, Eq. (5.7), yields the following expressions for each component,

$$
\begin{aligned}
C_A U^*\big|_{z=H(t)} - D_A \left.\frac{\partial C_A}{\partial z}\right|_{z=H(t)} &= \rho_{cat} d\left(r_{SR} + r_d\right); \\
C_B U^*\big|_{z=H(t)} - D_B \left.\frac{\partial C_B}{\partial z}\right|_{z=H(t)} &= \rho_{cat} d\left(r_{SR} + r_{WGS}\right); \\
C_C U^*\big|_{z=H(t)} - D_C \left.\frac{\partial C_C}{\partial z}\right|_{z=H(t)} &= \rho_{cat} d\left(-r_{SR} - r_{WGS}\right); \\
C_D U^*\big|_{z=H(t)} - D_D \left.\frac{\partial C_D}{\partial z}\right|_{z=H(t)} &= \rho_{cat} d\left(-3r_{SR} - r_{WGS} - 2r_d\right); \\
C_F U^*\big|_{z=H(t)} - D_F \left.\frac{\partial C_F}{\partial z}\right|_{z=H(t)} &= \rho_{cat} d\left(-r_d + r_{WGS}\right);
\end{aligned}
\tag{5.8}
$$

Here, ρ_{cat} is the density of the catalyst, *d* is the thickness of the porous catalyst layer, and *H* is the time-dependent distance between the piston and membrane, $H(t) = H_0 + \int_{t^*}^{t} U_P dt$, for a piston moving with velocity $U_P = f(t)$. The mixture velocity relative to the boundary, U^* is related to the absolute mixture average molar velocity, *U*, by the piston velocity, that is, $U^* = U - U_P$.

The initial conditions for the set of governing equations (5.4) are,

$$\begin{aligned} &C_A(z, t=0) = C_B(z, t=0) = 0.5\frac{P_{initial}}{RT}; \\ &C_C(z, t=0) = C_D(z, t=0) = C_F(z, t=0) = 10^{-4}; \left[mol/m^3\right] \end{aligned} \tag{5.9}$$

The small initial amounts of carbon dioxide, hydrogen, and carbon monoxide are provided to avoid singularities in the kinetic expressions at very short times. In addition to the unknown transient concentration profiles of each of the five species within the reactor, a sixth unknown, the molar average velocity of the mixture, *U*, must also be determined.

The molar average mixture velocity, *U*, required to complete the formulation is found from the continuity of the total mixture under the condition of uniform pressure in the reactor. This is derived by balancing the time rate of change of the number of moles in the reactor and the net flow of the mixture into and out of the reactor:

$$\frac{dC_T}{dt} + \frac{dN_T}{dz} = 0 \tag{5.10}$$

Here, C_T is the total molar concentration of the mixture, and N_T is the molar flux of the mixture, given by $N_T = C_T U$. Substitution of this expression into equation (5.10) yields the continuity equation for the total number of moles of mixture within the reactor,

$$\frac{dC_T}{dt} + \frac{d\left(C_T U\right)}{dz} = 0 \tag{5.11}$$

It should be noted that Eq. (5.11) can also be obtained by summing up the species transport equations (5.4) for individual species, and using linearity of equations to re-arrange:

$$\begin{aligned}\sum_{i=1}^{n}\left[\frac{\partial C_i}{\partial t} + \frac{\partial\left(C_i U\right)}{\partial z} = -\frac{\partial\left(J_i\right)}{\partial z}\right] &= \left[\frac{\partial\left(\sum_{i=1}^{n} C_i\right)}{\partial t} + \frac{\partial\left(U\sum_{i=1}^{n} C_i\right)}{\partial z} = -\frac{\partial\left(\sum_{i=1}^{n} J_i\right)}{\partial z}\right] \\ &= \left[\frac{\partial C_T}{\partial t} + \frac{\partial\left(C_T U\right)}{\partial z} = -\frac{\partial\left(\sum_{i=1}^{n} J_i\right)}{\partial z}\right]\end{aligned} \tag{5.12}$$

By definition [72] the sum of the diffusive terms must be zero, i.e. $\sum_{i=1}^{n} J_i = 0$, and Eq. (5.12) is reduced to Eq. (5.11).

The assumption of spatially uniform pressure (pressure equilibrates at the speed of sound, much faster than process timescales) within the reactor chamber allows the simplified form,

$$\frac{dC_T}{dt} + C_T \frac{dU}{dz} = 0 \tag{5.13}$$

The only unknown in this equation is the molar average velocity, *U*. The total concentration is the sum of the five component concentrations, and the time rate of change of concentration is found by balancing the number of moles in the entire reactor volume, considering all the sources (due to reaction) and sinks (due to permeation losses):

$$C_T A_c H\big|_{t+\Delta t} - C_T A_c H\big|_t = \left(\left(C_T UA\right)_{inlet} - \left(C_T UA\right)_{outlet} + R_{gen,Rxn} - R_{loss,perm}\right)\Delta t \tag{5.14}$$

When the inlet and outlet of the reactor are closed (as in the case of the CHAMP batch reactor with all intake/exhaust valves closed), the first two terms in the right-hand-side of equation (5.14) vanish. The net rate of molar generation (production) is found by summing all the rates of production for each species (given in the boundary conditions of Eq. (5.8)) yielding, $R_{gen,Rxn} = \rho_{cat} A_c d\left(2r_{SR} + 2r_d\right)$ while the net loss of moles due to hydrogen permeation through the membrane is $R_{loss,perm} = \frac{D_{memb}}{\delta} A_c \left(P_D^{1/2}\left(z=0\right) - P_{D,\infty}^{1/2}\right)$.

With these simplifications, the mole balance equation (5.14) is reduced to

$$\begin{aligned} C_T H\big|_{t+\Delta t} - C_T H\big|_t &= \left(\rho_{cat} d\left(2r_{SR} + 2r_d\right) - \frac{D_{memb}}{\delta}\left(P_D^{1/2}\left(z=0\right) - P_{D,\infty}^{1/2}\right)\right)\Delta t \\ \frac{d\left(C_T H\right)}{dt} &= \rho_{cat} d\left(2r_{SR} + 2r_d\right) - \frac{D_{memb}}{\delta}\left(P_D^{1/2}\left(z=0\right) - P_{D,\infty}^{1/2}\right) \\ C_T \frac{dH}{dt} + H\frac{dC_T}{dt} &= \rho_{cat} d\left(2r_{SR} + 2r_d\right) - \frac{D_{memb}}{\delta}\left(P_D^{1/2}\left(z=0\right) - P_{D,\infty}^{1/2}\right) \end{aligned} \qquad (5.15)$$

The final expression then, for the time rate of change of the total concentration in the reactor is:

$$\frac{dC_T}{dt} = \frac{1}{H}\left[\rho_{cat} d\left(2r_{SR} + 2r_d\right) - \frac{D_{memb}}{\delta}\left(P_D^{1/2}\left(z=0\right) - P_{D,\infty}^{1/2}\right) - C_T\frac{dH}{dt}\right] \qquad (5.16)$$

Upon substitution of equation (5.16) into the continuity equation [Eq. (5.13)], and remembering that the total concentration is assumed to be spatially uniform, equation (5.13) can be readily integrated in space (z-coordinate) at any given moment of time, resulting in a linear molar average velocity profile,

$$U\left(z\right) = -\frac{1}{C_T}\frac{dC_T}{dt} z + constant \qquad (5.17)$$

The constant of integration is found by applying either of the two boundary conditions, at $z=0$ or $z=H(t)$. For example, if $z=0$ is chosen, the total molar flux relative to the boundary (fixed-in-space) is given by,

$$N_T^*\big|_{z=0} = -C_T U\big|_{z=0} = \frac{D_{memb}}{\delta}\left(P_D^{1/2}(z=0) - P_{D,\infty}^{1/2}\right) \tag{5.18}$$

Therefore, the molar average velocity at $z=0$ is,

$$U\big|_{z=0} = -\frac{D_{memb}}{C_T\delta}\left(P_D^{1/2}\big|_{z=0} - P_{D,\infty}^{1/2}\right) \tag{5.19}$$

and substitution of this into equation (5.17) yields the distribution of molar average velocity across the reactor:

$$\begin{aligned} U(z) = -\frac{1}{H}\Bigg[&\frac{\rho_{cat} d\left(2r_{SR}+2r_d\right)}{C_T} - \frac{D_{memb}}{C_T\delta}\left(P_D^{1/2}(z=0) - P_{D,\infty}^{1/2}\right) - \frac{dH}{dt}\Bigg] z \\ &- \frac{D_{memb}}{C_T\delta}\left(P_D^{1/2}\big|_{z=0} - P_{D,\infty}^{1/2}\right); \end{aligned} \tag{5.20}$$

Notice, that because the slope of the velocity profile includes information from both boundaries (it was derived based on mass conservation for the total number of moles, Eqs. (5.14)-(5.16), which utilized information at both boundaries to compute dC_T/dt), the velocity profile in Eq. (5.20) automatically yields the correct value at the other boundary, $z=H(t)$.

For example, the total molar flux at the boundary $z=H(t)$ relative to the moving boundary is,

$$N_T^*\big|_{z=H(t)} = C_T U^*\big|_{z=H(t)} = \rho_{cat} d\left(2r_{SR}+2r_d\right) \tag{5.21}$$

yielding the molar average velocity (relative to the boundary)

$$U^{*}\Big|_{z=H(t)} = \frac{\rho_{cat} d\left(2r_{SR} + 2r_d\right)}{C_T} \tag{5.22}$$

Since the boundary (and the mixture next to the boundary) is moving with the piston velocity, $U^P = \frac{dH}{dt}$, the total molar average velocity relative to a fixed-in-space coordinate (U) is the sum of the velocity relative to the moving boundary, eq. (5.22), and the piston velocity (U^P),

$$U\Big|_{z=H(t)} = \frac{dH}{dt} - \frac{\rho_{cat} d\left(2r_{SR} + 2r_d\right)}{C_T} \tag{5.23}$$

This expression is identical to that found by substituting $z = H(t)$ into equation (5.20).

Alternatively, equation (5.23) could be substituted into equation (5.17) to find the distribution of molar average velocity along the length of the reactor:

$$\begin{aligned} U(z) = \frac{1}{H}\left[\frac{\rho_{cat} d\left(2r_{SR} + 2r_d\right)}{C_T} - \frac{D_{memb}}{C_T \delta}\left(P_D^{1/2}(z=0) - P_{D,\infty}^{1/2}\right) - \frac{dH}{dt}\right](H - z) \\ + \frac{dH}{dt} - \frac{\rho_{cat} d\left(2r_{SR} + 2r_d\right)}{C_T}; \end{aligned} \tag{5.24}$$

Notice that this expression is consistent with the expression for velocity at $z = 0$ [equation (5.19)].

The mass diffusion coefficients were calculated via the semi-empirical equation of Gillilland [74] for calculating binary diffusion coefficients, D_{AB}. The coefficients were calculated for each combination of pairs of species found in the mixture, i.e. methanol/water vapor, methanol/carbon dioxide, methanol/hydrogen, water vapor/carbon dioxide, etc. For multi-component mixtures, the diffusion coefficient of a species through the mixture, $D_{i,m}$, varies with composition, as well as molar flux of each component. An approximate value for the multi-component diffusion coefficient can be

obtained by assuming that species, A, for example, is diffusing through a stagnant mixture of A, B, C, D, and F, which is calculated from [74],

$$D_{Am} = \frac{1 - x_A}{x_B / D_{AB} + x_C / D_{AC} + x_D / D_{AD} + x_F / D_{AF}} \tag{5.25}$$

This value was calculated for each component diffusing through the mixture using an average mixture composition in the reactor corresponding to 50% methanol conversion. These average values were used for D_i in Eqs (5.4) - (5.8) above, and the numerical values calculated at baseline (reference) temperature and pressure are given in Table 5.2. Also shown are the extreme values of the diffusion coefficient at 0% and 100% conversion. The diffusivities were adjusted in the model for the reactor's temperature and pressure according to the predictions of kinetic theory, $\left(T/T_{ref}\right)^{3/2}$ and P_{ref}/P.

Table 5.2. Baseline Diffusion Coefficients

Species, *i* (250 °C; 1 atm)	**Multi-component diffusion coefficient,** $D_{i,m}$ 50% MeOH conversion (0 – 100 %); [m^2/s]
Methanol	5.5e-5 (4.1 – 6.0 e-5)
Water Vapor	7.2e-5 (4.1 – 9.0 e-5)
Carbon Dioxide	5.6e-5 (3.2 – 9.5 e-5)
Hydrogen	12.1e-5 (12.4 – 11.7 e-5)
Carbon Monoxide	5.3e-5 (3.7 – 7.0 e-5)

5.1.3 Solution method

Because these transient equations cannot be solved analytically, the solution was obtained numerically using a finite difference approach. The time derivative for a given species concentration at each node location, *i*, (*i* = 1, 2, …, M) was approximated by the forward difference method, that is,

$$\frac{\partial C_i}{\partial t} \approx \frac{C_i^{n+1} - C_i^n}{\Delta t} \tag{5.26}$$

where the index *n* refers to the present time and *n* +1 refers to the next time step. The advective flux gradient term was approximated using a first order upwind scheme, which is written as,

$$\frac{\partial\left(C_i U_i\right)}{\partial z} \approx \beta \frac{C_i^{n+1} U_i^{n+1} - C_{i-1}^{n+1} U_{i-1}^{n+1}}{\Delta z} + \left(1-\beta\right) \frac{C_i^{n} U_i^{n} - C_{i-1}^{n} U_{i-1}^{n}}{\Delta z} \tag{5.27}$$

for example, when the velocity magnitude is positive relative to the coordinate, z. The coefficient β varies between zero (fully explicit) and one (fully implicit). For values of β greater than or equal to 0.5, the solution is unconditionally stable and first-order accurate. The diffusion term was approximated using the centered difference scheme,

$$\frac{\partial^2 C_i}{\partial z^2} \approx \beta \frac{C_{i+1}^{n+1} - 2C_i^{n+1} + C_{i-1}^{n+1}}{\Delta z^2} + \left(1-\beta\right) \frac{C_{i+1}^{n} - 2C_i^{n} + C_{i-1}^{n}}{\Delta z^2} \tag{5.28}$$

This set of M equations for each species at the given time step is expressed in matrix form as (e.g. methanol),

$$\left[\mathbf{K_A}\right]\mathbf{C_A^{n+1}} = \mathbf{r_A} \tag{5.29}$$

Where $\mathbf{C_A^{n+1}}$, the M *x* 1 vector of unknown concentrations of methanol at the next time step, is found by inverting the tri-diagonal M *x* M coefficient matrix $\left[\mathbf{K_A}\right]$ and multiplying it by the right-hand side vector, $\mathbf{r_A}$ which contains known information from the current time step.

The following procedure for numerically solving these equations was implemented in the C computer language.

1. The kinetic reaction rates, hydrogen permeation rate, and mixture velocity at the present time were calculated from present (initial) conditions. This also serves as the first guess for these values at the next time step.

2. The coefficient matrix for each species was populated and inverted using the tri-diagonal matrix algorithm (TDMA) [75].
3. The unknown concentrations at the next time step were calculated, and these values allowed a recalculation (Step 1) of the reaction rates, etc. at the next time step.
4. Iterate from Step 1 to 3 until the reaction rates, permeation rate, mixture velocity and species concentrations at the next time step have converged to a solution.
5. Proceed to the next time step and return to Step 1.
6. The simulations terminate when a specified level of methanol conversion has been reached and/or a specified level of hydrogen yield efficiency has been achieved.

Several tests were conducted to validate the code: 1) the numerical solution to the equations was shown to be independent of the mesh and time step using a discretization of 100 nodes, and time step of 0.001 seconds, 2) the total mass of each element (H, C, and O) was monitored to ensure that the calculations did not violate mass conservation, and 3) the condition of spatially uniform pressure, which was indirectly enforced through the mixture velocity calculation, was checked after the fact to ensure that it still held true.

Additionally, the numerical results were validated by comparison to the semi-analytical model results presented in Chapter 4 (ideal limit of no mass transport limitations in the bulk gas phase, $D_i \to \infty$). This was done by setting the mass diffusion coefficients in the mass transfer model here to artificially large values (several orders of magnitude larger than reality) and simulating several scenarios:

Case 1. With no membrane permeation and no piston motion, the time varying concentration of each species (as in Figure 5.3) was calculated to validate the correct implementation of the reaction kinetic expressions.

Case 2. For a fixed reactor volume (no piston motion) the hydrogen yield versus time (as in Figure 5.6) was calculated to validate the combined reaction/permeation results.

Case 3. With no reactions and no permeation, the pressure change due to compression of the volume by the piston was compared to the analytical solution (assuming an ideal gas), $P(t) = P_0 H_0 / H(t)$

These special cases served to demonstrate the validity of the code, showing excellent agreement between the analytical (or semi analytical) solutions and the complete numerical solution of the five coupled, partial differential equations [Eq. (5.4)] subject to the boundary and initial conditions given in Eqs. (5.6) - (5.9), and the continuity equation, (5.13).

5.2 Model Results

The baseline set of parameters for the CHAMP design and operation are the same as those given in Table 4.4. The first item of interest in understanding the dynamics of the coupled reaction, transport, permeation, and compression processes is the transient evolution of the component concentration profiles as the fuel is consumed and hydrogen permeates the membrane. Figure 5.2 shows concentration profiles of methanol and hydrogen in a constant volume reactor. At very short times, the methanol concentration near the catalyst drops very rapidly with a corresponding rapid increase in hydrogen. The increasing total number of moles near the catalyst pushes the mixture away from the wall,

in order to maintain a uniform pressure in the reactor. Evidence of this is seen by the temporary methanol peak near the center of the reactor which is greater in magnitude than the initial concentration (11.6 mol/m^3). At the membrane, back-permeation of hydrogen has the same effect, pushing the mixture towards the center of the reactor. When sufficient hydrogen has been generated by the reactions and has had time to diffuse across the reactor to the surface of the membrane, the elevated hydrogen partial pressure drives permeation forward and out of the reactor.

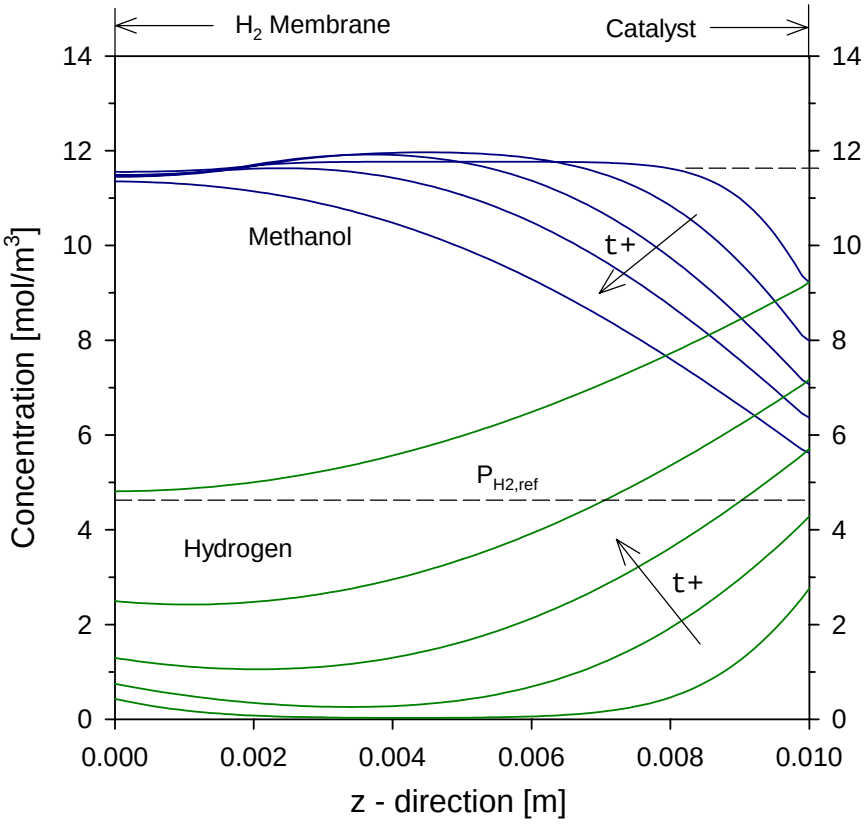

Figure 5.2 Methanol and hydrogen concentration profiles at very short times (< 0.5 s) within the reactor volume. The hydrogen partial pressure outside the membrane corresponds to a concentration of 4.6 mol/m^3, indicated by the lower dashed line, and the initial methanol concentration is 11.6 mol/m^3.

The complete evolution of methanol and hydrogen concentration profiles from t = 0 to very near equilibrium is shown in Figures 5.3 and 5.4, respectively. Methanol

conversion greater than 99% is reached after approximately 10 seconds. Equilibrium for hydrogen requires more time because permeation is delayed initially by diffusion within the reactor chamber, and the molar quantity of hydrogen produced is approximately three times that of the initial methanol. After approximately 16 seconds the hydrogen yield efficiency (defined in Chapter 4) is nearly 85% (the ideal limit is 86.6%).

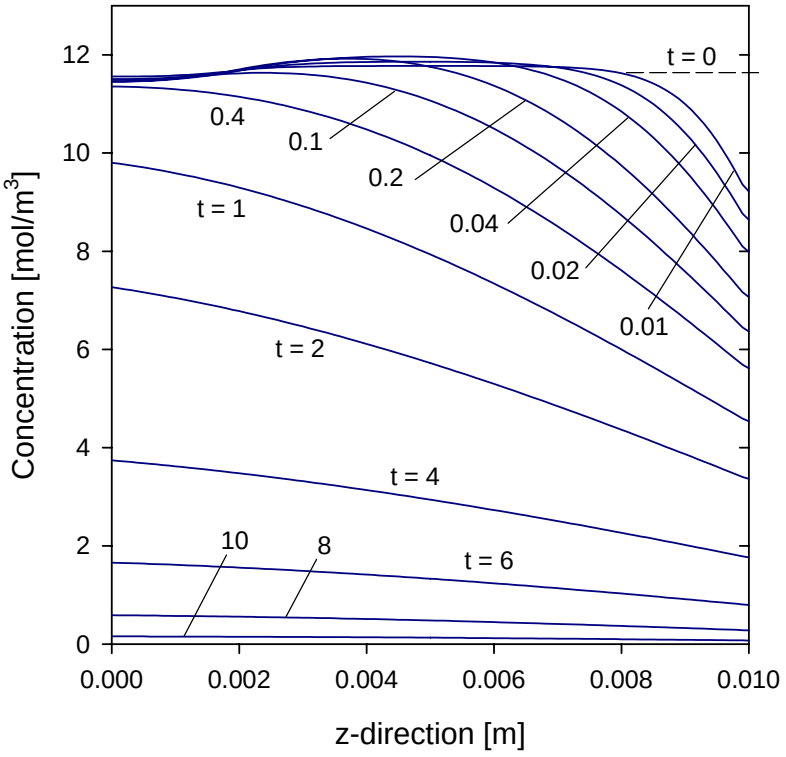

Figure 5.3 Time evolution of the methanol concentration profile.

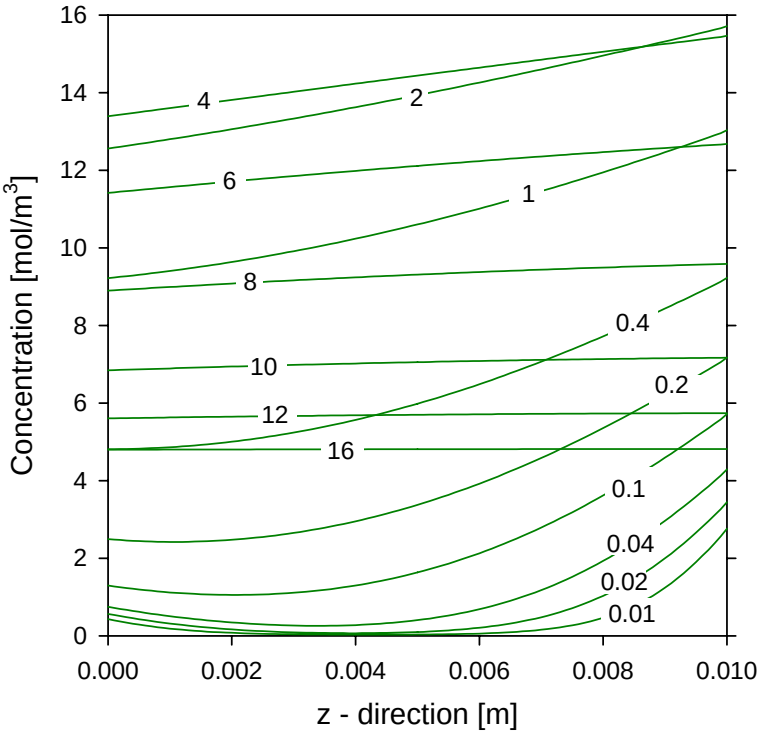

Figure 5.4 Time evolution of the hydrogen concentration profile

The effects of mass diffusion limitations can be seen in Figure 5.5 which shows model predictions of methanol conversion and hydrogen yield vs. time for the baseline CHAMP reactor. The limiting case, in the absence of transport limitations (Chapter 4), is indicated on the figure as the ideal limit. As expected, the presence of diffusion limitations slows down both the rate of conversion and the rate of hydrogen yield in a 'real' reactor. However, the qualitative aspects of the performance remain the same. For a short time near the beginning of the cycle, hydrogen yield initially is negative due to back-permeation through the membrane into the reaction chamber. Eventually the hydrogen partial pressure at the surface of the membrane provides a sufficient driving force for forward permeation. Then, as the hydrogen becomes depleted, the yield asymptotically approaches its ideal limit, which in this case is 86.6% (due to the non-zero hydrogen partial pressure on the permeate side of the membrane).

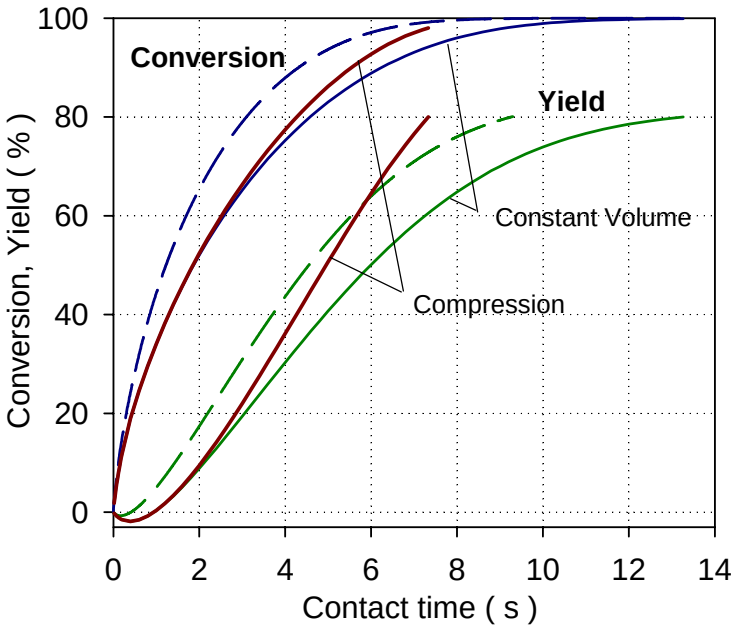

Figure 5.5 Methanol conversion and hydrogen yield vs. time in the CHAMP reactor. The ideal limits (dashed lines) are in the absence of diffusion limitations. The cycle is complete when hydrogen yield reaches 80%. For compression, the piston was moved forward after 1 second, at the constant rate of 1 mm/s until the end of the cycle.

To illustrate a variable-volume mode of operation, the piston is moved forward during the cycle, compressing the volume and driving the permeation rate higher as a result of elevated hydrogen partial pressure and diminished mass transfer resistance across the bulk of the reaction chamber. In the case shown in Figure 5.5, the piston was moved forward after 1 second at a uniform rate of 1.0 *mm*/*s* until the end of the cycle (defined as 80% hydrogen yield). The final reactor size, *H*, was 3.7mm. This results in almost 50% shorter cycle time, or a near doubling of specific power as seen in Figure 5.5. More importantly, this did not come at the expense of fuel utilization—in both cases, more than 99% of the methanol was consumed, and the same criterion of 80% hydrogen yield was achieved.

This does, however, come at the expense of increased total pressure in the reactor, as illustrated in Figure 5.6. The maximum pressure in the constant-volume reactor is less

than 1.4 atm; but with compression by the piston, the pressure continues to increase and approaches 2 atm. Maximum allowable pressure is an important practical consideration in the design and operation of the reactor. Keeping the pressure below some maximum threshold during a cycle requires a careful matching of the characteristic timescales for reaction, diffusion, permeation and compression within the reaction chamber. Therefore, it is instructive to assess the relative magnitudes of these process timescales and use this knowledge to guide the optimal design and optimal method of operation of the CHAMP reactor.

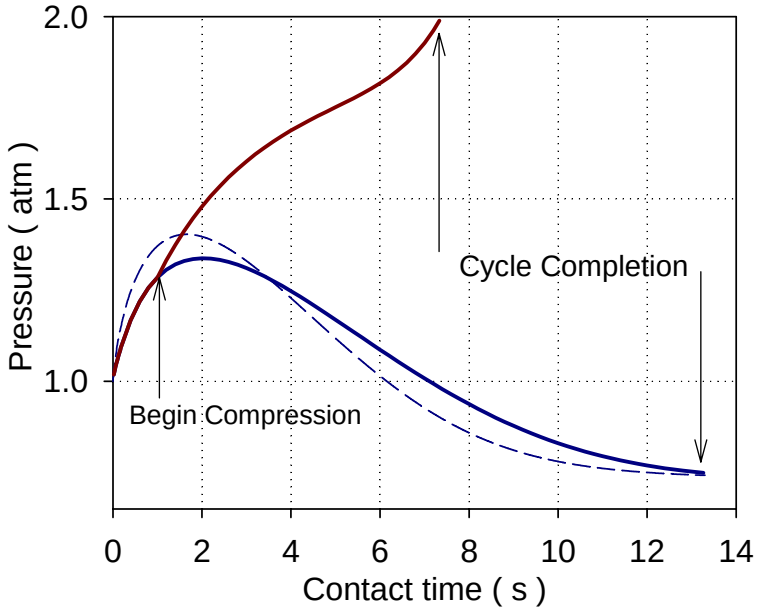

Figure 5.6 Profiles of pressure vs. time within the reactor. The ideal case (dashed line) is in the absence of diffusion limitations. With compression of the volume by the piston (same as Figure 5.5), the pressure rises, driving a higher rate of permeation or power output.

5.3 Analysis

5.3.1 Characteristic timescales and rate limiting steps

Reaction:

The rate of disappearance of methanol roughly follows an exponential decay, $\exp\left[-t/\tau_{Rxn}\right]$, where τ_{Rxn} is the reaction characteristic time constant. When $t=\tau_{Rxn}$ the methanol conversion is approximately 63.2% or $1-1/e$. Therefore the characteristic time scale for the reaction, τ_{Rxn}, will be defined as the time required for methanol conversion to reach 63%. This is also known as the *e-folding* time, 1/*e*. To calculate τ_{Rxn} it is assumed that diffusion and permeation are much faster than the reaction, i.e. $\tau_{Perm}, \tau_{Diff} << \tau_{Rxn}$. Thus, the partial pressure of hydrogen in the reactor is uniform and equal to the low side partial pressure, P_{H2}^{∞}, on the permeate side. The reactor is filled with the fuel mixture, and when conversion reaches 63%, the time is recorded as τ_{Rxn}.

Permeation:

The rate of disappearance of hydrogen (by permeation through the membrane) can also be assumed to follow an exponential decay, $\exp\left[-t/\tau_{Perm}\right]$, where τ_{Perm} is the permeation characteristic time constant. If the reaction timescale is much faster then the permeation timescale $\tau_{Rxn} << \tau_{Perm}$, then the membrane immediately sees an equilibrium mixture of roughly 3:1 hydrogen to carbon dioxide (via steam reforming of methanol). For a low side partial pressure of P_{H2}^{∞} the maximum hydrogen yield efficiency is $\gamma_{H2}^{\max}=\dfrac{0.75\left(2P_{initial}\right)-P_{H2}^{\infty}}{0.75\left(2P_{initial}\right)}$. When $t=\tau_{Perm}$ the hydrogen yield efficiency is 63.2% of its maximum value, or $\left(1-1/e\right)\gamma_{H2}^{\max}$. Therefore the characteristic time scale for permeation,

τ_{Perm}, is defined as the time required for the hydrogen yield to reach 63% of the maximum possible hydrogen yield (when the reactor is initially filled with a 3:1 H_2:CO_2 mixture at $P_{initial}$).

Diffusion:

The bulk gas phase diffusion timescale is defined as $\tau_D = H^2 / D_m$, where H is the size of the reactor, and D_m is the average of the multi-component mass diffusion coefficients for the reaction mixture.

Figure 5.7 illustrates the variation in these timescales as temperature varies from 200-300 °C. The solid lines are the reaction timescale which is seen to have a heavy dependence on temperature. The three solid lines represent three different thicknesses of catalyst layer, 100, 250, and 500 μm, from upper line to lower line, respectively. The size of the reaction chamber, *H*, is fixed at 1 cm. The low side partial pressure of hydrogen is 0.2 atm and the permeation occurs so quickly that the partial pressure of hydrogen inside the reactor is always 0.2 atm.

The dashed lines in Figure 5.7 represent the timescale for permeation as described above. The size of the reaction chamber, *H*, is fixed at 1 cm, the low side partial pressure of hydrogen is 0.2 atm, and the thickness of the membrane is 1, 10, and 50 μm, from lower to upper line, respectively. The reaction was assumed instantaneous so that the initial conditions were 1.5 moles of hydrogen, 0.5 moles of carbon dioxide, and initial total pressure of 2.0 atm.

The dotted line in Figure 5.7 is the approximate diffusion timescale for the reactor of size, H = 1 cm.

A typical operating point, such as the baseline conditions for the CHAMP reactor described in Chapter 4, is marked by **x** on the set of curves. At a temperature of 250 °C, the diffusion timescale is 1.0 second, the reaction timescale is 1.3 seconds, and the permeation timescale is 1.4 seconds. The timescale for operation of a cycle then is dictated by permeation, which is the longest. However, at this operating point, all the timescales are fairly well matched implying that no one process is exclusively rate limiting. For example, even though diffusion has the shortest characteristic time, it is by no means negligible. Diffusion acts to slow the reactions and permeation—in addition to delaying the start of the permeation process.

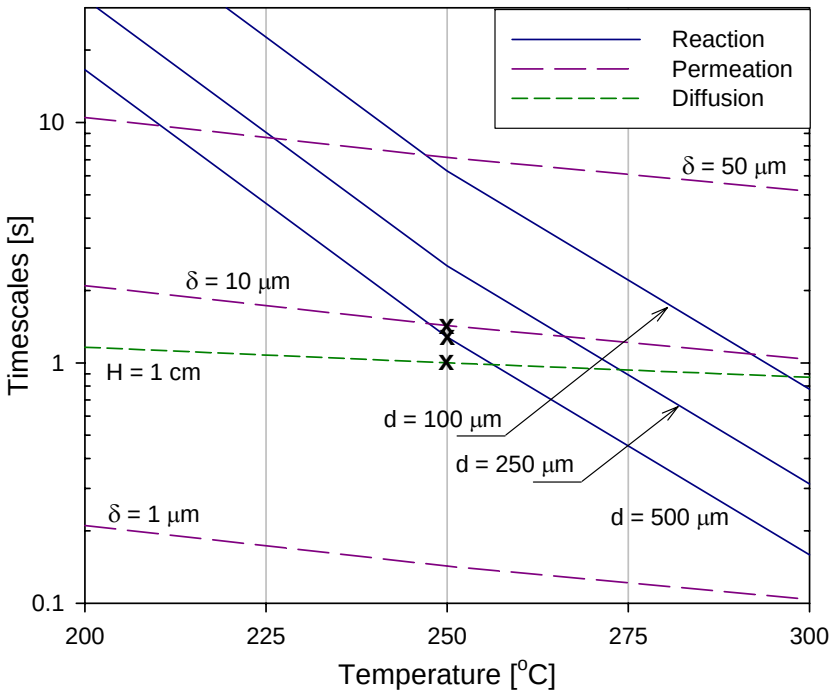

Figure 5.7 Timescales for reaction (solid lines), permeation (long dash), and diffusion (short dash) versus temperature (H = 1 cm).

The reaction timescale and permeation timescale, as they are currently defined, depend linearly on H, the size of the reactor. For example, a doubling of H causes the

reaction time to double because there is twice as much fuel to be consumed. (The ratio of *H* to *d*, or the turnover ratio, is the true scaling of the intrinsic reaction timescale, but it is not appropriate for scaling the intrinsic permeation or diffusion timescales.) In similar fashion, a doubling of H causes the permeation timescale to double because there is twice as much hydrogen to be permeated. This dependence on *H* can be removed by normalizing the timescales by *H*.

Timescale divided by *H*, results in a parameter with units of [time/length]. Taking the diffusion timescale and dividing it by *H*, leaves H/D_{AB}. This is none other than the inverse of the mass transfer coefficient, also known as the mass transfer *resistance*. Thus, normalizing all timescales by *H* in this manner allows us to view the reaction, diffusion, and permeation processes each as respective resistances to the ultimate goal of hydrogen output. It also allows us to clearly map the resistances for a wide range of parameters, *d*, *H*, and δ, versus temperature, as seen in Figure 5.8.

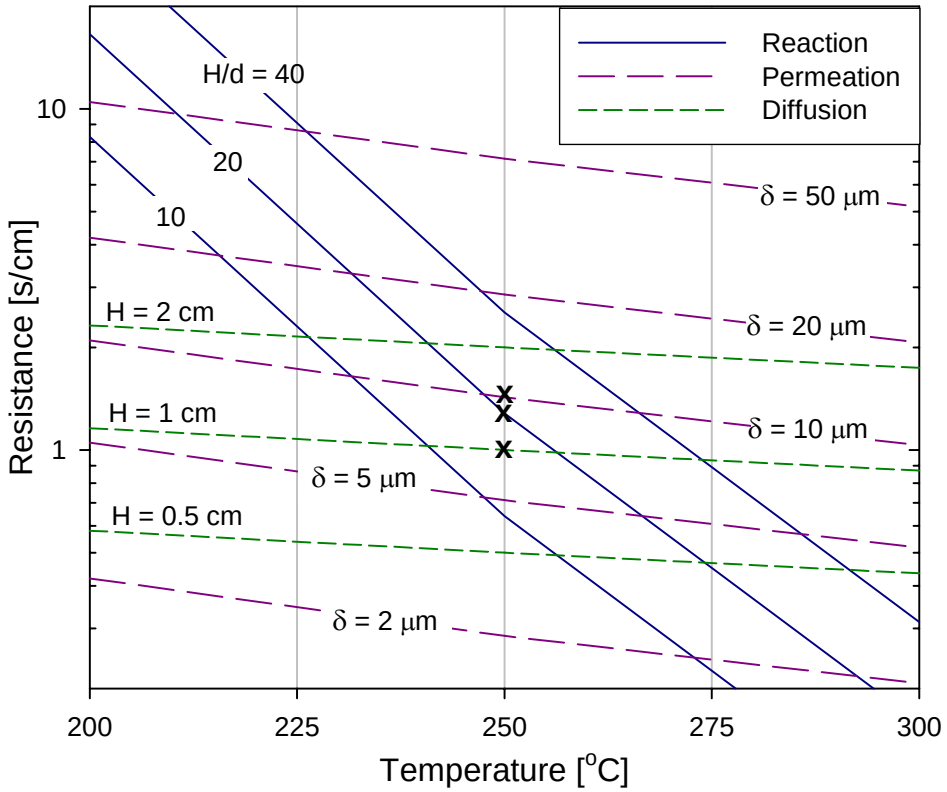

Figure 5.8 Timescale normalized by reactor size, *H*, is an equivalent "resistance" for the reaction, diffusion, and permeation processes plotted here as a function of temperature.

5.3.2 Optimization of reactor design

In the baseline case, located by the markers on Figure 5.8, the relevant process timescales (or resistances) are similar in magnitude. Figure 5.9 shows the rate of consumption of methanol, and the rate of permeation of hydrogen (output) with and without the effects of diffusion limitations. Because of the balance in timescales, the real reactor's performance can be significantly improved by 1) making the membrane thinner or providing a lower partial pressure of hydrogen on the permeate side, 2) providing more catalyst per volume of reactor, or 3) reducing the mass transfer resistance by decreasing the reactor size, *H*.

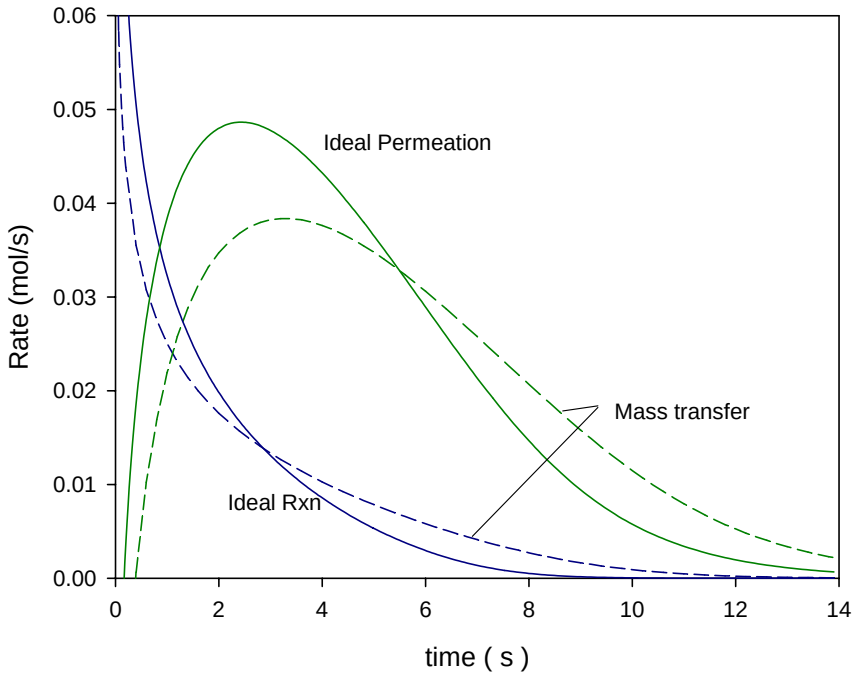

Figure 5.9 Reaction rate and permeation rate for the ideal case (solid lines) and with consideration of mass transfer effects (dashed lines).

In contrast, at an operating temperature of 200 °C, the reactor is clearly reaction limited with permeation and diffusion occurring at a significantly faster timescale. Investing in an ultra-thin membrane here, for example, would yield only a negligible

improvement in the reactor's performance. On the other hand, at 300 °C, the permeation and diffusion processes are rate limiting, with reactions being much faster. Therefore, shrinking the reactor size, H, or the thickness of the membrane, δ, translates into immediate gains in performance.

With these general qualitative trends in mind, a detailed analysis of the reactor performance as each design parameter is varied provides the quantitative information necessary to build a reactor that will meet the user-specified performance criteria. These criteria are assumed to be the cycle-averaged hydrogen yield rate, and the hydrogen yield efficiency as discussed previously. The cycle-averaged hydrogen yield rate serves as a proxy for the power output of the reactor because the quantity of hydrogen being sent to the power plant (e.g. fuel cell) is directly proportional to power output. The hydrogen yield efficiency is the quantity of hydrogen that has permeated the membrane, relative to three times the initial quantity of methanol in the reactor. Because the hydrogen permeation always lags the reactions, the extent of methanol conversion almost always exceeds 99% by the time the desired hydrogen yield has been reached. Therefore, it is unnecessary to include methanol conversion in the discussion.

For the baseline model parameters, the efficiency and cycle-averaged rate of hydrogen production are shown on the left and right vertical axes, respectively, of Figure 5.10. These values are plotted versus residence time scaled by reactor size, *H*. This parameter is proportional to the weight of catalyst to fuel ratio (W/F) that was described earlier. Here, the thickness of the catalyst layer, *d*, is held constant at 500 μm, the maximum value at which it is safe to neglect diffusion limitations within the catalyst [61]. The efficiency and power curves are given for three different reactor sizes, 0.5, 1.0,

and 2.0 cm. In the ideal reactor model, these three curves would have collapsed on each other when plotted versus time/*H*. However, the effects of mass diffusion in the bulk of the reaction chamber are clearly seen here. As the reactor size becomes smaller, diffusion resistance decreases and the power output and efficiency both increase approaching ideal performance.

On the other hand, the same curves are much closer together in Figure 5.11, where the temperature has been decreased from 250 to 200 °C. Here, the reaction is the rate limiting step and diffusion is relatively insignificant. However, because of the much slower reaction rate, the power output at 200 °C is approximately one-fourth of that at 250 °C. In both figures, a trade-off is seen between power and efficiency. For most applications of interest, the efficiency is required to be as high as practically possible. The maximum possible efficiency is governed by the low side partial pressure of hydrogen and the formation of CO, whose rate of production via the decomposition reaction increases faster than the steam reforming reaction rate as temperature rises. One possible procedure for designing a system is to specify a level of efficiency that must be reached and then seek to maximize the power output.

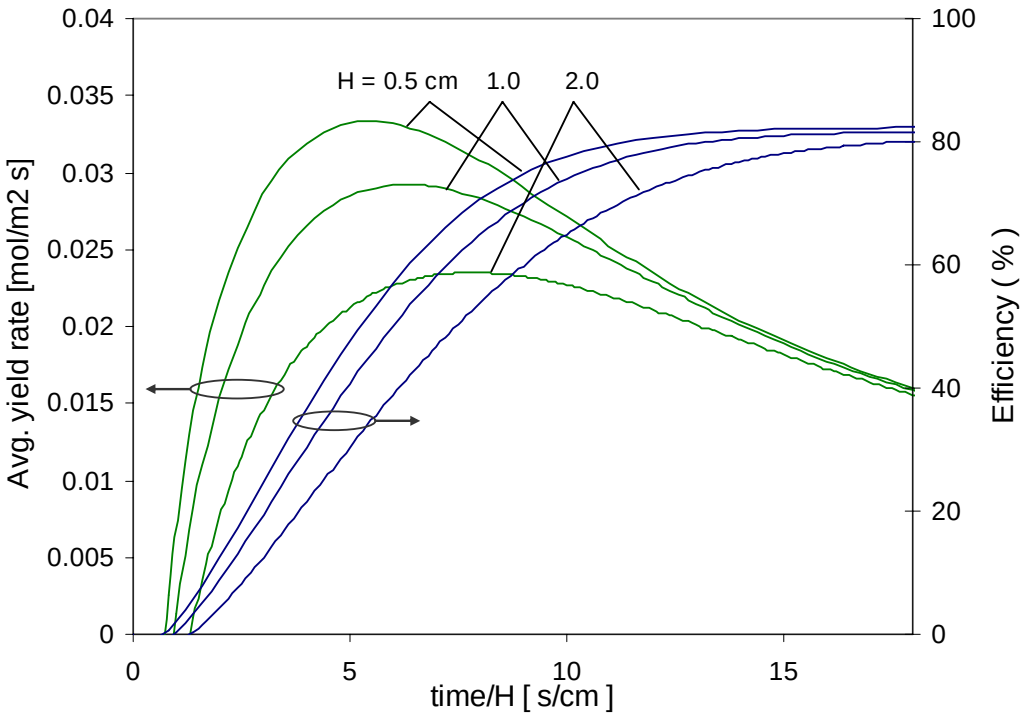

Figure 5.10 Efficiency and average hydrogen yield rate (power) for the baseline CHAMP reactor of various size, *H*, operating at 250 °C.

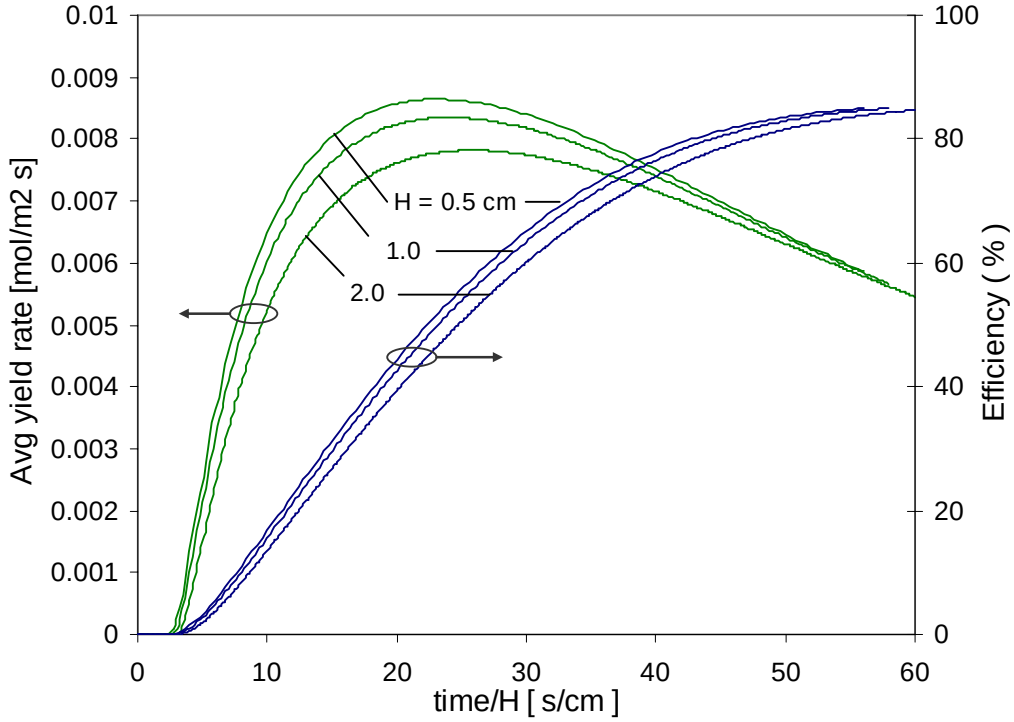

Figure 5.11 Efficiency and power output versus scaled residence time for the baseline CHAMP reactor with various reactor size, *H*, and an operating temperature of 200 °C.

In Figure 5.12, the efficiency criteria which must be reached (at which point the cycle is terminated) is fixed at 80%. The cycle-averaged hydrogen output once 80% efficiency is achieved is shown at various operating temperatures (200, 225, 250, 300 °C) as the membrane thickness is varied from 1 to 100 μm. Several noteworthy features are immediately apparent. Reducing the membrane thickness below approximately 5 μm provides a diminishing return on improved power output. At low temperatures, this is a result of operation in the reaction-limited regime and at high temperatures, a result of diffusion limitations. With very thick membranes (> 20 μm) power decreases with a slope of $1/\delta$ as expected in a permeation-limited regime. Also, increasing the temperature from 250 to 300 °C has a weak effect on power output because of entering either a diffusion-limited (thin membrane) or permeation-limited (thick membrane) regime—both processes have relatively weak temperature dependence. The magnitude of the membrane permeability's temperature dependence can be deduced from the trends on the far right side of the figure, where the reactor is exclusively permeation-limited.

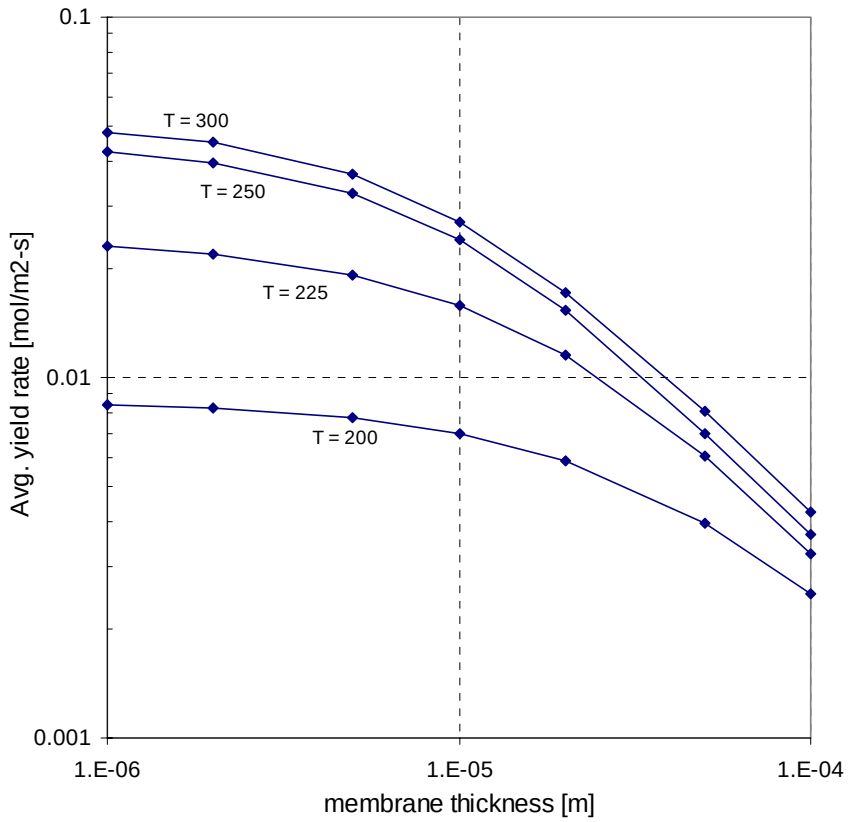

Figure 5.12 Average power output versus membrane thickness for various operating temperatures. The efficiency is fixed at 80%, the reactor size, *H*, is 1 cm, and the low side hydrogen partial pressure is 0.2 atm.

The average cycle power and yield efficiency are also affected by the low-side hydrogen partial pressure which establishes the set point for the driving force for permeation of hydrogen through the membrane and determines the upper limit of efficiency. In Figure 5.13 efficiency versus average hydrogen yield (power) is shown for low side partial pressures of 5, 10, 20, 30, and 50% of one atmosphere. As the low side partial pressure decreases, power output increases and the upper limit of efficiency increases. Also shown are lines of constant cycle (residence) time. Because of back permeation very early in the cycle, the average yield and efficiency are both initially negative. This is not a regime for practical operation and is excluded from the figure, which only shows positive values. The best regime for operation is above the dashed line

indicated on the figure. Below this line, both the power and efficiency can be increased by holding a longer cycle. Therefore, such a short cycle time is wasteful and unjustified. Eventually, power reaches a maximum (relative to efficiency), and beyond that point, longer cycle times allow higher efficiency by sacrificing the cycle-averaged power output. In the extreme limit of infinite cycle time, the maximum theoretical efficiency would be achieved and the cycle averaged power would go to zero. It is up to the system designer to determine the mix of efficiency and power that is most appropriate for a particular application. Once a design is chosen, the optimal parameters for operation must be specified.

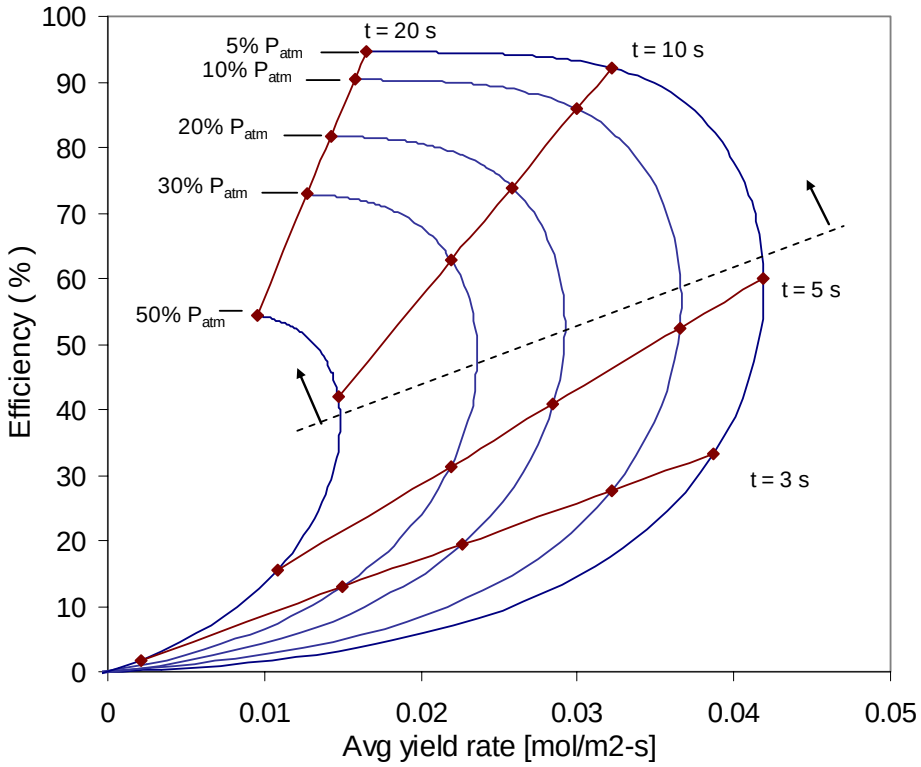

Figure 5.13 Efficiency versus cycle-averaged hydrogen output for the baseline CHAMP reactor for various values of low side hydrogen partial pressure. The lines of constant cycle time (residence time) are also shown.

5.3.3 Optimal reactor operation

The CHAMP reactor being considered here is operated by filling the reaction chamber with fuel, waiting for the reactions and permeation to proceed to completion, and then pushing the contents of the reaction chamber out through the exhaust valve in preparation for the next cycle. Additionally, the reaction chamber volume could be compressed during the waiting period to enhance the yield above that of the fixed volume case. Therefore, the operating parameters are 1) *H*, the distance that the piston is initially drawn back during the intake stroke, 2) residence time, or time that the mixture remains in the chamber, 3) decision to operate in fixed volume or variable volume mode, and 4) if in variable volume mode, what transient profile of piston motion to employ and the modified residence time that corresponds to the desired efficiency and cycle power.

First, consider the case of fixed volume operation. In Figures 5.14 and 5.15 the reactor efficiency and average power output is mapped for operating temperatures of 225 and 250 °C and various initial piston displacements, *H*, of 0.25, 0.5, 1.0, 1.5, and 2.0 cm. Once a reactor size is chosen, the residence time corresponding to a particular combination of power and efficiency can be read from the map. The residence time, *t*, is scaled by reactor size, *H*, and is given in units of [s/cm]. Because of mass diffusion in the reaction chamber, the smaller reactor size always gives better performance. However, moving along a line of constant t/H implies an increasing frequency of cycles, which always brings additional overhead cost and system losses (e.g. friction).

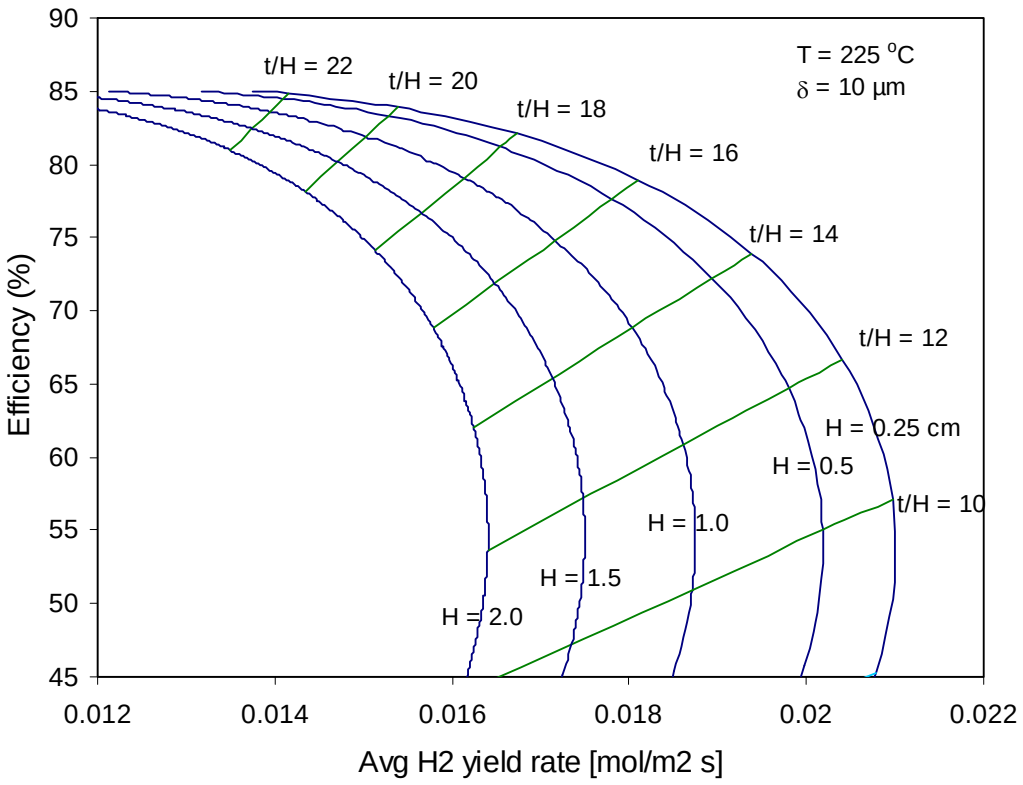

Figure 5.14 Efficiency versus average power output for the baseline CHAMP reactor operated at 225 °C and with various initial displacement, *H*. Lines of constant residence time, *t*, scaled by *H* [s/cm] are indicated.

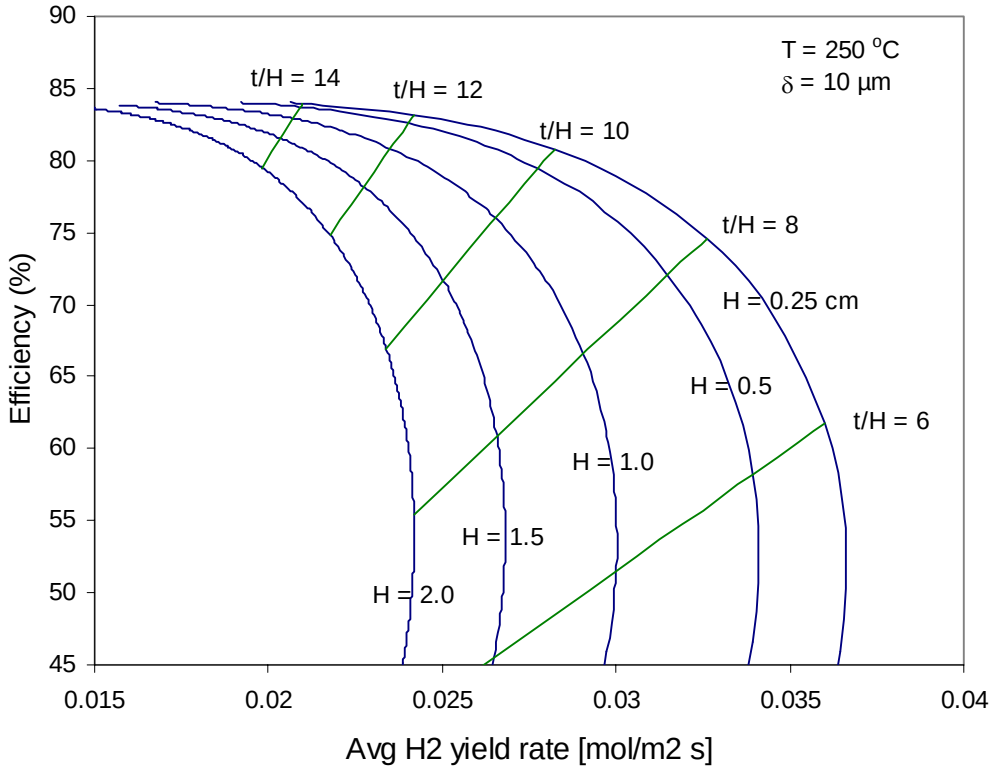

Figure 5.15 Efficiency versus average power output for the baseline CHAMP reactor operated at 250 °C and with various initial displacement, *H*. Lines of constant residence time scaled by H [s/cm] are indicated.

The cycle-averaged power output given in the figures is for a single cycle, taking no account for the time required to fill the reactor or discharge it. The quasi-steady output averaged over multiple cycles will be somewhat lower due to this "dead" time between cycles. For example, the transient profiles of instantaneous hydrogen yield rate for several cycles are shown in Figure 5.16 for initial reactor sizes of 0.5 and 1.0 cm. The cycles are terminated when the efficiency reaches 80%. The dead time between cycles has been arbitrarily set at 1 second for the purpose of this example. The 0.5 cm size reactor has a single cycle-averaged hydrogen yield of 0.0246 mol/m^2 s, and the 1.0 cm reactor yield is 14% lower, or 0.0211 mol/m^2 s. However, when including the "dead" time in calculations, the quasi-steady output of the reactors over multiple cycles is 0.021

and 0.0196 mol/m^2 s for the 0.5 and 1.0 cm reactors, respectively. This is a difference of only 6.7%. The penalty of having to run twice as many cycles to achieve this minimal improvement in power output may or may not be justified.

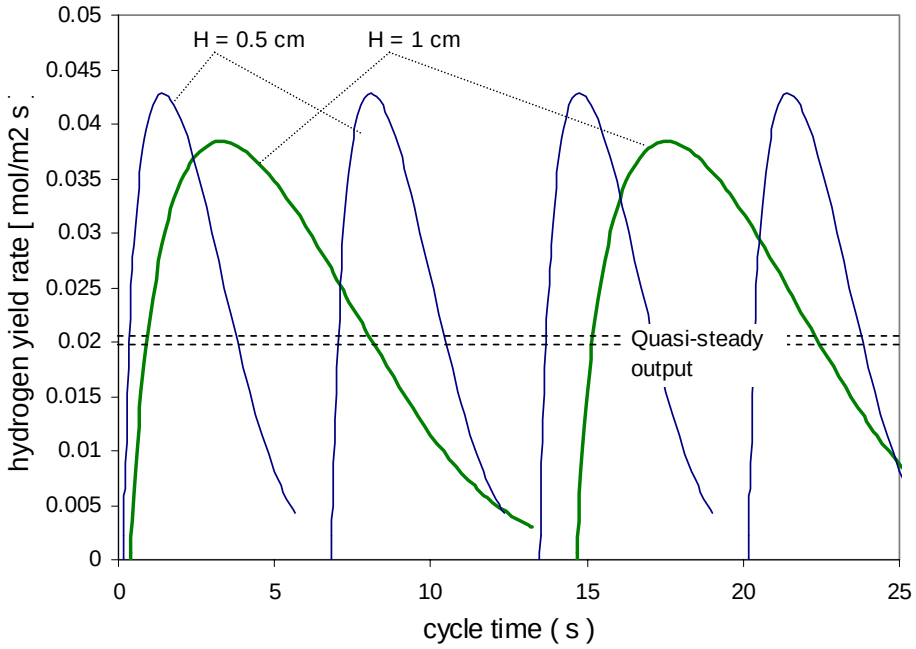

Figure 6.16 Instantaneous rate of hydrogen yield across multiple cycles for the baseline CHAMP reactor with initial displacement, *H*, of 0.5 and 1.0 cm. A dead time of 1 second has been added on to the end of each cycle for discharge and refilling.

In addition to the fixed-volume mode of operation just described, the CHAMP reactor may also be operated in variable-volume mode. Compressing the reactor with the piston may be desirable if an immediate boost in hydrogen output is required to satisfy a transient load. However, piston motion robs the power output if it is not implemented properly, and compression could increases the total pressure in the reactor, putting a mechanical strain on the delicate membrane, the piston seals, tubing connections, and valving.

The key to managing the total pressure in the reactor is to match the timescale for piston motion, or velocity, to the rate of hydrogen permeation through the membrane. If

the piston motion is faster than hydrogen can permeate, then the pressure rises rapidly. If the piston motion is too slow, then it is ineffectual in driving additional hydrogen through the membrane beyond what would normally occur and instead becomes a parasitic load on the power output of the system. When the rate of hydrogen permeation is precisely matched by the rate of compression, then the pressure remains constant.

As already mentioned, the pressure in the reactor initially rises (without active compression) due to the increasing number of moles of products created by the reactions. As the rate of loss of hydrogen due to permeation matches the rate of production via reactions, the pressure reaches a maximum (see Figure 5.6). The system must be designed to withstand this temporary maximum pressure. Therefore, once the maximum is reached, the piston could be driven forward to maintain the pressure at an elevated constant value, which, in turn, maximizes the rate of hydrogen permeation (under the constraint of maximum total operating pressure).

Figure 5.17 illustrates the pressure profiles and corresponding piston displacements for both constant volume and constant pressure operation. The trajectory of piston motion for the constant-pressure operation is not known *a-priori,* but is adjusted throughout the cycle as needed to keep the pressure at its maximum value. The enhancement in performance is seen in Figure 5.18 which shows yield efficiency and net power output versus time. Operating the reactor at its maximum allowable pressure enhances both power output and efficiency beyond the fixed-volume case. The net power output was defined previously and takes into account the power required for compression of the reactor volume. The gain, or ratio of piston power input to marginal reactor power increase is of similar magnitude to that shown in Figure 4.14.

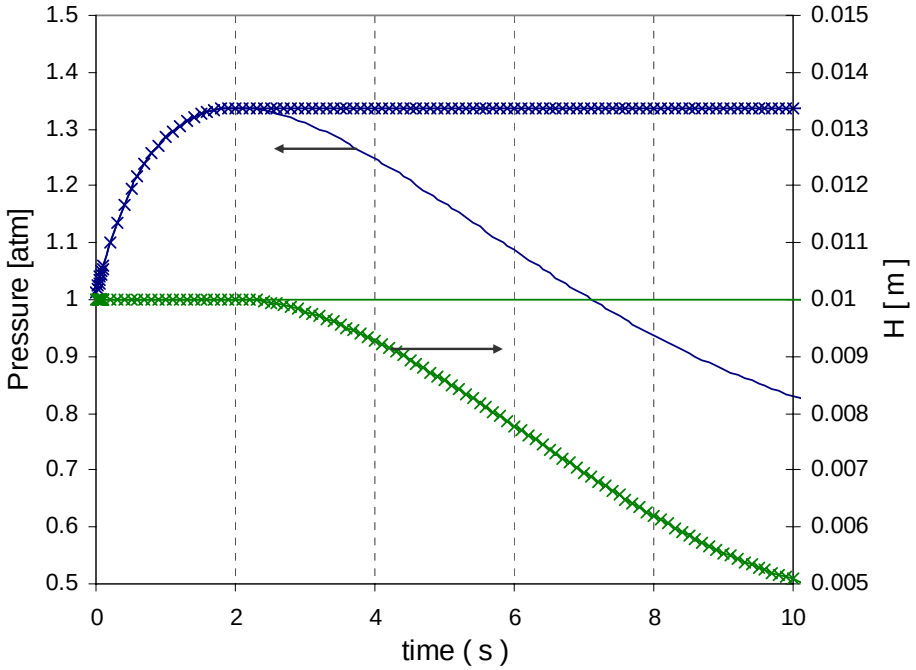

Figure 5.17 Transient profiles of total pressure and size of reactor, *H*, for the baseline CHAMP reactor operated in constant-volume (solid lines) and constant-pressure (lines marked with x's) mode.

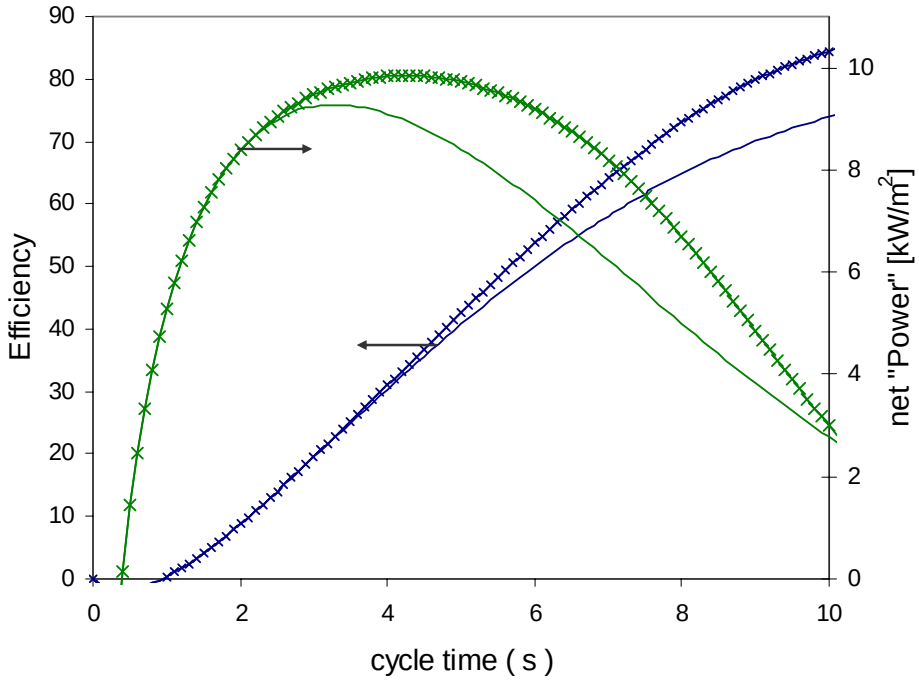

Figure 5.18 Efficiency and net power output of the two cases illustrated in Figure 6.17. In constant-pressure mode (lines marked with x), both power output and efficiency are higher than in the fixed volume mode (solid lines).

Countless other trajectories of piston motion are possible, but those that do not exceed the maximum allowable total pressure are bounded on one side by the zero velocity (fixed-volume) case, and on the other side by the constant-pressure case just described. If compression were to begin before the pressure peaks, then the magnitude of the pressure peak is required to increase beyond what is allowed. On the other hand constant pressure operation at a lower total pressure (after the pressure peak as illustrated in Figure 5.19) is allowed but does not provide the magnitude of performance enhancement that is achieved by operating at the highest allowable pressure (see Figure 5.20). The constraint of constant, maximum total pressure makes the optimization of the piston trajectory somewhat intuitive. Other constraints, such as required hydrogen yield efficiency or power output, and a relaxed pressure constraint can lead to entirely different transient profiles of piston motion.

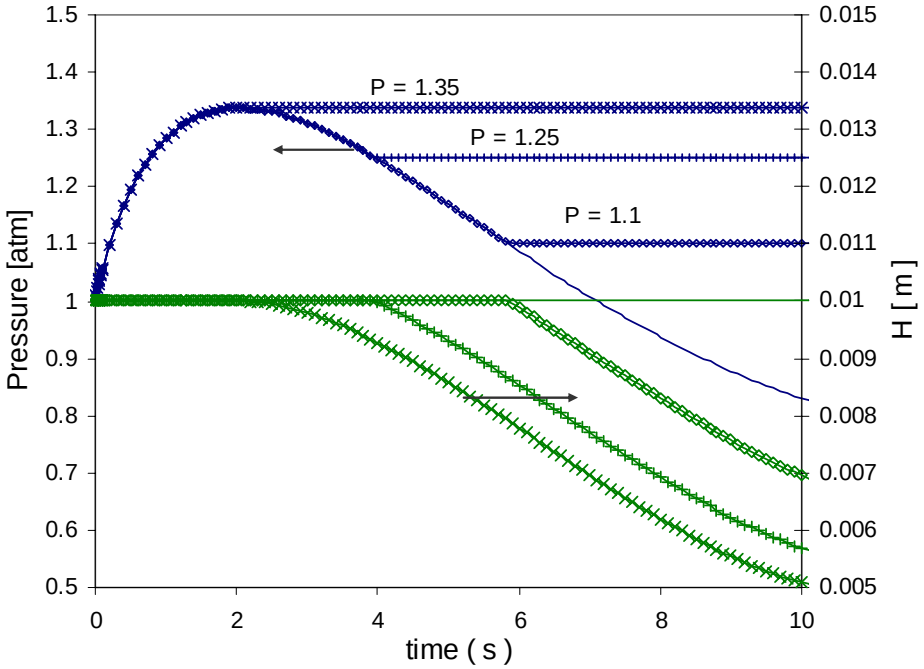

Figure 5.19 Constant pressure profiles with corresponding piston trajectory.

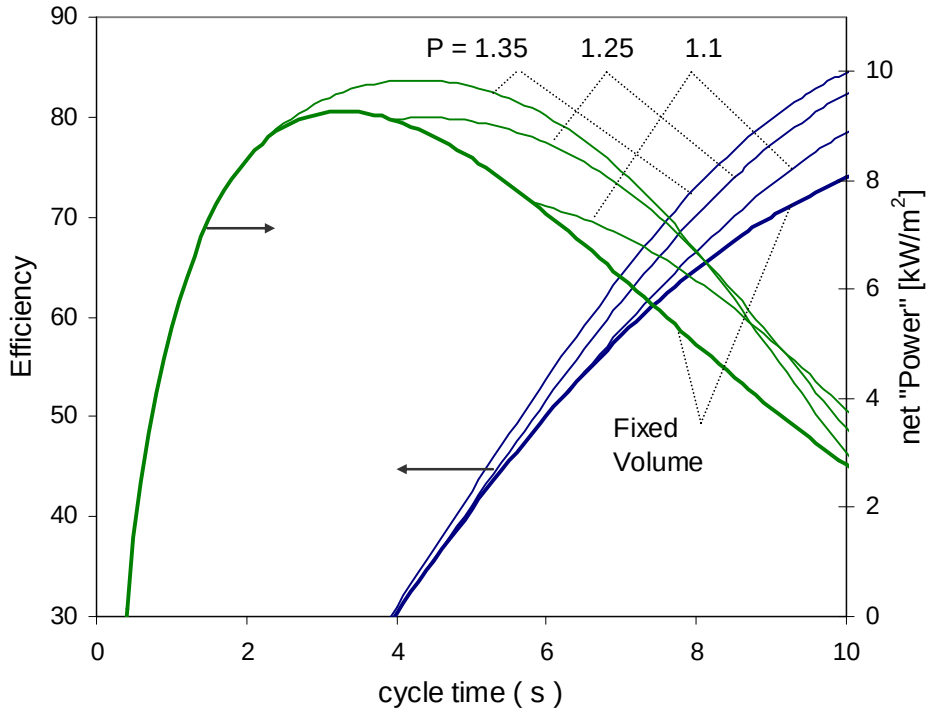

Figure 5.20 Efficiency and net reactor power output for the piston/pressure profiles given in Figure 6.19

The design map in Figure 5.21 relates the cycle-averaged net power output, and efficiency, to initial reactor size and cycle time for the constant pressure mode of operation (in similar fashion to Figures 5.14 and 5.15 for constant-volume operation). Also given is the maximum pressure that the reactor will see assuming an initial pressure of 1 atm. This mapping provides the information necessary to operate the reactor in a constant-pressure mode of operation, while allowing the user to choose the balance of power versus efficiency that is appropriate for the application in mind.

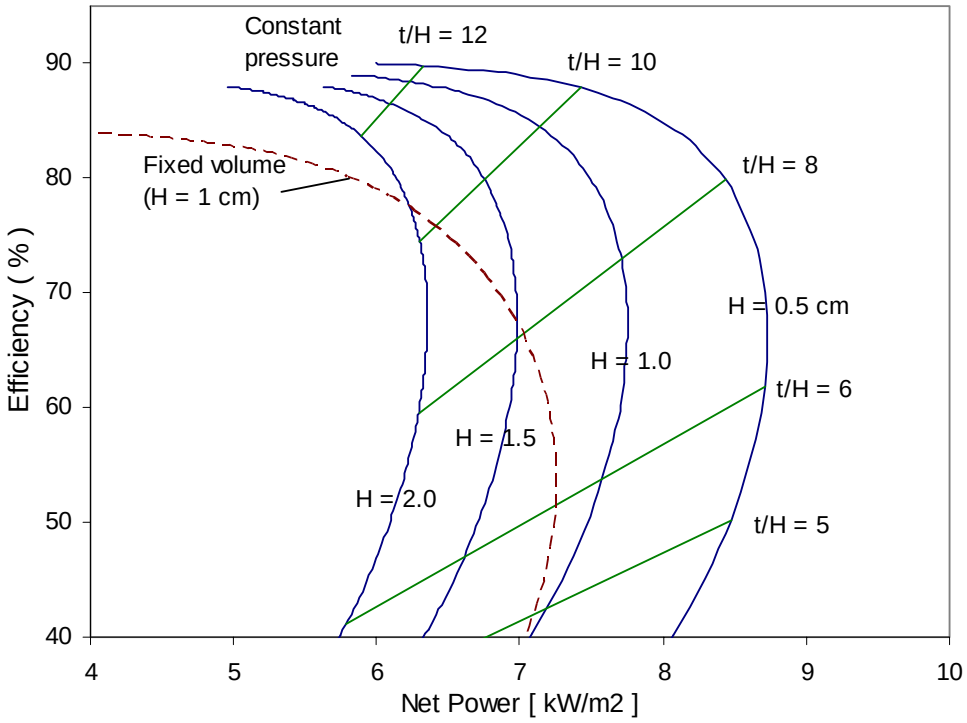

Figure 5.21 Efficiency versus power output for the baseline CHAMP reactor operated in a constant-pressure mode and various initial size, H. The initial pressure for each reactor was 1 atm, and the peak operating pressure was approximately 1.35 atm.

5.4 Conclusions

The one-dimensional, coupled, mass transport, reaction kinetics, permeation, and volume compression model presented here allows a study of the optimal design and operation of a realistic batch reactor. The transitions between reaction limited, permeation limited, and diffusion limited regimes have been mapped out and provide insight into optimization of the design parameters including temperature, reactor size, membrane thickness, and low-side hydrogen partial pressure. Once a design is chosen, the operating parameters must be selected: initial displacement of the piston, residence time, and transient profile of piston motion (if any).

In fixed-volume mode of operation, the residence time is precisely controlled to provide the desired trade-off between efficiency and power output. Recognizing that the

reactor can operate at an elevated constant pressure—maintained by a pressure-following piston trajectory—opens up otherwise inaccessible regions of the efficiency-power parameter space. This ability to dynamically control the reactor volume, mid-cycle, to achieve the desired blend of efficiency and power is unique to the CHAMP-class of reactors.

To complement this theoretical analysis, experimental characterization of a test rig reactor is described next in Chapter 6.

CHAPTER 6

BENCH SCALE REACTOR DEVELOPMENT & CHARACTERIZATION

Complimentary to the conceptual and theoretical development of the CHAMP reactor technology, a bench-scale test reactor has been built and tested. The primary purpose of this experimental work is to 1) demonstrate that the concept of a variable volume batch reactor is sufficiently practical and feasible that it can be built and operated, and 2) validate the numerical model predictions of fuel conversion and hydrogen yield via a side-by-side comparison to experimental data. To measure the rate of conversion of fuel to hydrogen and verify that the expected reactions are taking place, a reactor without a hydrogen permeable membrane was built and tested with periodic sampling of the reacting mixture. A second test reactor—with a hydrogen permeable membrane incorporated—was designed to allow continuous measurement of the hydrogen yield, or permeation rate, throughout the operation of a cycle. In both cases, measurements were taken with the reactors operating in the constant volume mode and with mid-cycle volume compression.

6.1 Experimental setup #1

Figure 6.1 shows a schematic diagram of the first reactor and experimental setup. The piston and cylinder (7.5 cm internal diameter) were machined from aluminum alloy 6061 and supplied with Viton O-rings (Parker Hannifin, AS568A dash number 334) on the piston to provide a good seal at elevated temperatures. See Appendix C for detailed drawings of the major reactor components. The catalyst is commercially available from BASF (F3-01, 1.5*mm* dia. *x* 1.5*mm* pellets) and composed of copper and zinc oxides on a

porous aluminum oxide substrate ($CuZnAl_3O_2$). A single layer of pellets was held in place on the face of the piston by a copper mesh. The catalyst was reduced in a mixture of 50/50 hydrogen and helium over the catalyst at 180 °C for 1 hour per the manufacturer's directions. The reactor was heated by four Chromalox cartridge heaters (3/8 inch dia. by 1.5 inch length, rated at 120V and 250W) embedded inside the piston. The power output of the heaters was controlled by a Tenma variable auto transformer with output of 0-130 V and maximum current of 10 A. The temperature of the catalyst was monitored by thermocouples (Omega Technologies, K-type) embedded 1 mm below the catalyst in the face of the piston. The thermocouples were connected to an Agilent 34970A data acquisition/switch unit which provided a continuous temperature readout (±0.05 °C). Prior to running experiments, the entire fixture was brought up to the desired steady-state temperature and the heater controller voltage was set to maintain this temperature while experiments were being run. The operating temperature was assumed to be that measured by the thermocouple nearest the edge of the piston. The temperature recorded by the thermocouple at the center of the piston was typically 5 °C greater than that near the edge, but these values never drifted off by more than 3 °C over the course of operating 15-20 cycles.

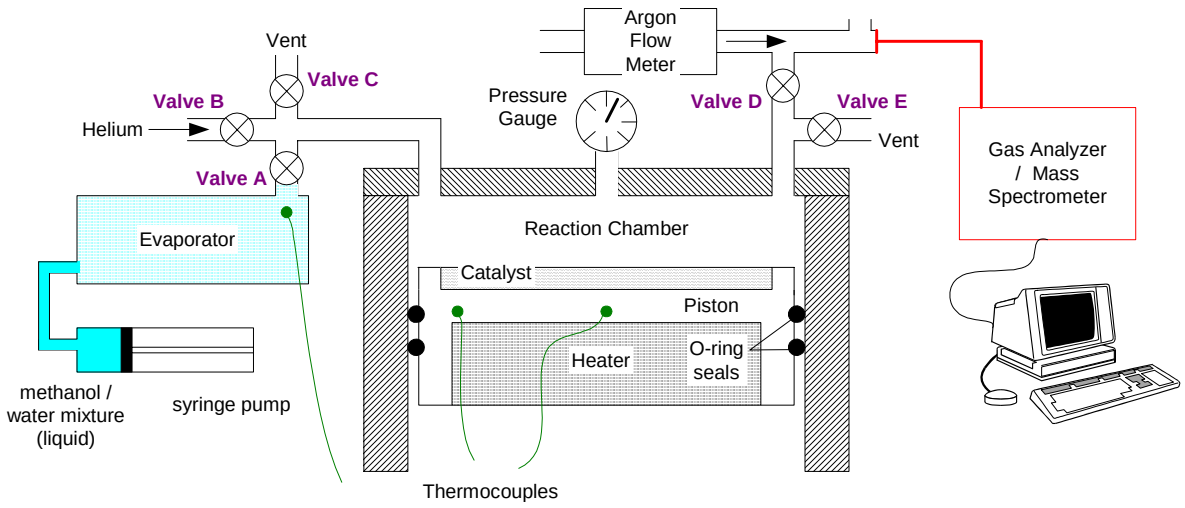

Figure 6.1 Schematic diagram of the experimental setup for testing the prototype reactor.

Experiments were performed to determine the extent of methanol conversion for various cycle time. A syringe pump (World Precision Instruments, SPI100i, with 0.05 ml/hr flow rate resolution) was used to pump a precise volume of methanol/water liquid mixture through an evaporator (constructed out of 1/8 inch stainless steel tube wrapped with a flexible Ni-chrome heater) and into the reaction chamber. The temperature of the evaporator was maintained at the same (±3 °C) temperature as the catalyst, by setting the voltage on the Tenma heater controller The content of the reactor was sampled at various times (measured by a wristwatch/stopwatch with 0.01 sec resolution) by sending the mixture out through an exhaust valve and sweeping it with argon (1100 ± 110 sccm, as measured by a Cole-Parmer mass flow meter, EW-32464-40) to a mass spectrometer (Hiden Analytical Quadrapole HPR-20) through a heated capillary tube (to keep water and methanol vapor from condensing). The baseline reference pressure for background argon measurements was 3e-6 torr. The mass spectrometer was calibrated to sample every 0.5 seconds with accuracy to 0.05 % of the argon sweep gas reference partial pressure. To achieve higher accuracy of partial pressure measurements would have

required an increase in the sampling time by an order of magnitude (to 5 seconds) which was not practical for capturing rapid changes in mixture composition required in the experiments.

The procedure for performing an experimental run (fixed-volume, to establish the baseline performance) was as follows:

1. The entire reactor (reaction chamber + pipes and valves) is purged with Helium gas, the piston is in the fully retracted position ($H = 2 \pm 0.05\ cm$), and all valves are closed.
2. Valves A and E (see Figure 6.1) are opened, and the syringe pump is turned on to deliver a set volume of 0.1 ml of fuel mixture at a rate of 240 ±0.05 ml/hr to displace the Helium and fill the reaction chamber.
3. When filling is complete, valves A and E are closed; the reactor is left undisturbed for a prescribed amount of time ranging from 10 to 30 seconds.
4. The valve D is opened and the piston is pushed forward rapidly (requires ~2 sec ±0.5 sec), sending the contents of the reactor to be swept to the mass spectrometer to determine the partial pressures of methanol, water vapor, hydrogen, carbon dioxide, and carbon monoxide relative to the argon background pressure.
5. The reactor is prepared for another trial run by flushing it with helium, and the experiment is repeated for multiple wait times (given in Step 3).

Figure 6.2 shows a sample readout of mass spectrometer measurements of partial pressure for each species (hydrogen, methanol, carbon dioxide, and carbon monoxide) relative to the background argon partial pressure. Because the flow rate of argon was metered, the flow rate of each species being carried to the gas analyzer in Step 4 could be

calculated by multiplying the flow rate of argon and the ratio of partial pressure of species, *i*, to partial pressure of argon.

$$\dot{n}_i = \frac{P_i}{P_{Ar}} \dot{n}_{Ar} \tag{6.1}$$

Then, by integrating the flow rate of species, *i*, the total number of moles of that species is known. The methanol conversion was calculated as,

$$\chi = 1 - 3n_{MeOH} \Big/ \left(3n_{MeOH} + n_{H2}\right) \tag{6.2}$$

where n_{MeOH} is the number of moles of methanol and n_{H2} is the number of moles of hydrogen. The number of moles of these species for given cycle times is summarized in Table 6.1. The uncertainty in the number of moles is calculated from the uncertainty in the flow rate of the sweep gas (10%) and the uncertainty in the partial pressure readings (0.05% of partial pressure of argon),

$$e_{n,i} = \sqrt{\left[\left(\frac{\partial n_i}{\partial P_i}\right) e_{P,i}\right]^2 + \left[\left(\frac{\partial n_i}{\partial P_{Ar}}\right) e_{P,Ar}\right]^2 + \left[\left(\frac{\partial n_i}{\partial n_{Ar}}\right) e_{n,Ar}\right]^2} \tag{6.3}$$

The uncertainty in the calculated methanol conversion is found from the following error-propagation expression:

$$e_\chi = \sqrt{\left[\left(\frac{\partial \chi}{\partial n_{MeOH}}\right) e_{MeOH}\right]^2 + \left[\left(\frac{\partial \chi}{\partial n_{H2}}\right) e_{H2}\right]^2} \tag{6.4}$$

These values are also summarized in Table 6.1.

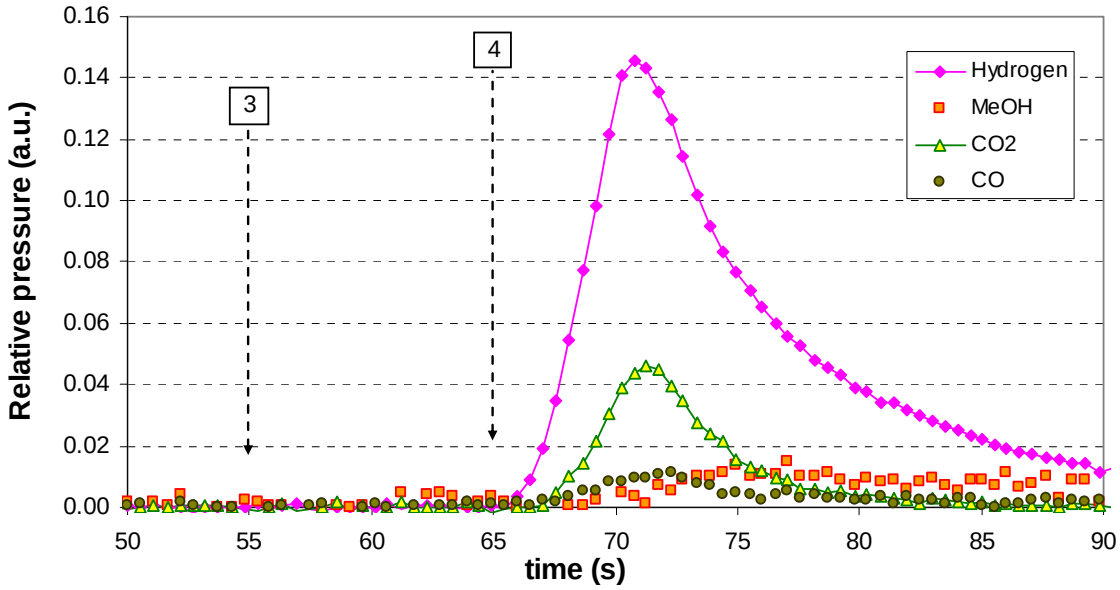

Figure 6.2 Sample plot of relative partial pressure readings for hydrogen, methanol, carbon dioxide, and carbon monoxide throughout completion of a cycle. After filling the reaction chamber with fuel and closing the valves (3), the reactor sits undisturbed for 10 seconds and then the exhaust valve is opened (4) and the piston pushes out the contents of the reaction chamber for analysis. The ratio of hydrogen to methanol indicates the extent of fuel conversion, and the ratio of hydrogen to carbon dioxide indicates that the dominant reaction mechanism is steam reforming.

Table 6.1 Experimental data for fixed-volume operation

cycle time (s) ± 1 s	CO_2 (mol/mol) ± 12%	H_2 (mol/mol) ± 11%	CH_3OH (mol/mol) ± 0.0007 (mol/mol)	Conversion	Conversion Uncertainty
10	0.0085	0.0242	0.0051	60.4%	±7.8%
10	0.0118	0.0330	0.0083	55.9%	±5.8%
11	0.0113	0.0322	0.0078	56.9%	±5.9%
13	0.0118	0.0349	0.0051	69.0%	±5.9%
13	0.0108	0.0316	0.0043	70.8%	±6.5%
13	0.0101	0.0299	0.0034	73.9%	±6.9%
13	0.0111	0.0322	0.0056	65.1%	±6.2%
13	0.0090	0.0268	0.0035	71.5%	±7.5%
12	0.0106	0.0305	0.0046	68.6%	±6.6%
18	0.0118	0.0349	0.0018	86.4%	±6.0%
18	0.0125	0.0364	0.0031	79.7%	±5.8%
18	0.0139	0.0400	0.0036	78.4%	±5.3%
23	0.0148	0.0442	0.0032	82.2%	±4.8%
23	0.0152	0.0440	0.0029	83.6%	±4.8%
23	0.0138	0.0413	0.0026	84.1%	±5.1%
33	0.0157	0.0463	0.0007	95.4%	±4.5%
33	0.0146	0.0441	0.0004	97.2%	±4.8%

Figure 6.3 shows the results of conversion vs. time for the set of experiments with a fixed reactor volume (case A), or no piston motion. The solid line in the figure is the model prediction for these operating conditions. Generally good agreement is observed between the model predictions and the trend of experimental results. The expression given for methanol conversion assumes that steam reforming is the dominant reaction, which is valid at the low operating temperature used here (190 °C). (see Fig. 4.4 in Chapter 4 describing reaction kinetics as function of temperature.) This is also validated by the ratio of hydrogen to carbon dioxide (Table 6.1) and the low levels of CO (2-3%).

The spread in the data can be attributed to limitations in the ability to precisely control the initial conditions from one cycle to the next. That is, the rate of fuel mixture filling the chamber and the extent to which it displaced the helium affected 1) the initial composition of the mixture, 2) the initial turbulent mixing within the reactor, and 3) the quantity of residual fuel that was trapped in the tubing between the exhaust port and the sweep gas junction. These parameters are difficult to control and their uncertainties cannot be accurately quantified in the test reactor. Also, it was not practical to gather data at shorter times (and lower levels of conversion) because the process of filling the reaction chamber with fuel, and emptying the products required nearly 5 seconds. The model assumes that these processes occur instantaneously without disturbing the concentration profiles of reactants and products. While this assumption is reasonable for long cycle times, it becomes less valid as the cycle time becomes similar to the filling and discharge time. For the experiments reported here, the temperature of the reactor was maintained at 190 °*C* in order to slow down the reaction rate to be recordable. Notice

from Figure 5.5 that the conversion of methanol would be more than 90% after only a 10 second cycle time at a temperature of 250 °*C* in a similar reactor.

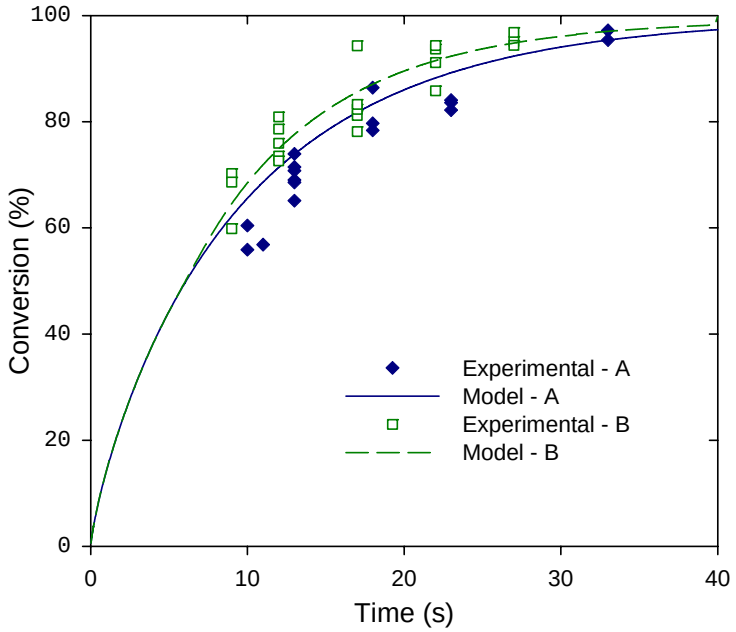

Figure 6.3 Experimental results and model predictions of methanol conversion for the case of a fixed reactor volume (A) and moving piston (B) with a reactor temperature of 190 ± 5 °C.

Under the operating conditions of these experiments, the reaction timescale and bulk gas diffusion timescales were of similar magnitude, implying that both processes play a role in determining the observed rate of conversion. As the fuel is consumed, the reaction rate slows down and maximum conversion is approached asymptotically as illustrated in Figure 6.3. To demonstrate the effects of a changing volume on fuel conversion, the experiments were repeated, this time moving the piston forward during the cycle in order to shorten the diffusion length and to maintain an elevated concentration of fuel. The procedure for experiments with piston motion was very similar to that listed above, with the following modification to Step 3:

3. When the filling process is complete, valves A and E are closed; the piston driving screw was moved forward at a rate of 1 turn per second for 2 seconds (which corresponds to a linear motion of 3.85mm/s, resulting in a total motion of 7.7 mm); the reactor is then left undisturbed for a prescribed amount of time ranging from 10 to 30 seconds.

The calculation of methanol conversion was the same as previously described [Eqs. (6.1) -(6.4)] and the data is reported in Table 6.2. The conversion results with piston motion (B) are plotted in Figure 6.3 along with the model simulation (dashed line) of the same operation. A clear shift in the data (vs. the fixed volume case (A)) towards higher conversion for any given time (after the piston is moved) indicates that the reaction rate is indeed being enhanced as expected.

Table 6.2 Experimental data for variable-volume operation

cycle time (s) ± 1 s	CO2 (mol/mol) ± 12%	H2 (mol/mol) ± 11%	CH3OH (mol/mol) ± 0.0007 (mol/mol)	Conversion	Conversion Uncertainty
10	0.0071	0.0202	0.0028	70.2%	±9.7%
10	0.0071	0.0199	0.0030	68.6%	±9.8%
10	0.0084	0.0232	0.0050	59.9%	±8.1%
12	0.0077	0.0221	0.0020	78.6%	±9.2%
12	0.0077	0.0227	0.0027	73.5%	±8.8%
12	0.0074	0.0211	0.0026	72.6%	±9.4%
12	0.0076	0.0222	0.0017	80.9%	±9.2%
12	0.0070	0.0207	0.0021	76.0%	±9.8%
17	0.0091	0.0262	0.0024	78.1%	±7.8%
17	0.0092	0.0269	0.0021	81.2%	±7.7%
17	0.0086	0.0245	0.0017	82.4%	±8.4%
17	0.0084	0.0246	0.0005	94.3%	±8.5%
17	0.0089	0.0256	0.0017	83.3%	±8.1%
22	0.0096	0.0285	0.0006	93.7%	±7.4%
22	0.0095	0.0281	0.0009	91.1%	±7.4%
22	0.0103	0.0300	0.0016	85.8%	±7.0%
22	0.0077	0.0224	0.0004	94.3%	±9.4%
27	0.0079	0.0233	0.0004	95.2%	±9.0%
27	0.0088	0.0258	0.0003	96.8%	±8.1%
27	0.0096	0.0287	0.0006	94.4%	±7.3%

Because the reactor was operated manually (opening and closing valves, running the syringe pump, moving the piston, etc.) the operating conditions were selected to force a long cycle time relative to event timing. Thus the experimental results reported here are not intended to demonstrate the ideal or optimal operation of the reactor, but rather to provide: 1) verification of the expected dominant reaction, 2) appropriateness of the coupled reaction kinetics and mass transfer models for predicting the reaction rate in the presence of bulk gas-phase diffusion limitations, and 3) the ability to operate the batch reactor in both fixed-volume and variable-volume modes.

6.2 Experimental setup #2

Experiments performed using the first reactor provided snapshots of the composition of the mixture inside the reactor as the methanol reacted with water vapor to form hydrogen and carbon dioxide. Of much more practical interest, however, is the rate of hydrogen output from a membrane-integrated reactor. Thus the reactor and experimental setup were modified to include an integrated, hydrogen selective, Palladium (Pd) membrane in direct contact with the reaction chamber.

The membrane was constructed of a commercially available [Birmingham Metal Company], 54 μm thick Pd foil and formed the cylinder cap or top of the reaction chamber as illustrated in Figure 6.4. A preheated, metered argon sweep gas was used to maintain a low partial pressure of hydrogen on the permeate side of the membrane and carry the separated hydrogen to the gas analyzer to measure the hydrogen permeation rate. Detailed drawings of the modified cylinder cap and sweep gas manifold are included in Appendix C. The fuel mixture was supplied through the same syringe pump, evaporator, and inlet valve as before. A discharge valve allowed the contents of the

reaction chamber to be sent to the argon sweep gas and carried to the mass spectrometer at the conclusion of the cycle. Unless stated otherwise, all equipment, hardware, and tools were the same as described previously with the same resolution of measurements.

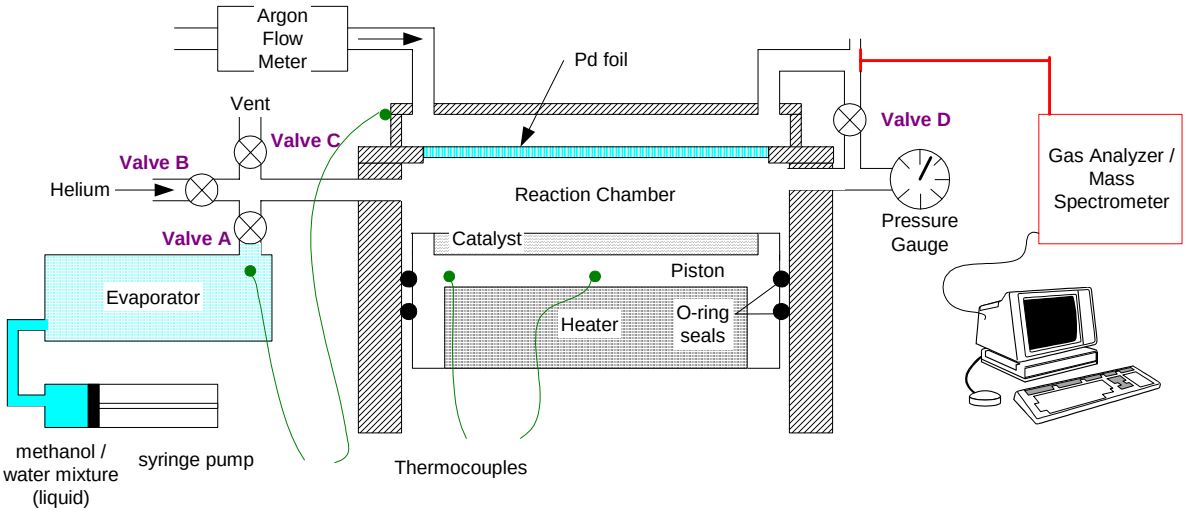

Figure 6.4 Schematic diagram of the experimental setup for testing the prototype membrane reactor

The procedure for performing an experimental run (without piston motion, to establish the baseline performance) was as follows:

1. The entire reactor (reaction chamber + pipes and valves) is purged with Helium gas, the piston is in the fully retracted position ($H = 2 \pm 0.05\ cm$), and all valves are closed. The argon sweep gas is flowing on the permeate side of the membrane.
2. Valves A and D (see Figure 6.4) are opened, and the syringe pump is turned on to deliver 0.1 ml of fuel mixture to displace the Helium and fill the reaction chamber.
3. When the filling process is complete, valve D and then valve A are closed; the reactor is left undisturbed for approximately 2 minutes while the mass

spectrometer records the partial pressures of argon, helium, hydrogen, and carbon dioxide (every 0.5 seconds). Pressure in the reactor is monitored and recorded every 5 to 10 seconds.

4. The valves B and D are opened, purging the reactor and sending the mixture to the mass spectrometer.
5. The reactor is prepared for another trial run, and the experiment is repeated several times to ensure reproducibility of results.

As seen in Figure 6.5, the readings of helium and carbon dioxide, relative to the sweep gas, were zero (within the resolution limit of the mass spectrometer) indicating that there were no leaks between the reaction chamber and the argon sweep gas. Thus, any hydrogen that was detected during step 3 must have permeated through the membrane. The flow rate (and uncertainty) of hydrogen is calculated as described previously.

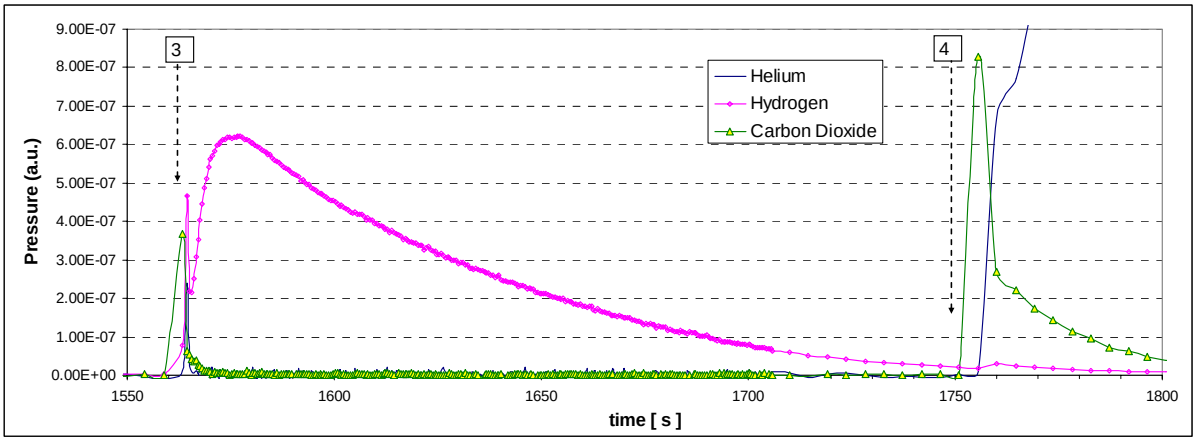

Figure 6.5 Sample plot of machine readings of partial pressure of helium, hydrogen, and carbon dioxide during the permeation phase (step 3) and exhaust phase (step 4) of a cycle. During step 3, He and CO_2 readings are zero within the resolution of the mass spectrometer, and the only species carried by the sweep gas is hydrogen. When the exhaust valve is opened (4), the contents of the reaction chamber are flushed out by the helium purge.

Figure 6.6 shows representative results for the reactor's hydrogen output (separated through the membrane) as measured by the gas analyzer during step 3. The reactor was operated at both 190 and 250 (± 5) °C, generating two distinct sets of curves. Most of the spread in the data can be attributed to limitations in the ability to precisely control the initial conditions from one cycle to the next. Pressure measurements (McDaniels Controls, 0-15 psi range with +/-0.25 psi resolution) indicated that the initial pressure was between (1.5 - 3.0) ± 0.25 psi above atmospheric pressure. This implies that not all of the helium was being displaced by the fuel mixture and remained in the reaction chamber during the cycle.

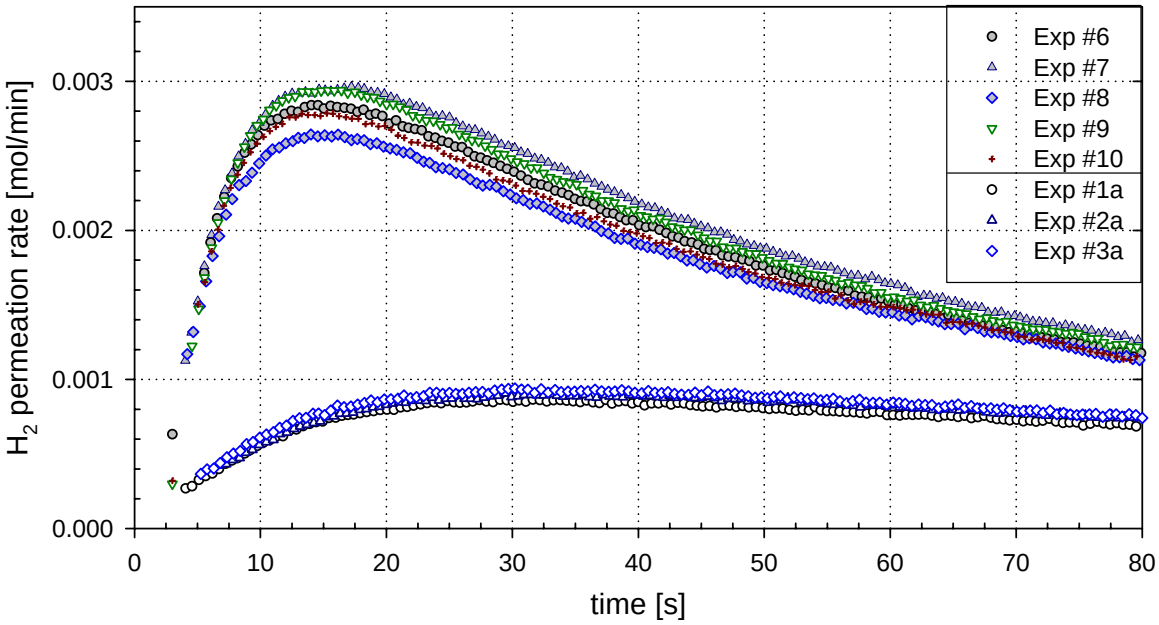

Figure 6.6. Hydrogen permeation rate measured by the gas analyzer for two operating temperatures. The lower data sets (1a, 2a, 3a) correspond to an operating temperature of 190 ± 5 °C, while the upper data sets (6-10) are at 250 ± 5 °C.

Under the operating conditions of these experiments, the hydrogen yield is limited both by the rate of permeation through the membrane, and mass transport in the bulk gas-phase of the reactor. The driving force for permeation of hydrogen through the

membrane is the partial pressure of hydrogen near the surface of the membrane, and as hydrogen becomes depleted, the permeation rate falls. By compressing the volume of the reactor, the hydrogen permeation rate can be maintained above the baseline (constant volume) value. To demonstrate this, the experiments were repeated, this time moving the piston forward during the cycle in order to shorten the diffusion length and to maintain an elevated partial pressure of hydrogen. The procedure for experiments with piston motion was similar to that listed above, with the following modification to Step 3:

3. When the filling process is complete, valve D and then valve A are closed; the reactor is left undisturbed for a fixed amount of time (e.g. 15, 20, 25 seconds); the piston driving screw is driven forward 1.25 turns in 10 seconds which corresponds to a linear speed of 0.5 mm/s; the reactor is left undisturbed again; meanwhile the mass spectrometer records the partial pressures of argon, helium, hydrogen, and carbon dioxide. Pressure in the reactor is monitored and recorded every 5 to 10 seconds.

These experimental results with piston motion are plotted in Figure 6.7 superimposed on data from the baseline cases that corresponded to the same initial pressure. A clear enhancement of the permeation rate is observed when the volume is compressed mid-cycle. Again, the uncertainty in the measurement of hydrogen flow (permeation) rate is as calculated previously.

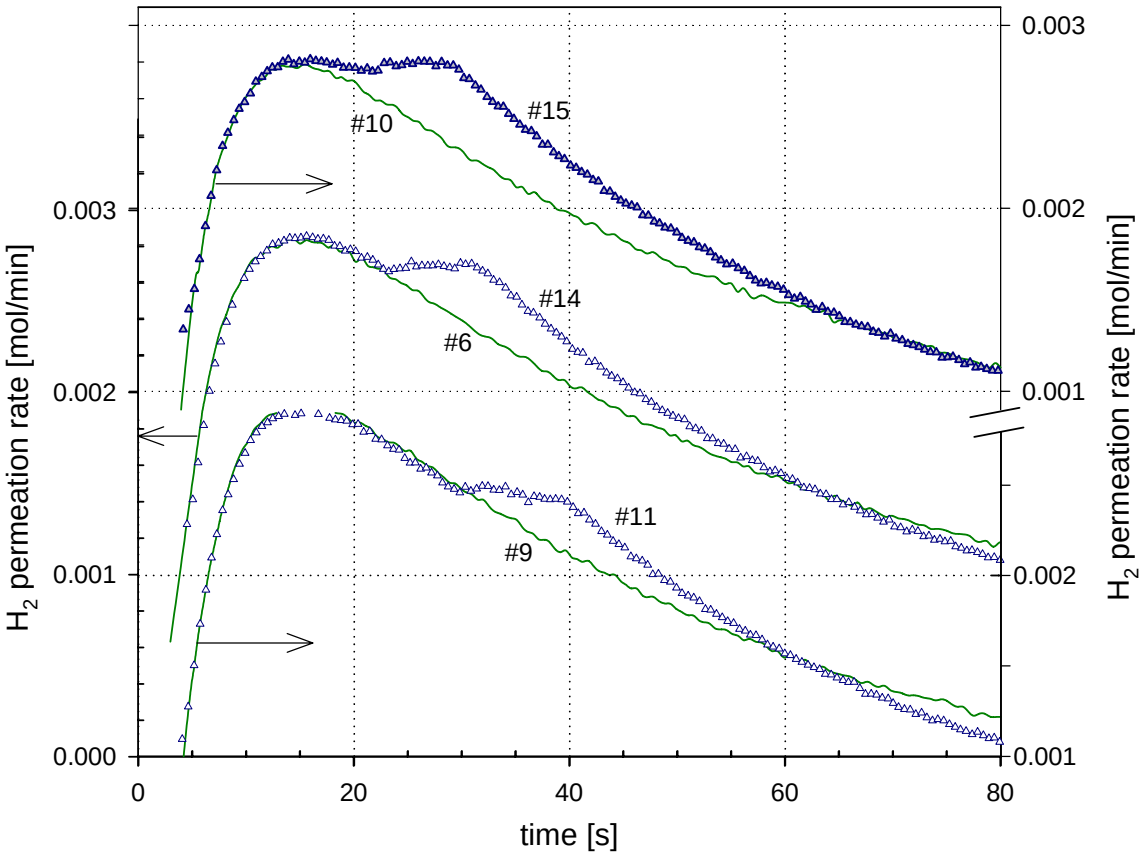

Figure 6.7 Transient profiles of hydrogen permeation rate (±11%) with and without volume compression. The experiments # 6, 9, and 10 are operated under baseline conditions (constant volume) while runs #11, 14, and 15 show enhanced hydrogen yield as a result of mid-cycle compression of the reaction chamber.

6.3 Model validation

The experimental results just reported, serve to demonstrate the overall feasibility of building and operating the variable volume, batch, membrane reactor. Additionally, the trends of baseline hydrogen yield and enhanced hydrogen yield were as expected and validate the present understanding of the key operating principles of the reactor.

Of equal interest is the ability of the numerical reactor model to predict the performance of the real reactor both qualitatively and quantitatively. In the model, the hydrogen flux permeating the membrane is assumed to follow the relationship,

$J = \frac{D_0}{\delta}\left(P_{H_2}{}^{1/2} - P_{\infty}^{1/2}\right)$, as described in Chapter 4. Typically, the membrane permeability, D_0 is assumed constant—here its value was obtained from a colleague [76] who tested the 54 μm thick palladium foil in pure gas (helium and hydrogen) experiments and measured the permeability, $D_0 = 4.1x10^{-6}\exp\left[-1387.9/T\right]\left[\frac{mol\ m}{m^2\ s\ kPa^{1/2}}\right]$. However, there is considerable evidence reported in the literature that the presence of the species found in the reacting mixture (CH_3OH, H_2O, CO_2, and CO) can have a deleterious effect on the membrane permeability, either through competitive adsorption or blocking of active sites on the surface. Carbon monoxide in the mixture has been singled out as being especially harmful, even in concentrations less than 1% by volume; however, its effects on membrane permeability are reversible (i.e. not "poisoned").

For example, Amandusson [77] tested a 25 μm thick palladium membrane and reports a 10% decrease in the ideal (pure gas) permeation rate when the retentate mixture contained equal parts hydrogen and carbon monoxide. This was measured at a membrane temperature of 250 °C, but much more severe CO-induced drops in permeability were reported at lower temperatures where surface reactions play a significant role in determining the total hydrogen flux through the membrane. On the other hand, Cheng [46] reports that permeation through a palladium membrane decreased to 1/5 of its initial (pure gas) rate when exposed to a Towngas mixture (CH_4, CO_2, H_2, and CO), but this effect was partially ameliorated in palladium-silver (Pd-Ag) membranes. (Although the state-of-the-art in hydrogen membranes is Pd-23%Ag alloy, the membrane in the present study is constructed out of pure palladium foil due to its immediate availability from the external vendor.)

In a more thorough study, Chabot [78] tested a 250 μm thick Pd-Ag membrane to measure the hydrogen flux for gas mixtures with small amounts of CO. Even with very small concentrations (e.g. 0.2 vol.%) of CO in the hydrogen mixture, the inhibiting effect can be significant. As seen in Figure 6.8, the inhibiting effect of CO depends strongly on temperature, but once the volume fraction of CO exceeds 5-10%, the membrane surface becomes "saturated" and higher levels of CO have little effect. Also at play is the transition between the rate limiting steps for permeation through the membrane. At higher temperatures (and with thicker membranes) the permeation is limited by diffusion through the solid Pd-alloy matrix and surface effects have negligible influence on the hydrogen flux. The membrane of Chabot [78] is nearly five times thicker (250 μm) than in the present study (54 μm) therefore it is expected that in the present study, surface effects (and CO in the mixture) will be even more noticeable and should be taken into account.

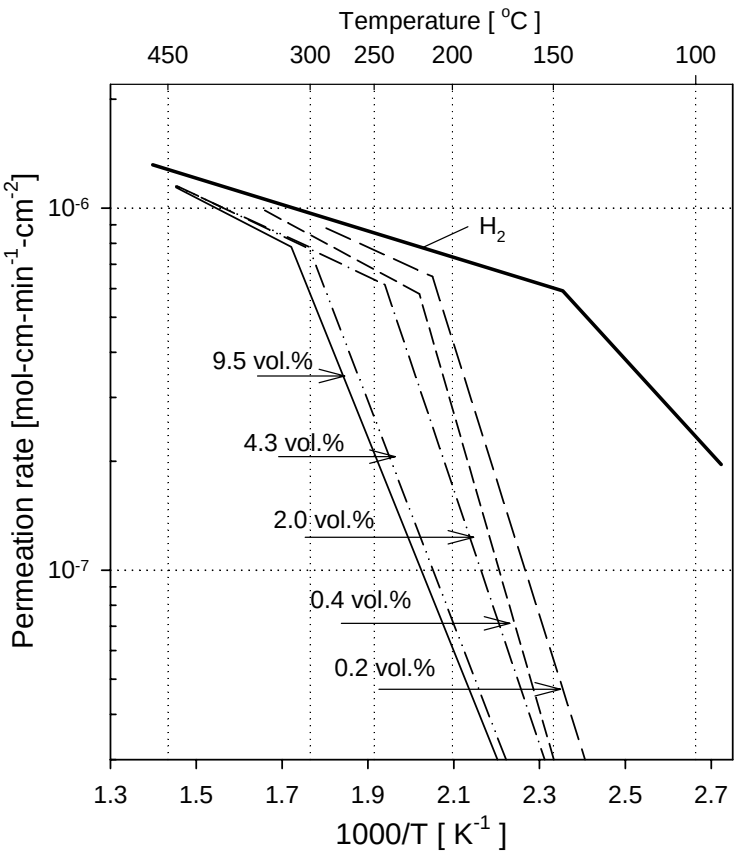

Figure 6.8 Inhibiting effect of various CO concentrations on the hydrogen permeation through a Pd-Ag membrane. (reproduced from Chabot, et al. [78])

Most recently, Peters [79] tested an ultra-thin Pd-Ag membrane (2.2 μm) at 400 °C and reports approximately a 50% decrease in permeation due to the presence of 5% CO by volume. The flux (relative to its ideal value) appears to fall with an exponential dependence on the molar fraction of CO in the feed (see Figure 6 in the referenced work), implying that the permeability roughly follows the relationship,

$$\frac{D}{D_0} = 1 - k_0 \exp\left[-A / x_{CO}\right] \tag{6.5}$$

The pre-exponential, k_0 and the constant, A can be approximated from the data reported [79] but can also be adjusted to provide a better fit to the experimental data here. This equation is plotted in Figure 6.9 showing the relationship between relative flux and

concentration of CO. As the mole fraction of CO goes to zero, the relative permeability approaches 1. As the mole fraction increases beyond 5%, the relative permeability levels off and increasing the concentration of CO has little effect. Thus, the numerical reactor model was modified so that the permeability of the membrane depends on CO concentration at the surface of the membrane according to Eq. (6.5).

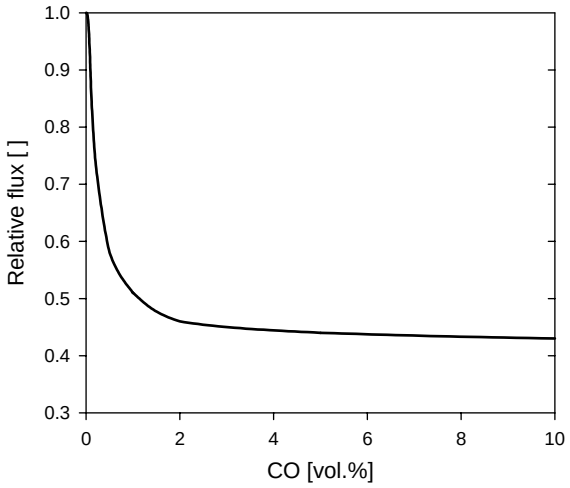

Figure 6.9 Dependence of membrane permeability on CO concentration (k_0 = 0.58, A = 0.0016).

Figure 6.10 shows the model predictions of hydrogen yield compared to a representative experimental run. Also shown is the CO concentration at the surface of the membrane, which affects the membrane permeability as just described. The model tends to over predict the hydrogen permeation rate initially and then predicts a more rapid drop as the hydrogen becomes depleted. This discrepancy can be explained not only by multi-dimensional effects in the real reactor (not truly 1-D), but also by the presence of helium used as a purge gas in the experiments, which dilutes the fuel mixture and diminishes the expected pressure rise in the reactor. (A 2:1 ratio of moles of product to reactant is expected, but the presence of a diluent lowers this ratio and hence the expected

pressure rise.) Ultimately, the diluted mixture results in a smaller driving force for permeation, hence, a reduced hydrogen flow rate.

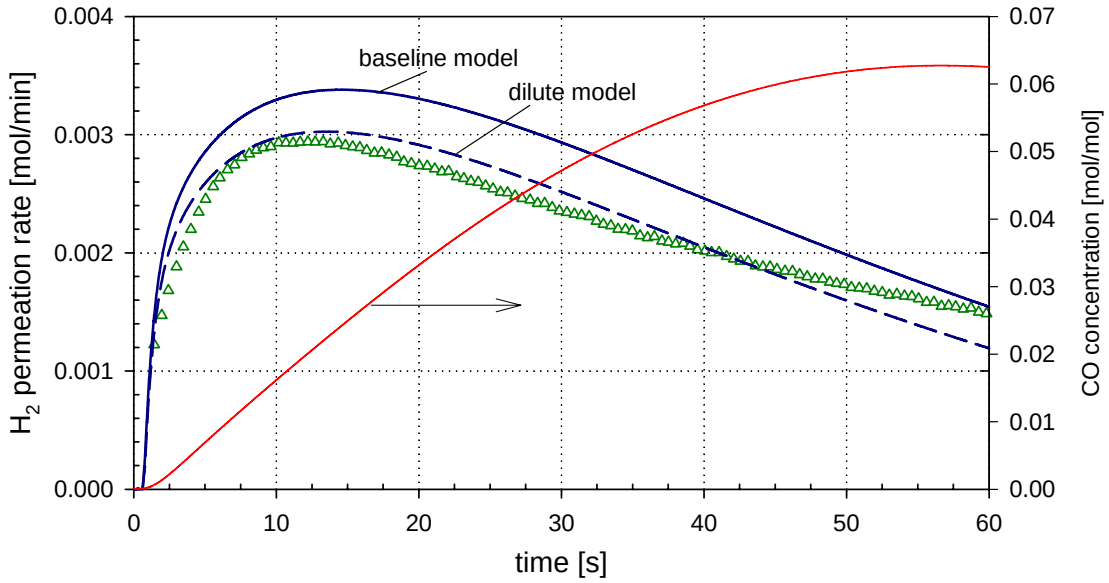

Figure 6.10 Comparison of experimentally measured hydrogen flux (run #9, flux ± 11%) and model predictions of hydrogen yield rate. The baseline initial condition assumes a pure fuel mixture in the reactor, while the dilute model assumes that the fuel mixture was initially diluted by helium (17%) that remains in the reaction chamber. Also, shown is the model prediction of molar concentration of carbon monoxide at the surface of the membrane.

The initial pressure in the reactor was slightly above atmospheric (1.2 atm, or 17.5 psi) as can be seen in Figure 6.11. It is reasonable to assume that this excess pressure corresponds to undisplaced helium from the filling process. That is, the fuel mixture is diluted with approximately 17% helium (0.2 atm / 1.2 atm). The numerical reactor model was solved for this dilute mixture case (including helium as an additional, but non-reacting species) and the result is a better prediction of both hydrogen yield and total pressure inside the reactor as seen in Figures 6.10 and 6.11.

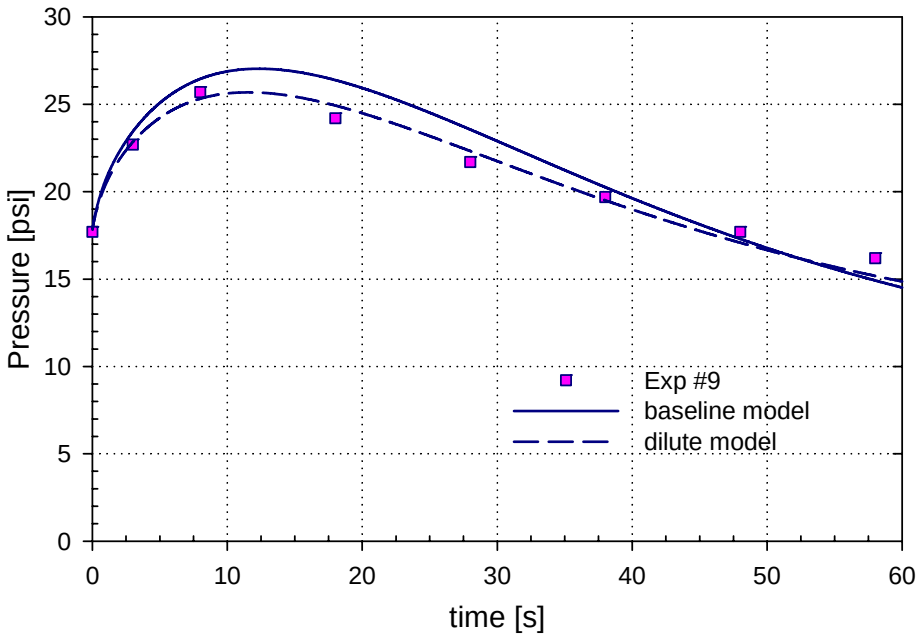

Figure 6.11 Comparison of experimental data and model predictions of total pressure in the reactor. The uncertainty in pressure measurements is ±0.25 psi and time ±0.5 second. The baseline and dilute models are the same as those in Figure 6.10.

The model is also well able to predict the hydrogen output and pressure in the reactor when the volume is compressed by the piston. In Figure 6.12, the experimental data from experiments #9 (constant volume) and #11 (with compression) are compared to the corresponding model predictions. The model assumes a dilute fuel mixture as previously described. In Figure 6.13, the pressure data from experiments #10 (constant volume) and #15 (with compression) are compared to the corresponding model predictions, with good agreement.

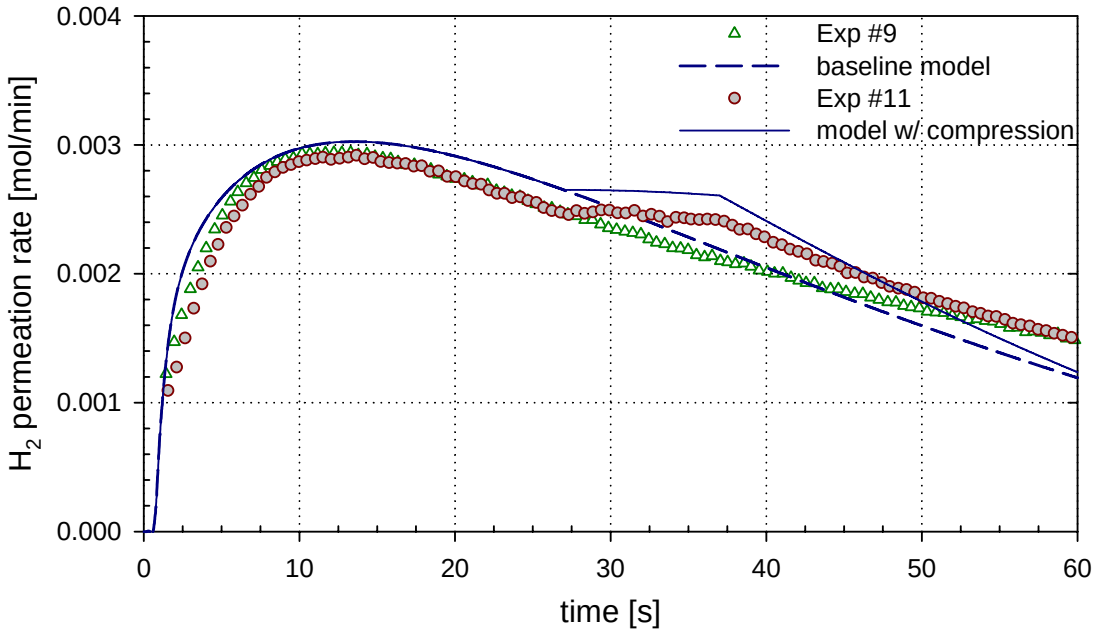

Figure 6.12 Experimental (uncertainty ± 11%) and model predictions of hydrogen output for the baseline case (constant volume) and the case with mid-cycle compression of the reactor volume.

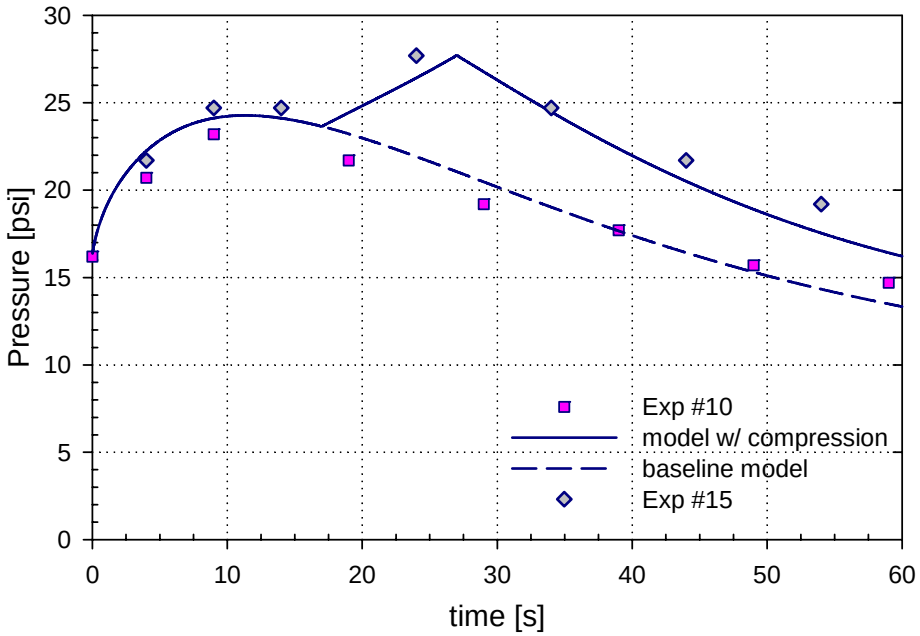

Figure 6.13 Transient pressure profiles in the reactor with and without volume compression. The initial pressure for these cases was 1.1 atmospheres, and the corresponding dilution of the fuel was 10% helium.

6.4 Conclusions

The experimental results illustrate that the variable volume, batch, membrane reactor concept is able to be realized for practical operation. More importantly, the theoretical model captures the relevant, coupled physical processes, and is able to predict the hydrogen output in a repeatable fashion with reasonable accuracy. The testing and characterization of these two reactors provides validation of the key operating principles of CHAMP reactors including 1) verification that the expected dominant reaction (steam reforming of methanol) is taking place, 2) appropriateness of the coupled reaction kinetics, membrane permeation, mass transfer, and volume compression models for predicting the rate of hydrogen yield, and 3) the ability to operate the batch reactor in both fixed-volume and variable-volume modes.

To demonstrate operation of a reactor that is designed for optimal performance requires several improvements to the test setup. Optimally, the reactor would have a thinner membrane (< 25 μm) that gives a much higher permeation rate. The processes of filling the reaction chamber with fuel, opening and closing valves, and driving the piston forward and back should be automated and electronically controlled for better range and precision of operation. The piston and cylinder should be constructed of stainless steel with closer tolerances to provide a robust seal and allow high pressure operation. Dead volume in the cylinder must be avoided, so that the piston is able to completely flush out the reaction mixture on the discharge stroke. The reactor must be very well insulated to minimize heat losses and allow a greater degree of control of temperature. The temperature and pressure data should be recorded automatically through a data acquisition system that is linked to the mass spectrometer readout.

These improvements will allow operation and study of an optimally designed reactor at a wider variety of operating points.

CHAPTER 7

CONCLUSIONS AND DIRECTIONS OF FUTURE RESEARCH

The CHAMP-class of batch reactors described in this thesis is well-suited for scalable production of hydrogen for distributed or portable applications. These reactors enjoy both fundamental and practical advantages over comparable, traditional continuous flow designs. A comprehensive reactor model was developed for simulating the reactor operation and exploring the design space for optimal points. The transitions between reaction-limited, permeation-limited, and diffusion-limited regimes have been mapped out and provide valuable insight into optimization of the design parameters, including temperature, reactor size, membrane thickness, and low-side hydrogen partial pressure. Additional insight was gained with respect to the optimal *operating* parameters, such as initial displacement of the piston, residence time, and transient profile of piston motion (if any).

In fixed-volume mode of operation, the residence time is precisely controlled to provide the desired trade-off between efficiency and power output. Recognizing that the reactor can operate at an elevated constant pressure—maintained by a pressure-following piston trajectory—opens up otherwise inaccessible regions of the efficiency-power parameter space. The ability to dynamically control the reactor volume, mid-cycle, to achieve the desired blend of efficiency and power is unique to the CHAMP-class of reactors.

Supporting the theoretical analysis, experimental characterization of a working bench-scale test reactor was performed. The experimental data served to validate the key

operating principles of CHAMP reactors including 1) verification that the expected dominant reaction (steam reforming of methanol) is taking place, 2) appropriateness of the coupled reaction kinetics, membrane permeation, mass transfer, and volume compression models for predicting the rate of hydrogen yield, and 3) the ability to operate the batch reactor in both fixed-volume and variable-volume modes.

7.1 Research issues for reactor development

Because this is only the first in-depth study of batch reactors for fuel processing and catalytic hydrogen production, there is much uncharted territory to cover in future research efforts:

- Refinement of numerical models (including multi-dimensional effects and non-isothermal modeling, for example),
- further analysis of various operating modes including the recycling of reaction products with the fuel stream (regenerative fuel processing), different fuels (other than methanol) and reaction mechanisms (such as autothermal reforming),
- development of other practical embodiments such as CO_2-membrane integrated reactors, and multiple piston/reaction chambers as described in Chapter 3,
- integration of the unit reactor into a coupled, multiple-unit stack, providing the desired total hydrogen yield required by the power plant
- optimization of the reactor as part of the whole power generation/energy conversion system, and not just an isolated, stand-alone fuel processing unit (see next section)

- development of active feedback control systems for taking advantage of the CHAMP's capability for dynamically variable volume and precisely controllable residence time to achieve the desired power output/efficiency trajectory
- practical considerations such as robust design of seals for wear resistance and high pressure operation under cyclic loading, compact driving mechanisms for actuating the piston or flexible diaphragms, ultra-thin but mechanically robust membranes able to withstand elevated operating pressures and without degradation of performance in the presence of reaction species
- advanced prototypes and experimental studies supporting all of the above mentioned efforts

I believe that as CHAMP reactor technology matures through efforts such as these, it will achieve commercial viability in time to meet future demand for distributed hydrogen production capacity.

7.2 System level issues and required developments

One motivation for development of this reactor is the fact that it is a central component to the sustainable carbon economy outlined in Appendix A. A primary driver is the need to avoid CO_2 emissions to the environment, and supply renewable energy to distributed power applications. To this end, a cost comparison should be made, not with energy conversion devices that pollute and use a non-renewable primary energy source, but with components of a potentially emission free, sustainable system. Devices that fit these criteria are reviewed briefly in Appendix A and include batteries, fuel cells with onboard hydrogen storage, and engines that burn biofuels. At the moment, all of these

technologies look “expensive” and/or face roadblocks in their path to widespread practical use. Further, they are currently actively researched and evolve very rapidly, making detailed cost analysis based on present estimates of little predictive value. Rather, it may be more productive to focus on the technical challenges of implementing these technologies, rather than their future cost.

When the capture of CO_2 emissions is incorporated as an additional step in the energy conversion process, the efficiency of the system is reduced. The engineering challenge is to minimize this energetic penalty through both systems level solutions and improvement of system components. To illustrate the method for estimating the additional work required to capture and liquefy CO_2 emissions, a specific system is analyzed.

Figure 7.1 shows a conception of one system that incorporates the CHAMP reactor with a fuel cell, and CO_2 capture/storage. The CHAMP reactor is designed to operate at 10 bars total pressure, taking in vaporized fuel mixture and providing pure hydrogen to the anode of the fuel cell at approximately 1 bar (see Sections 3.4.2 and 4.5.2 for a discussion of high pressure operation). The system is closed, operated in a cycle, with the batch reactor piston pneumatically actuated using high pressure CO_2 and integrated with a resistive film heater in intimate contact with the catalyst. Only one reactor unit is shown, but there could be many stacked together providing the necessary rate of hydrogen generation for a desired power output. The rate of consumption of methanol depends on the desired power output, lower heating value of methanol, and efficiency of the entire process. The rate of production of CO_2 is the same as the rate of consumption of methanol (1:1 molar ratio). For example, if 100 kW of power output is

required and the entire plant is assumed to be 25% efficient, then the rate of production of CO_2 is,

$$\dot{n}_{CO2} = \frac{100\ kW}{25\%\left(638.2\ kJ\ /\ mol\right)} = 0.63\ mol\ /\ s \tag{7.1}$$

If the efficiency of the system is lower than what was assumed in this example, then the rate of production of CO_2 will increase—for the same power output.

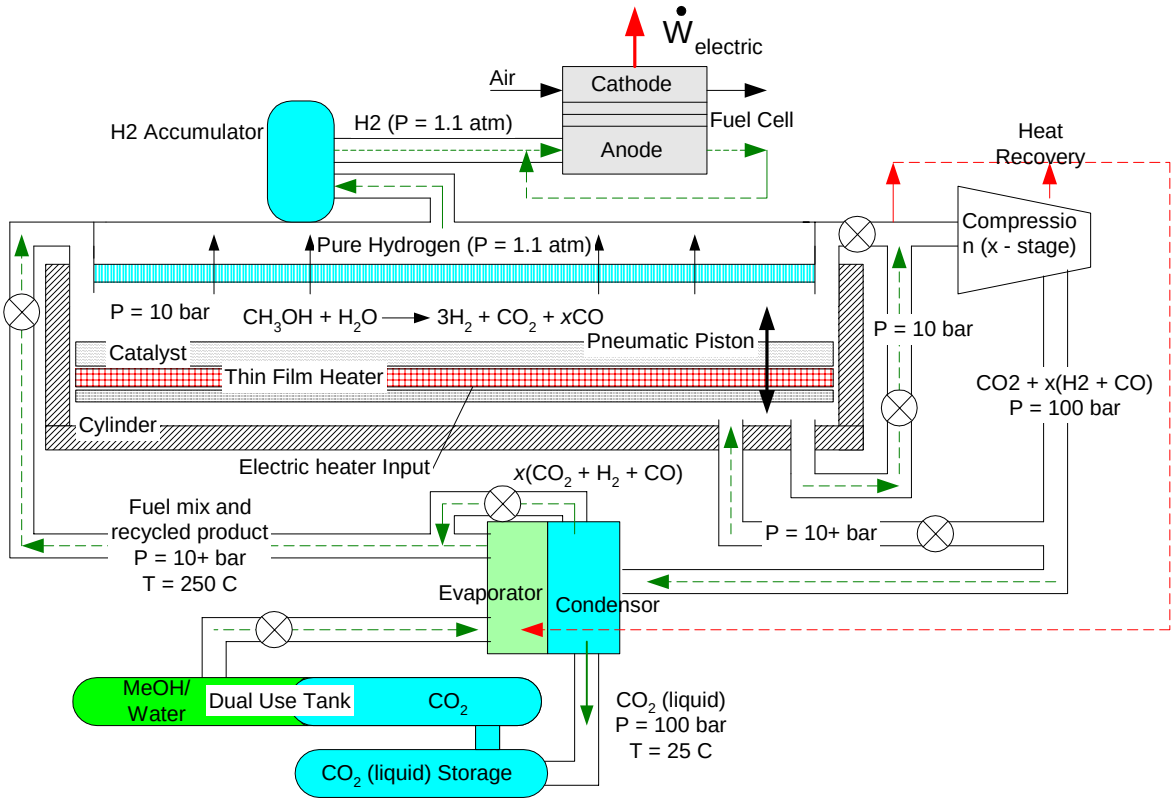

Figure 7.1 Conceptual design of a fuel cell-based system with onboard steam reforming in the CHAMP reactor, capture of the CO_2 byproduct, and recycling of the exhaust stream.

The exhaust coming out of the reactor is at a pressure of at least 10 bars and contains mostly (~90%) CO_2. For illustration purposes, the following process for compressing and liquefying the CO_2 is considered:

1) the exhaust is cooled from 250 to 95 °C by transferring approximately 9,700 kJ/kmol of heat to the liquid fuel mixture in a heat exchanger, heating the liquid from 25 - 85 °C (P = 10 bar). Using the example above (100 kW of power output and the flow rate of CO_2 calculated in Eq. (7.1)), the heat transfer rate for this heat exchanger is 6.1 kW.
2) the CO_2 is compressed from 10 bars to 100 bars in the compressor (multi-stage if necessary). Assuming an isentropic efficiency of 50% requires work input of 23,260 kJ/kmol (or power input of 14.7 kW) and heats the CO_2 to 535 °C.
3) the CO_2 is cooled to approximately 140 °C by transferring 20,500 kJ/kmol of heat to the fuel mixture in an evaporator (with a heat transfer rate of 12.9 kW). The liquid fuel mixture begins changing phase to vapor (the saturation temperature of water and methanol is 180 °C and 137 °C, respectively, at P = 10 bar). This may be done in multiple stages with multiple heat exchangers in conjunction with Step 2, to limit the peak temperature.
4) the CO_2 is condensed to liquid at 100 bars and its temperature brought down to 25 °C by removing an additional 13,300 kJ/kmol of heat (i.e. 8.4 kW) and rejecting it to the environment in a radiator/heat exchanger.

All of these numbers were calculated using the EES software package, and the equations are reproduced in Appendix D.

The additional power required for the CO_2 capture system is that in Step 2, to compress the exhaust, 14.7 kW. Also, hardware such as compressors, heat exchangers, tubing, valves, and control systems must be added. The peak temperature in Step 2

represents a challenge that requires either 1) a compressor capable of operating at high temperatures, or 2) multi-stage compression with intercooling (i.e. a repeat of Steps 2 and 3) which adds hardware to the system. Notice, however that the heat rejected during cooling of CO_2 in Step 3 is recovered to vaporize the fuel. This 12.9 kW represents a savings in the energy balance that helps to offset the penalty for CO_2 capture. If multiple intercoolers are used in conjunction with multi-stage compression, then the waste heat at each cooling stage should be recovered to heat/vaporize the fuel.

This simple illustration provides guidance for broader areas of future research and development that are required for realization of a complete system, in addition to the reactor-specific research needs already stated in the previous section. These include:

- compact, high efficiency, (possibly high temperature) CO_2 compressors
- compact, high efficiency CO_2 heat exchangers/condensers able to withstand elevated pressures
- lightweight, high pressure liquid CO_2 storage tanks

Solution of these important engineering challenges, should lead to the emergence of economically viable systems for power generation with integral CO_2 capture in the foreseeable future.

APPENDIX A

THE SUSTAINABLE CARBON ECONOMY

The following has been reproduced in part from:
[Damm D. L. and Fedorov A. G. (2008). "Conceptual study of distributed CO_2 capture and the sustainable carbon economy." Energy Conversion & Management **49**: 1674-1683].

Background

Environmental concerns over rising CO_2 concentrations in Earth's atmosphere are driving efforts to reduce anthropogenic emissions of CO_2. Currently, levels of CO_2 are over 30% higher than pre-industrial levels (approx. 280 ppm), and while there is a lack of consensus on what level of atmospheric CO_2 is "safe", evidence exists that elevated CO_2 concentrations are already causing perturbations to the climate [80] and harming critical ecosystems such as coral reefs [81]. According to the Intergovernmental Panel on Climate Change (IPCC) [80], approximately three-fourths of the increase in atmospheric CO_2 is attributable to the burning of fossil fuels. If the carbon in all of the estimated fossil fuel reserves were emitted to the atmosphere, the carbon concentration would rise to more than 5 times pre-industrial levels [82]. Following the current trajectory of energy usage and carbon emissions, atmospheric CO_2 will be double the pre-industrial level by the end of the 21st century. This level has been suggested as a plausible long-term stabilization goal, although it would likely require that carbon emission-free energy sources totaling 15 terrawatts (TW) be available by mid-century [83]. This is a significant challenge, considering that current global energy consumption is approximately 12 TW—the vast majority of which is not carbon-free.

The first step in meeting this challenge is to explore every feasible pathway for reducing carbon emissions, so that all available options are on the table. These pathways generally fall into three broad categories:

1) reduced energy consumption, either through conservation, improved efficiency, economic contraction, or some combination of these

2) displacement of fossil fuels by renewable, or carbon-neutral energy sources
3) capture and storage of CO_2 emissions, both passively (through increased uptake by biological carbon sinks) and by active sequestration in permanent repositories

It is clear that implementation of all three of these options will be necessary if CO_2 emissions abatement becomes a serious global priority. That is, a decrease in energy consumption, combined with increased reliance on alternative energy sources, as well as implementation of CO_2 sequestration and storage technologies are forthcoming in the near to mid future.

Active CO_2 sequestration requires carbon emissions to be captured and stored in a form or location that is isolated from the atmosphere on a millennial time scale. Numerous promising options for storage, such as within geological formations [84], under the oceans [85], or in solid carbonate form [86] are being studied extensively but are beyond the scope of this work. Most CO_2 capture efforts are focused on large-scale, stationary point sources of CO_2 such as power plants which produce 30% of emissions in the U.S. [87]. These sources feature steady-state, continuous operation, large physical size, and relatively high efficiency, making them an attractive target for implementation of state-of-the-art capture technologies. On the other hand, emissions from the transportation and small-scale distributed power sectors contribute more than 2/3 of global carbon emissions [15] and are considerably more difficult to capture. In particular, transportation applications provide the most difficult challenge because of their transient operation, constrained size and weight, often harsh operating environments, and the need to maximize efficiency without sacrificing performance. For these reasons it is nearly universally assumed that emissions from small-scale distributed energy sources cannot practically be directly sequestered, either onsite or onboard. Numerous examples of this assertion exist both in the scholarly and popular scientific publications.

However, the motivation for distributed CO_2 capture lies not only in its potential as a short term solution to the problem of carbon emissions, but more importantly, as a critical component of the sustainable carbon economy that is outlined below. For this reason, the existing assumptions are challenged by first theoretically establishing the

feasibility of distributed CO_2 capture, and then briefly analyzing several conceptual system designs that practically support implementation of the sustainable carbon economy. This is done in contrast to several other frequently discussed pathways for mitigation of carbon emissions from the transportation sector, which are briefly reviewed in next. While the discussion will focus primarily on the transportation sector, the analysis is equally valid for any distributed power generation application where efficiency, energy density, and sustainability are critical concerns. I must emphasize that onboard/distributed fuel processing with CO_2 capture is not intended to compete with today's polluting vehicles, but could be an important future technological solution if and when society demands CO_2 emission reductions.

Review of Strategies for CO_2 Emissions Mitigation

Currently, several pathways to elimination (or displacement) of carbon emissions from the transportation sector are being actively researched and receive serious consideration in the literature.

Electric vehicles

The first approach, using battery electric vehicles, is a fundamentally attractive pathway to elimination of carbon emissions from the transportation sector. Electricity is generated in a large-scale centralized location from renewable sources or from fossil fuels with the CO_2 sequestered centrally. The electricity is efficiently distributed throughout the grid, then transferred to and stored in batteries on the vehicle. This electric energy is converted to mechanical energy in the electric motors which propel the vehicle with no local emissions. The entire system is illustrated schematically in Figure A.1. Well-to-wheels efficiency is expected to be relatively high (compared to vehicles with internal combustion engines [88]); however, energy density and charging time of the batteries has so far limited the applicability to fleet or commuter vehicles. Continued advances in battery technology combined with reductions in cost are required for this proposed pathway to become widely acceptable. West and Kreith [89], as well as Van Mierlo, et al. [90], discuss battery electric vehicles in more detail and provide an economic analysis and comparison to other technologies. (Hybrid electric vehicles, while reducing emissions through improved efficiency, do not eliminate CO_2 emissions from the vehicle because they still burn a carbon based fuel to charge the battery.)

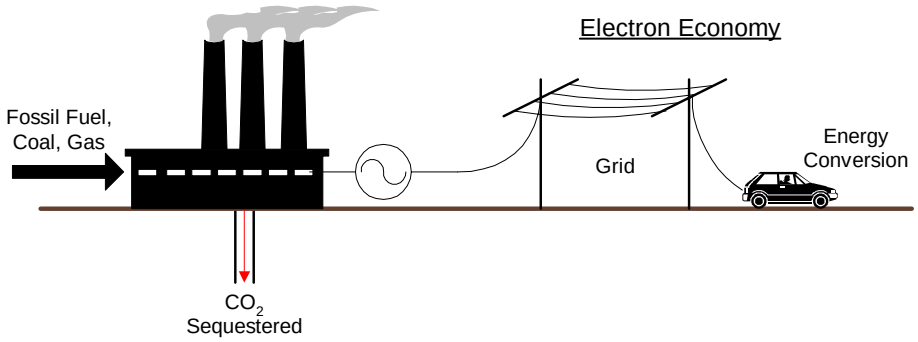

Figure A.1 Battery electric vehicles use the existing electric power production and distribution infrastructure, effectively centralizing the carbon emissions.

Hydrogen-fueled vehicles

Another option for zero carbon emission vehicles is the use of hydrogen as a fuel. The pure hydrogen fuel is produced at a central location (either from renewable energy sources or from fossil fuels with the CO_2 sequestered) and distributed through a newly created, hydrogen-refueling infrastructure similar in capability and magnitude to the current petrol infrastructure (refueling stations, pipelines, trucking, etc.). Hydrogen is stored onboard the vehicle at high pressures or in metal hydrides and burned in an internal combustion engine or electrochemically converted to electricity in a fuel cell. The system is illustrated schematically in Figure A.2. Azar, et al. [10] analyzes several feasible scenarios and concludes that widespread use of hydrogen fueled vehicles could lead to stabilization of atmospheric CO_2 levels. However, multiple economic and technological barriers to this pathway, including refueling, on-board hydrogen storage, investment in infrastructure, and safety must be overcome. Additionally, as Kreith and West [88] (as well as numerous other critics) point out, the well-to-wheels efficiency of a hydrogen- based transportation system is less than that of the current hydrocarbon-based system and would lead to increased fossil energy usage in the near term. These are not trivial challenges, and it is by no means certain that this envisioned pathway will soon become reality.

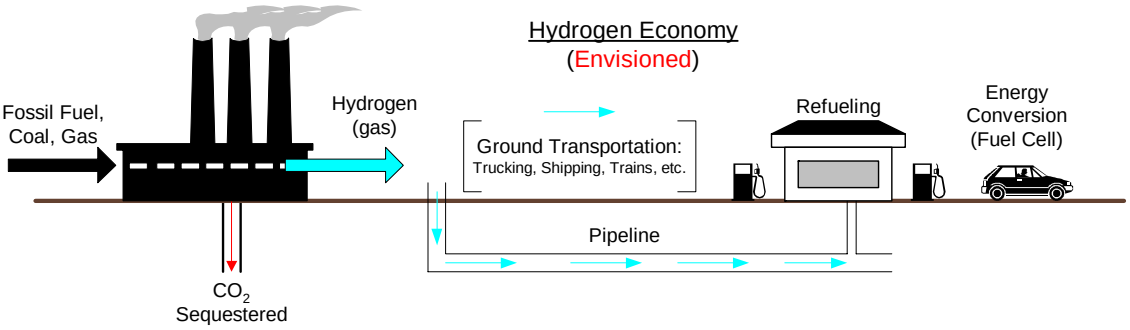

Figure A.2 Necessary infrastructure for a hydrogen-based transportation system with CO_2 sequestered centrally at the hydrogen production facility.

Carbon neutral biofuels

An alternative pathway that accommodates a wide variety of portable energy conversion devices, including the highly developed and mature internal combustion engine, relies on carbon-neutral biofuels [91] or synthetic fuels. Biofuels are carbon-neutral (or negative) if they are synthesized from biomass using renewable energy sources, so that the CO_2 released upon conversion of the fuel, is balanced by carbon uptake from the atmosphere at some point during the cycle. For example, biomass comes from plants that have absorbed a quantity of CO_2 from the atmosphere during their lifetime. The biomass could be converted to a liquid fuel with no additional carbon input. When the fuel is consumed the CO_2 returns to the atmosphere and the carbon neutral cycle is completed. Although this represents a sustainable cycle that may be cost-effective for transportation applications [10], the magnitude of resources available for carbon neutral biofuels is likely insufficient for widespread use, as illustrated by the fact that all of the land area currently devoted globally to agriculture would need to be devoted to biomass to provide 10 TW of energy [83].

CO_2 capture from the air

An additional pathway proposed by Lackner [92] is a business-as-usual scenario wherein vehicles continue to use carbon-based fuels (either by combustion or in fuel cells), and continue to freely emit CO_2 into the atmosphere. Large, centralized facilities located adjacent to geologic storage sites would be built to remove atmospheric CO_2 from the air. However, because dumping CO_2 into the atmosphere dilutes it to atmospheric concentrations (<400 ppm), the energetic penalty for separation downstream is maximized. Additionally, to reduce atmospheric concentrations by *x*% requires filtering

at least *x*% of the entire atmosphere [32]. Although this may be technically feasible, it would require a large investment in infrastructure, and significant land-use designations, none of which have been seriously proposed thus far.

Distributed CO_2 capture and storage

The final option, currently being given little or no serious consideration in the literature, is that of onboard/onsite CO_2 sequestration. Carbon dioxide that is produced by the consumption of hydrocarbon fuels would be captured and temporarily stored at the point of generation (e.g. on the vehicle). Refueling stations could double as CO_2 collection stations so that the vehicle could empty its CO_2 exhaust and then refuel in a single stop. In the literature, onboard CO_2 sequestration is often dismissed or mentioned in passing as too difficult, complicated, costly, or generally not feasible, with little or no analysis given to support this claim. One important exception is the work of Kato et al. [94] which proposed producing hydrogen from methane in an onboard fuel reformer with integrated CaO pellets [95] for CO_2 absorption via the reaction

$$\mathrm{CaO} + \mathrm{CO_2} \rightarrow \left(\mathrm{CaCO_3}\right)_{solid} \tag{A.1}$$

The spent reformer unit would be swapped for a fresh one when the vehicle refuels.

To the best of my knowledge this is the first and only serious effort in the literature to demonstrate a feasible system for capturing and storing CO_2 on board of a vehicle. I attempt here to outline several pathways through which on-board/on-site CO_2 sequestration in the transportation sector (or any other small-scale distributed source) is not only feasible, but can also lead to a sustainable energy system for distributed applications. This will allow another energy option to be on the table as society begins to demand and subsidize meaningful reductions in CO_2 emissions.

The Sustainable Carbon Economy

A key driver in the energy pathways just mentioned above, is the need to ultimately transition from a transportation system based on oil (whose supply is arguably finite) to one based on renewable (or nearly infinite) energy sources. Wind and solar energy are truly renewable, carbon-free energy sources, however they are intermittent, distributed, and are most effectively used to produce electricity which is easy to transport great distances but not easy to store densely and for a long time. The same can be said for nuclear and fusion energy which, while carbon free, are used to produce electricity,

not transportation fuels. If battery density, weight, and recharge capabilities were sufficient, the "electron economy" (see Figure A.1) would be most attractive because the number of inefficient energy conversion processes is minimized. The proposed "hydrogen economy" (Figure A.2) attempts to address these concerns by using hydrogen from renewable sources as the energy carrier; however multiple (and inefficient) energy conversion processes may reduce the overall efficiency of the system [88]. Additionally, hydrogen is one of the most difficult substances to transport and store densely due to its light, gaseous state and propensity to diffuse through solids. There is, then, compelling motivation to continue using the current liquid fuel infrastructure (illustrated schematically in Figure A.3) because of the energy density, ease of storage, and convenience in refueling the vehicle with liquid fuels. But eventually this liquid fuel must carry renewable energy rather than fossil-based energy.

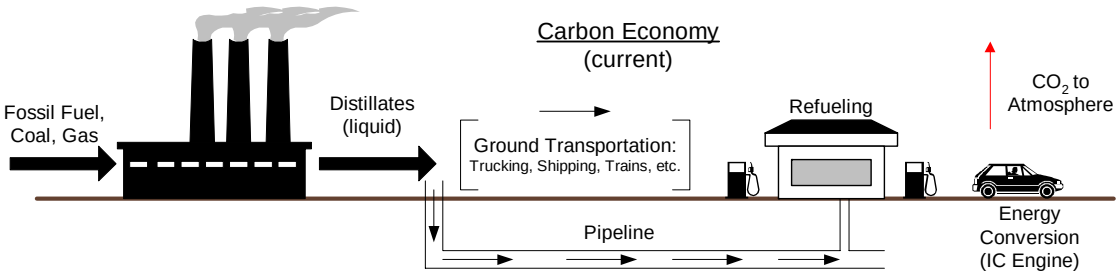

Figure A.3 The current infrastructure for providing energy to the transportation sector results in many distributed sources of CO_2 emissions.

If the CO_2 generated by the current system could be captured and stored on the vehicle, and then collected and sequestered, this would be a mid-term solution to the problem of distributed CO_2 emissions while still using much of the current infrastructure. This is illustrated in Figure A.4 and requires the development of technology to capture emissions at the source. The system in Figure A.4 seamlessly transitions into that shown in Figure A.5, wherein the captured CO_2 is now recycled back to a fuel processing plant and used to create a synthetic carbon-based liquid fuel such as methanol, for example. (In a similar system proposed by Kato, et al. [94], methane is produced.) Methanol synthesis by hydrogenation of CO_2 is a well-studied and mature process [96] given by the reaction,

$$CO_2 + 3H_2 \rightarrow CH_3OH + H_2O \qquad (A.2)$$

The energy input to produce the hydrogen needs to be renewable and the entire system is emissions free, leading to a *sustainable* "carbon economy". (Other feasible options for fuel production are certainly available including direct solar-thermochemical processing [97].)

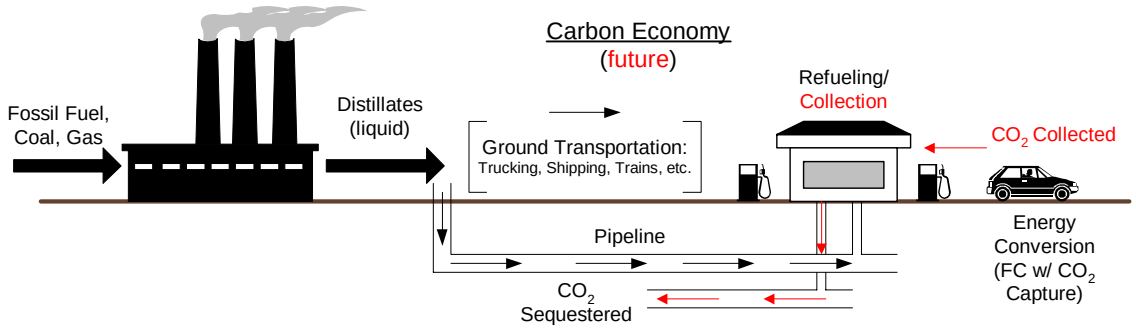

Figure A.4 In the near to mid future CO_2 could be captured onboard, collected through the current refueling stations, and delivered to a centralized sequestration site.

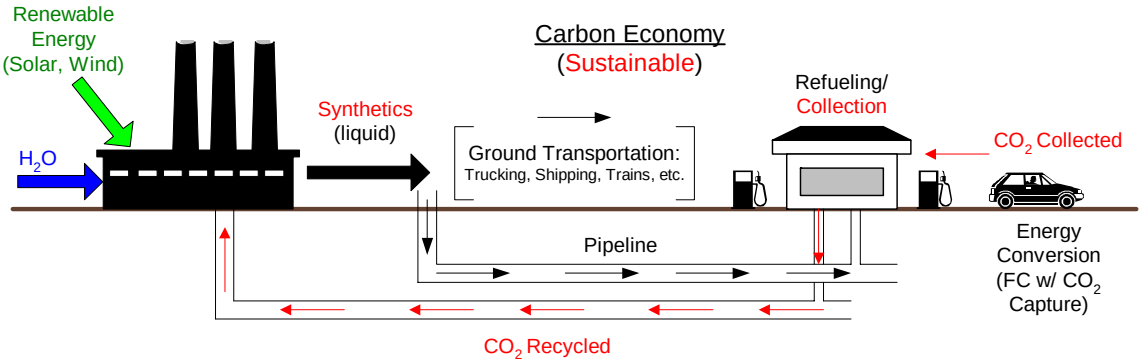

Figure A.5 Further in the future, as the renewable energy infrastructure is developed, the system in Figure 2.4 transitions to this "sustainable carbon economy", wherein recycling takes the place of sequestration.

An important aspect of the pathway just described is that development of technology to efficiently capture and collect CO_2 from distributed sources now, will enable the transition to renewables further on down the road. This is true because the existing infrastructure can be added to incrementally, requiring only minor modifications, and thereby avoiding the stalemate between supply-side and demand-side investment that often occurs when an entirely new infrastructure must be built from the ground up (as has

seemingly occurred with the so-called “hydrogen economy”). Therefore, distributed CO_2 capture may be a near term solution for carbon emissions abatement, as well as a long term enabler for the future sustainable distributed energy system based on liquid synthetic carbon fuel energy carriers.

Feasibility and Thermodynamic Analysis of Distributed CO_2 Capture

Scope

The first step in proposing a system for capturing distributed CO_2 emissions is to establish its feasibility, particularly for transportation applications where it is most difficult. The first assumption here is that the vehicles under consideration are carrying and consuming hydrocarbon fuels which generate CO_2 in the process of converting chemical energy to mechanical energy. Clearly the conversion process must be efficient enough that the vehicle will have sufficient energy left over for carrying a payload over a specified range before refueling. Additionally the power to weight ratio must be sufficient to provide the level of performance that consumers have become accustomed to. The system must have a rapid transient response to a variety of loads and operating conditions. The allowed physical size of the system is also fairly well-defined and should conform to currently available vehicles. The vehicle should also be easy to refuel/recharge (and additionally easy to discharge the collected CO_2). The efficiency penalty for CO_2 capture (due to the power consuming compressor and additional weight of captured CO_2 and additional hardware) should be made as small as possible. Finally, the cost of the system must be competitive with other commercially available technologies.

Although quantitative standards currently exist for all of these considerations, the additional requirement of CO_2 capture and storage may require these vehicle standards to be changed in the future. This will depend on the level of urgency assigned to capturing CO_2 emissions in the future. It would be rather futile to try to predict these future standards and use them now as design criteria. Therefore I am concerned with generally evaluating the technical feasibility, and quantifying the energetic penalty incurred by capturing, storing, transporting, and collecting the CO_2 that is generated by the vehicle’s power plant (or from any other small, distributed source).

Dilution of CO_2 exhaust stream

Sequestration of CO_2 from large scale power plants (such as electric power generating stations) has been given significant attention for more than a decade and three general classifications or approaches are being pursued [98]:

- post combustion/process capture, wherein CO_2 is sorbed from the flue gases (requires large scale equipment due to low concentrations of CO_2 in the exhaust)
- oxy-fuel combustion/processing, wherein pure O_2 is used as the oxidizing agent rather than air (requires a source of pure O_2)
- fuel decarbonization, wherein the carbon is removed from the fuel before being combusted or reacted in the energy conversion device (requires fuel pre-treatment)

The first of these is clearly not applicable to automotive, mobile, or small-scale applications due to the large physical size of the systems required for sorbing CO_2 from a diluted exhaust stream. Typical concentrations of CO_2 in an automobile exhaust are approximately 4%, as a result of using air (which is mostly nitrogen) to oxidize the fuel. Therefore, the first (and most critical) requirement for onboard CO_2 capture is that the "engine", or power conversion device, generates power without allowing the byproduct CO_2 to become diluted with air during the process. The latter two broad approaches satisfy this requirement and are adaptable to transportation applications.

Many standard processes that convert chemically-stored energy in a fuel to mechanical work ultimately rely on oxidation of hydrogen and carbon in the fuel to release the stored chemical bond energy. The challenge is to provide pure oxygen to the process rather than oxygen diluted in air. Significant advances have been made in oxygen membrane technologies which are reviewed more generally by Bouwmeester [99] and specifically for power generation with CO_2 capture by Bredesen, et al., [98]. In an internal combustion engine the fuel could be mixed with oxygen supplied from an oxygen membrane separator unit. The operating temperature could be optimized by recirculating the CO_2 byproduct into the fuel stream. Alternatively, in high temperature solid oxide fuel cells, the oxygen is separated electrochemically from air by the solid YSZ electrolyte and combined with hydrogen and carbon in the porous anode. The exhaust stream contains only CO_2 and water vapor. In low temperature polymer

electrolyte membrane (PEM) fuel cells, hydrogen (which has been de-carbonized) travels through the membrane and combines with oxygen from the air in the porous cathode. Fuel processing schemes such as autothermal reforming or partial oxidation reactions may be carried out in an oxygen membrane integrated reformer to produce the hydrogen for the fuel cell. The exhaust from these reformers is highly enriched in CO_2.

Alternatively, decarbonization processes that do not require the use of oxygen membranes are available. For example, steam reforming of hydrocarbon fuels produces hydrogen, carbon dioxide, carbon monoxide, water vapor, and other trace byproducts. If this reaction is carried out in a hydrogen permeable membrane reactor, then not only is hydrogen separated and purified, but the remaining byproduct stream contains a very high concentration of carbon dioxide which is amenable to capture.

The energy conversion processes just mentioned have received much attention in the literature and several are quite mature. They are discussed in more detail in the next section where conceptual system designs are proposed. Assuming that the vehicle power plant exhaust stream contains relatively "pure" CO_2, the next challenge is to store the CO_2 onboard until it can be unloaded at a centralized location. One option for dense storage is to compress and liquefy the carbon dioxide.

Thermodynamics of CO_2 liquefaction

Because energy efficiency of the zero emission power plant is critical, the magnitude of the energetic penalty for compression and liquefaction of CO_2 will determine its feasibility for transportation applications. Figure A.6 shows a liquid/vapor equilibrium diagram for CO_2 at ambient temperatures and elevated pressures. The critical temperature and pressure of CO_2 are 31 °C and 7.375 MPa, respectively [100]. As a baseline case, consider a quantity of CO_2 at standard temperature and pressure (T = 25 °C, P = 101.3 kPa). The ideal work required to compress the gas to a storage pressure of 10 MPa (approx. 1500 psi) and condense it to liquid, can be calculated from the change in entropy and internal energy,

$$W_{1-2} = T\left(S_2 - S_1\right) - (U_2 - U_1) = -30\ kJ/mol \qquad \text{(A.3)}$$

The properties are calculated from the equation of state given by Span & Wagner [101]. The number calculated in Eq. (A.3) represents the minimum thermodynamic penalty or the best that could ever be hoped for. This assumes an isothermal compression process

which is usually not practical in small-scale, compact applications. A more realistic approach is the isentropic compression processes described with greater detail in section 7.2.

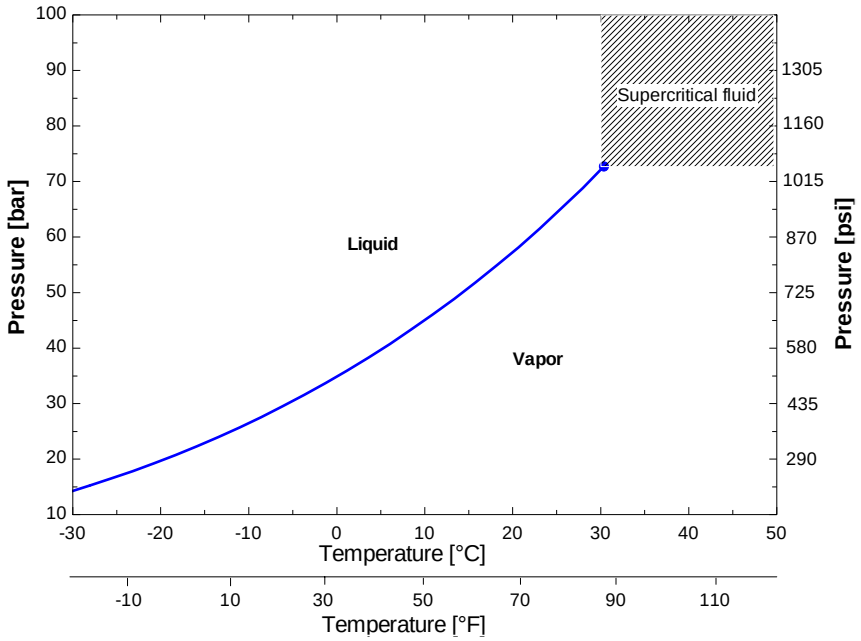

Figure A.6 Liquid/Vapor diagram for CO_2

To evaluate this in terms of available energy content of the fuel that is consumed in producing the same amount of CO_2, consider, for example, steam reforming of methanol producing hydrogen for use in a PEM fuel cell. As discussed previously, methanol synthesis, Eq. (A.2), requires energy input, which hopefully could come from renewable sources. The steam reforming reaction is endothermic,

$$CH_3OH + H_2O \rightleftharpoons 3H_2 + CO_2 \qquad \Delta H = 49.2 \quad kJ/mol \tag{A.4}$$

indicating that an additional 49.2 kJ/mol of energy input per mole of fuel is consumed by the reaction [102] producing three moles of hydrogen. The hydrogen is electrochemically combined with oxygen in the fuel cell by the following reaction,

$$H_2 + \frac{1}{2}O_2 \rightarrow H_2O \qquad \Delta G = -228.6 \quad kJ/mol \tag{A.5}$$

where the available electrical work (Gibbs free energy) is 228.6 kJ per mole of hydrogen. The minimum energetic penalty of carbon dioxide liquefaction, as a percentage of the available electrical work in the fuel, is

$$\varepsilon = \frac{W_{1-2}}{\Delta H_{rxn} + 3\Delta G_{fuelcell}} 100\% = 4.7\% \qquad \text{(A.6)}$$

This number represents the minimum thermodynamic penalty, or the best that can be hoped for (though real systems can never achieve it). In a real system the penalty will be higher due to inefficiencies in the fuel reformer, fuel cell, and CO_2 liquefaction systems. For example, in section 7.2 the power required for a 50% efficient isentropic compressor was 14.7 kW (for the example of a 100 kW system). However, this penalty was partially offset by heat recovery.

In addition to the energetic penalty for CO_2 liquefaction, the weight and volume of the stored CO_2 is of concern for transportation applications. Fortunately, the weight and volume of liquid CO_2 produced, per mole of methanol fuel, is only about one-third higher than those of the methanol itself. The density of both, at ambient temperature (T = 25 °C) is approximately 800 g/liter, or 19 mol/liter for CO_2 and 25 mol/liter for methanol, depending on the storage pressure. Thus, a dual-use fuel tank can be designed to store the CO_2 byproduct as the fuel is being consumed, thereby minimizing the additional volume required for the capture system. It should be taken into consideration that other liquid fuels with higher carbon content, such as ethanol, gasoline, or diesel, will generate proportionately more CO_2. Therefore, from the perspective of CO_2 capture, methanol certainly is an attractive fuel on which to base the transportation sector (though it is used here as an example only).

Conceptual System Design and Analysis

Multiple options exist for designing a power plant that converts the chemical energy stored in a liquid fuel to mechanical or electrical work while capturing the generated CO_2. As previously mentioned, a critical requirement is to not allow the byproduct CO_2 to become diluted with air because efficient and compact separation of dilute streams is usually not practical on the small-scale. The simplest and most immediate option would be to run the internal combustion engine with pure oxygen from an oxygen membrane separator unit. Based on oxygen fluxes available from state-of-the-

art membranes [99], the unit would need an active membrane surface area on the order of 2 m^2 to power a vehicle (50 kW).

Here, two systems based on hydrogen fuel cells are illustrated, which have a higher theoretical efficiency and no toxic emissions (such as NO_x or SO_x) as compared to the internal combustion engine. In these examples methanol is used as the fuel because of its relatively high H/C ratio.

Autothermal fuel reforming with CO_2 capture

This system is centered around an autothermal fuel reformer such as the HotSpot™ reactor [19] developed by Johnson Matthey. Typically, air and fuel are mixed in the packed catalyst bed and the initial partial oxidation of methanol provides heat and water vapor for steam reforming of the remaining fuel. The net reaction is,

$$CH_3OH + 0.5\,(O_2 + 3.76N_2) \rightarrow CO_2 + 2H_2 + 1.88N_2 \qquad (A.7)$$

with no net generation (or consumption) of heat. Ideally, the product stream could be sent directly to the fuel cell where the hydrogen is electrochemically converted to electricity. However, the reaction also produces carbon monoxide which poisons the catalyst of PEM fuel cells, and because the hydrogen is dilute, the fuel cell efficiency is reduced. Additional reforming/reaction steps such as water-gas shift or preferential oxidation can be included to clean up the CO [19,26]. Here, a dense metallic (Pd-Ag alloy) hydrogen permeable membrane [45,46,49], is integrated with the reactor [20,58,103,104], to produce a virtually pure hydrogen stream. This leaves the byproduct stream enriched in CO_2, but still heavily diluted by nitrogen (from the air). To remedy this, the reactor is supplied with pure oxygen rather than air. The oxygen comes from an oxygen selective membrane integrated into the reactor, or from a separate oxygen membrane separator unit. Now, the exhaust stream is 80-90% CO_2 which is much more amenable to capture.

The byproduct stream is compressed through several stages, dried to remove water vapor, and condensed to liquefy the CO_2. The liquid CO_2 is stored in the dual-use fuel tank, and the remaining (uncondensed) vapor is recycled back to the fuel reformer. The entire system is illustrated schematically in Figure A.7. The system has no carbon emissions and utilizes 100% of the fuel (i.e. none is exhausted to the environment).

These are very important features of the system and will be discussed further in a following section.

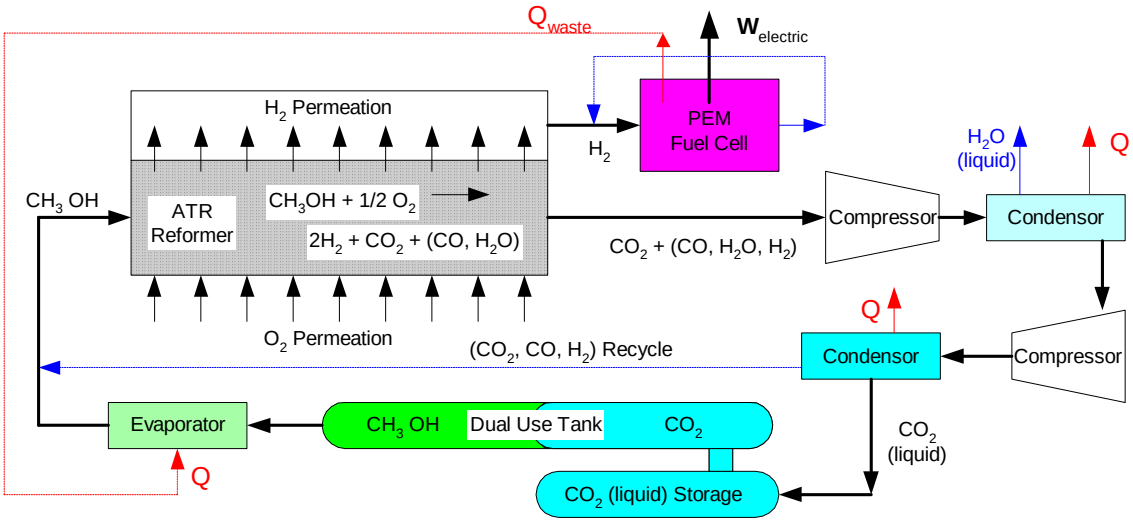

Figure A.7 Autothermal reformer and fuel cell system with integrated CO_2 capture and storage.

Steam reforming with CO_2 capture

An alternative system that avoids the use of oxygen permeable membranes is based on a hydrogen membrane integrated steam reforming reactor to supply hydrogen to the PEM fuel cell. Steam reforming of methanol is an endothermic reaction given by Eq. (A.4). This reaction does not require oxygen from the air, and so the problem of CO_2 dilution by nitrogen is avoided. The low quality heat (~250 °C) required for the reaction could be supplied by combusting a small amount of methanol or by electrical heating. After hydrogen separation, the byproduct stream from the reactor is enriched in CO_2 which can be liquefied and stored in a similar manner to that described in Section 2.5.1. The entire system is illustrated schematically in Figure A.8.

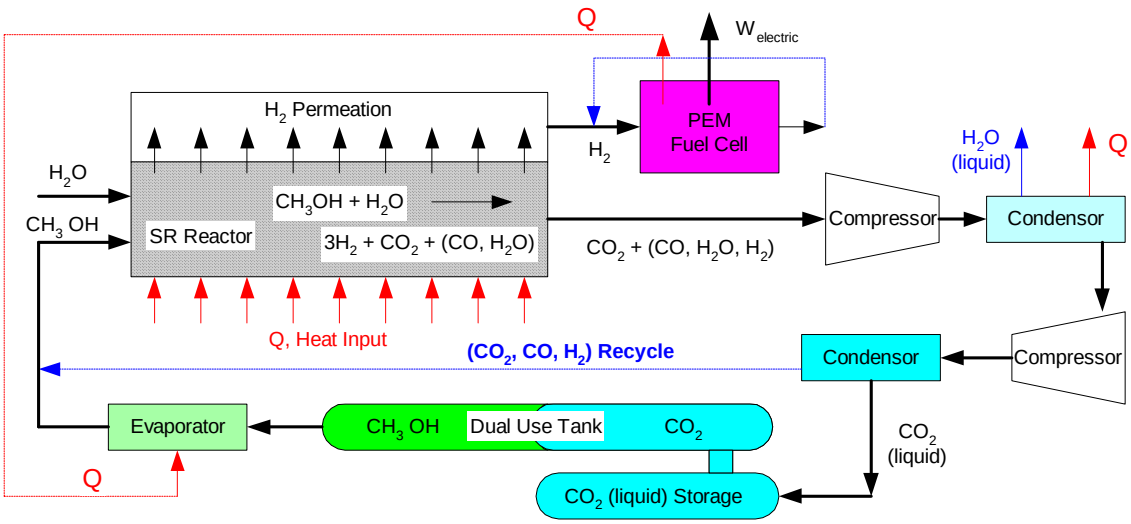

Figure A.8. Steam reforming reactor and fuel cell system with integrated CO_2 capture and storage.

Regenerative fuel processing

A novel feature of these systems is that removal of CO_2 from the byproduct stream allows the remaining products (including H_2 and CO) to be recycled back into the fuel reformer, giving rise to a "regenerative" fuel processing scheme. In conventional state-of-the-art systems, a certain amount of fuel products (such as H_2 and CO) are lost (exhausted to the environment or burned) because they are heavily diluted in air or CO_2 and cannot be efficiently converted or extracted. Here, because the bulk of the CO_2 is separated out, the resulting stream and its valuable fuel components are recycled—hence 100% of the fuel is utilized. Additionally, the energy content of this recycled fuel can partially (or completely, in some cases) offset the energetic penalty incurred by the CO_2 liquefaction system. The price that must be paid, however, is a marginal increase in the reactor volume to obtain the same rate of hydrogen production.

To clarify these points, equilibrium calculations of realistic reaction, separation, and liquefaction processes shown in Figure A.8 are employed. In this specific case, the reactor is assumed to operate isothermally (250 °C) at atmospheric pressure. Also, the hydrogen permeation is assumed to proceed to equilibrium, *leaving* 10% hydrogen (by mole fraction) on the reaction (retentate) side of the membrane. This is typical, because the hydrogen permeation is driven by the partial pressure difference across the membrane, and the partial pressure on the permeate side cannot practically be brought to

zero in most cases. Removal of hydrogen shifts the equilibrium of the reaction (Eq. (A.4)) towards the products, resulting in nearly 100% methanol conversion. The remaining mixture in the reactor is then, 3% H_2O, 3% CO and 84% CO_2 (by mole fraction). The actual composition (per mole of fuel) is given in Table A.1. The net hydrogen production (separated and sent to the fuel cell) is 2.85 moles per mole of fuel, compared to the ideal ratio of 3.0 moles per mole of fuel. The lost hydrogen (0.15 moles) could have been sent to the fuel cell to produce 34 kJ of electricity (according to Eq. (A.5)).

Table A.1. Composition of the steam reforming reaction product stream

Reaction products after H_2 separation

Species	Moles / Mole fuel
H_2O	0.035
H_2	0.117
CO	0.035
CO_2	0.965

Now, to fully utilize this valuable fuel, the CO_2 is separated from the byproduct stream by liquefaction. The mixture is compressed to twice the vapor pressure of CO_2 so that after it is condensed, the remaining gases contain only 50% saturated CO_2. The composition of this recyclable stream is given in Table A.2. The recycled products are fed back into the reactor, with the fuel/water mixture adjusted to the correct stoichiometry. For a given reactor volume, the net hydrogen production rate (separated and sent to the fuel cell) is now almost 15% lower than the case with no recycling because some of the fuel is displaced by CO_2. Therefore, to achieve the same power output, the reactor must be incrementally larger.

Table A.2. Composition of the recycled stream

Recyclable products after CO_2 liquefaction

Species	Moles / Mole fuel
H_2O	0.000
H_2	0.117
CO	0.035
CO_2	0.152

In addition to offsetting the energetic penalty of CO_2 capture, regenerative fuel processing redefines the parameter space for optimizing the membrane reactor. Previously, the optimal design would strike a balance between reactor volume, efficiency, conversion, and separation capabilities. An *incremental* improvement in conversion and separation often required a *significant* increase in reactor volume and a decrease in efficiency. Now, in a regenerative fuel processor, 100% of the fuel will eventually be converted to pure H_2 with only an *incremental* increase in reactor volume and *minimal* decrease in efficiency.

These features, demonstrated here in a highly specific example, are intrinsic to most energy conversion processes where CO_2 capture is designed as an integral part of the system (for example, [94]) rather than imposed as a burdensome afterthought. This change in perception provides an inroad for the introduction of CO_2 capture technology in the small-scale distributed/transportation sectors, eventually enabling the sustainable carbon economy.

Conclusions and Future Direction

A variety of options or pathways exist for eliminating carbon emissions from small, distributed sources such as the transportation sector. Of these, onboard/onsite carbon dioxide capture and storage has been shown to be a key driver towards a sustainable carbon economy. This approach is feasible if the local energy conversion device does not dilute the CO_2 byproduct. Many such systems exist and are the focus of ongoing research. Liquefaction of CO_2 provides a dense storage method for the byproduct; however, it also incurs an energy penalty. Additionally, it is shown that when small-scale energy conversion systems are designed to capture CO_2 emissions, the system is also able to take advantage of regenerative fuel processing.

To achieve widespread acceptance and demand for this technology, major technological improvements are needed in several areas including but not limited to:

- identification, development, and demonstration of advanced energy conversion processes that are amenable to distributed CO_2 capture
- highly scalable, novel reactor designs for small-scale, transient, distributed, and mobile applications

- cost effective catalysts and materials for the interconnects, electrodes, and electrolytes of fuel cells; improvements in efficiency, longevity, transient response, and power/weight/volume ratios of fuel cells for mobile applications
- catalysts with high activity and selectivity, and longevity of performance for distributed hydrogen generation from liquid fuels
- selectively permeable hydrogen, oxygen, and/or carbon dioxide membranes that are sufficiently robust to withstand realistic operating conditions—within a fuel reformer or in the presence of reformate species—without degrading performance and at a reasonable cost
- efficient systems for CO_2 compression and liquefaction, and materials for safe storage and transportation of pressurized liquid CO_2 on-board vehicles or from on-site distributed sources
- feasible and practical process development for recycling CO_2 into synthetic transportation fuels using only renewable primary energy input

Additionally, integration of individual processes through development of multi-functional components is critical to the scaling and packaging of a system that will fit "under the hood" or otherwise be convenient for the consumer. The cost of the system will be an important future concern as it needs to be competitive, not with today's polluting vehicles, but with the other available technologies for a sustainable, zero-carbon emission system.

APPENDIX B

MATLAB CODE FOR IDEAL CHAMP REACTOR MODEL

```
clc
clear
% ideal CHAMP reactor (no mass transfer)
% NOTE: variable total pressure
% kinetic model of Peppley, 1999 considers three simultaneous reactions:
% steam reforming, water gas shift, methanol decomposition

T = 523;   %temperature [K]
Pinit=1.0;   %total pressure [bar] or [atm]
R = 8.314; %gas constant [J/(mol-K)]

d = 0.0005;     %thickness of catalyst layer [m]
H_0=0.01;  %size of reactor [m]
L = 0.1;   %length of reactor [m]
rhocat=1300;    %density of catalyst [kg/m^3]
mcat = rhocat*d*L;    %mass of catalyst per unit depth [kg/m]
eps = 0.5;  %porosity of catalyst

Dmemb = 2.5e-7; %membrane diffusion coefficients [units for concentration]
del = 10.0e-6;   %membrane thickness [m]
CDinf = 1.0*101.3e3/(R*T);  %low side concentration of hydrogen [xP/RT]

deltat=0.002;   %size of time step
m=30000; %number of time steps

%%%%%%%%%%%%% Kinetic expressions &
parameters %%%%%%%%%%%%%%%%%%%%%%%%%%%%%%%%%%%%
ER=102.8e3; %activation energy [J/mol]
ED=170.0e3; %activation energy [J/mol]
EW=87.6e3;  %activation energy [J/mol]

kR=7.4e14*exp(-ER/(R*T));   %[m^2/(s-mol)]
kD=3.8e20*exp(-ED/(R*T));   %[m^2/(s-mol)]
kW=5.9e13*exp(-EW/(R*T));   %[m^2/(s-mol)]
CS1 = 7.5e-6; %Type 1 site concentrations [mol/m^2]
CS1a = 1.5e-5; %Type 1a site concentrations [mol/m^2]
CS2 = 7.5e-6; %Type 2 site concentrations [mol/m^2]
CS2a = 1.5e-5; %Type 2a site concentrations [mol/m^2]
SA = 102e3; %specific surface area of catalyst [m^2/kg]

%CH3O(1)
SCH3OI=-41.8;    %delta S [J/(mol-K)]
HCH3OI=-20.0e3;  %delta H [J/mol]
KCH3OI=exp(SCH3OI/R-HCH3OI/(R*T));
%HCOO
SHCOO=179.2;    %delta S [J/(mol-K)]
HHCOO=100.0e3;  %delta H [J/mol]
KHCOO=exp(SHCOO/R-HHCOO/(R*T));
%OH(1)
```

```
SOHI=-44.5;      %delta S [J/(mol-K)]
HOHI=-20.0e3;    %delta H [J/mol]
KOHI=exp(SOHI/R-HOHI/(R*T));
%H(1)
SHI=-100.8;     %delta S [J/(mol-K)]
HHI=-50.0e3;    %delta H [J/mol]
KHI=exp(SHI/R-HHI/(R*T));
%CH3O(2)
SCH3OII=30.0;    %delta S [J/(mol-K)]
HCH3OII=-20.0e3;  %delta H [J/mol]
KCH3OII=exp(SCH3OII/R-HCH3OII/(R*T));
%OH(2)
SOHII=30.0;      %delta S [J/(mol-K)]
HOHII=-20.0e3;    %delta H [J/mol]
KOHII=exp(SOHII/R-HOHII/(R*T));
%H(2)
SHII=-46.2;     %delta S [J/(mol-K)]
HHII=-50.0e3;    %delta H [J/mol]
KHII=exp(SHII/R-HHII/(R*T));
%K_R (steam reforming equilibrium constant)
SR=177.0;       %delta S [J/(mol-K)]
HR=49.2e3;      %delta H [J/mol]
KR=exp(SR/R-HR/(R*T));
%K_W (water gas shift equilibrium constant)
SW=-41.9;      %delta S [J/(mol-K)]
HW=-41.2e3;     %delta H [J/mol]
KW=exp(SW/R-HW/(R*T));
%K_D (decomposition equilibrium constant)
SD=219.0;      %delta S [J/(mol-K)]
HD=90.4e3;     %delta H [J/mol]
KD=exp(SD/R-HD/(R*T));
%%%%%%%%%%%%%%%%%%%%%%%%%%%%%%%%%%%%%%%%%%%%%%%%
%%%%%%%%%%%%%%%%%%%%%%%%%%%

%calculate partial pressures [bar] here
%A - methanol; B - water vapor; C - carbon dioxide; D - Hydrogen;
%F - carbon monoxide;
j=1;
nfuel=Pinit*101.3e3*(H_0+eps*d)*L/(R*T); %initial moles of fuel mix [mol/m]
nA(j)=0.5*nfuel;  %initial number of moles of methanol [mol/m]
nB(j)=0.5*nfuel;  %initial number of moles of water vapor [mol/m]
nC(j)=1.0e-8*nfuel;  %initial carbon dioxide
nD(j)=1.0e-8*nfuel;  %initial hydrogen
nF(j)=1.0e-8*nfuel;  %initial carbon monoxide

Ntot=nA(j)+nB(j)+nC(j)+nD(j)+nF(j);
xA(j)=nA(j)/Ntot;    %mole fraction of methanol
xB(j)=nB(j)/Ntot;    %mole fraction of water vapor
xC(j)=nC(j)/Ntot;    %mole fraction of carbon dioxide
xD(j)=nD(j)/Ntot;    %mole fraction of hydrogen
xF(j)=nF(j)/Ntot;    %mole fraction of carbon monoxide

PA=xA(j)*Pinit;  %partial pressure of methanol [bar]
PB=xB(j)*Pinit;
PC=xC(j)*Pinit;
```

```
PD=xD(j)*Pinit;
PF=xF(j)*Pinit;
PhiW(j)=0.0;
WFratio=0.0;

t(j)=0.0;
Ptot(j)=Pinit;
MeOH(j)=0.0;
Perm(j)=0.0;
Yield(j)=0.0;
Yieldrate(j)=0.0;
H(j)=H_0;
for j=1:m; %step forward in time

    %calculate rate expressions, rR, rW, rd
    rR=1 + KCH3OI*PA*PD^-0.5 + KHCOO*PC*PD^0.5 + KOHI*PB*PD^-0.5;
    rR=kR*KCH3OI*PA*PD^-0.5*(1-PD^3*PC/(KR*PA*PB))*CS1*CS1a/(rR*(1 + (KHI*PD)^0.5));

    rW=1 + KCH3OI*PA*PD^-0.5 + KHCOO*PC*PD^0.5 + KOHI*PB*PD^-0.5;
    rW=kW*KOHI*PF*PB*PD^-0.5*(1-PD*PC/(KW*PF*PB))*CS1^2/(rW)^2;

    rd=(1 + KCH3OII*PA*PD^-0.5 + KOHII*PB*PD^-0.5)*(1 + (KHII*PD)^0.5);
    rd=kD*KCH3OII*PA*PD^-0.5*(1-PD^2*PF/(KD*PA))*CS2*CS2a/rd;

    %rR*SA
    %rW*SA
    %rd*SA

    %calculate rate of production/consumption of each species
    rC=(rR+rW)*SA; %carbon dioxide production [mol/s-kg]
    rF=(rd-rW)*SA; %carbon monoxide production
    rA=-(rC+rF); %methanol consumption
    rB=-rC; %water vapor consumption
    rD=3*rC+2*rF; %hydrogen production

    CD=xD(j)*Ptot(j)*101.3e3/(R*T);    %hydrogen concentration in the reactor
    Jh(j)=L*Dmemb*(CD^0.5-CDinf^0.5)/del; %rate of hydrogen permeation [mol/m-s]

    %Jh(j)/L

    nA(j+1)=nA(j)+deltat*mcat*rA;   %moles of meth at future time step [mol/m]
    nB(j+1)=nB(j)+deltat*mcat*rB;
    nC(j+1)=nC(j)+deltat*mcat*rC;
    nD(j+1)=nD(j)+deltat*(mcat*rD-Jh(j));
    nF(j+1)=nF(j)+deltat*mcat*rF;

    MeOH(j+1)=(1-nA(j+1)/nA(1))*100;   %conversion of methanol
    Perm(j+1)=Perm(j)+deltat*Jh(j); %hydrogen permeated [mol/m]
    Yield(j+1)=Perm(j+1)/(3.0*nA(1))*100; %hydrogen yield efficiency
    t(j+1)=t(j)+deltat;
    time = t(j+1)
    %WFratio(j+1)=mcat*time*(1+MeOH(j+1)/100)/(nA(1)*0.5);
    %WFratio(j+1)=mcat*time/(nA(1)*0.44);
    WFratio(j+1)=mcat*time/(nA(1));
```

```
    Yieldrate(j+1)=Perm(j+1)/time;

    Ntot=nA(j+1)+nB(j+1)+nC(j+1)+nD(j+1)+nF(j+1);
    xA(j+1)=nA(j+1)/Ntot;    %mole fraction of methanol
    xB(j+1)=nB(j+1)/Ntot;    %mole fraction of water vapor
    xC(j+1)=nC(j+1)/Ntot;    %mole fraction of carbon dioxide
    xD(j+1)=nD(j+1)/Ntot;    %mole fraction of hydrogen
    xF(j+1)=nF(j+1)/Ntot;    %mole fraction of carbon monoxide

    Ptot(j+1)=Ntot*(R*T)/(L*(H(j)+eps*d)*101e3); %total pressure [bar]
    H(j+1)=H(j);
    if time > 3.0
       %H(j+1)=H(j)-0.0015*deltat; %drives the piston forward at 1 mm/s
    end
    if Ptot(j+1)<8.0
       Ptot(j+1)=8.0; %sets a minimum pressure at atmospheric
       H(j+1)=Ntot*R*T/(Ptot(j+1)*101e3*L)-eps*d;
    end
    PA=xA(j+1)*Ptot(j+1);  %partial pressure of methanol [bar]
    PB=xB(j+1)*Ptot(j+1);
    PC=xC(j+1)*Ptot(j+1);
    PD=xD(j+1)*Ptot(j+1);
    PF=xF(j+1)*Ptot(j+1);

    PhiW(j+1)=PC*PD/(PF*PB*KW);

    if Yield(j+1)>=91.0
       break %breaks when yield is at least x%
    end

    %deltat=deltat*(1.0005);
    %if deltat>0.01
    %    deltat=0.01;
    %end
end
Jh(j+1)=Jh(j);

results=[t(:) Yield(:) WFratio(:)];
%results=[t(:) xA(:) xB(:) xC(:) xD(:) xF(:)];
dlmwrite('results.txt',results,'precision','%.6f');
j
Fuelflow = nfuel/time %fuel flow rate for cycle [mol/m-s]
HYield = Perm(j+1)/time %hydrogen yield rate for cycle [mol/m-s]
```

APPENDIX C

EXPERIMENTAL SETUP DRAWINGS

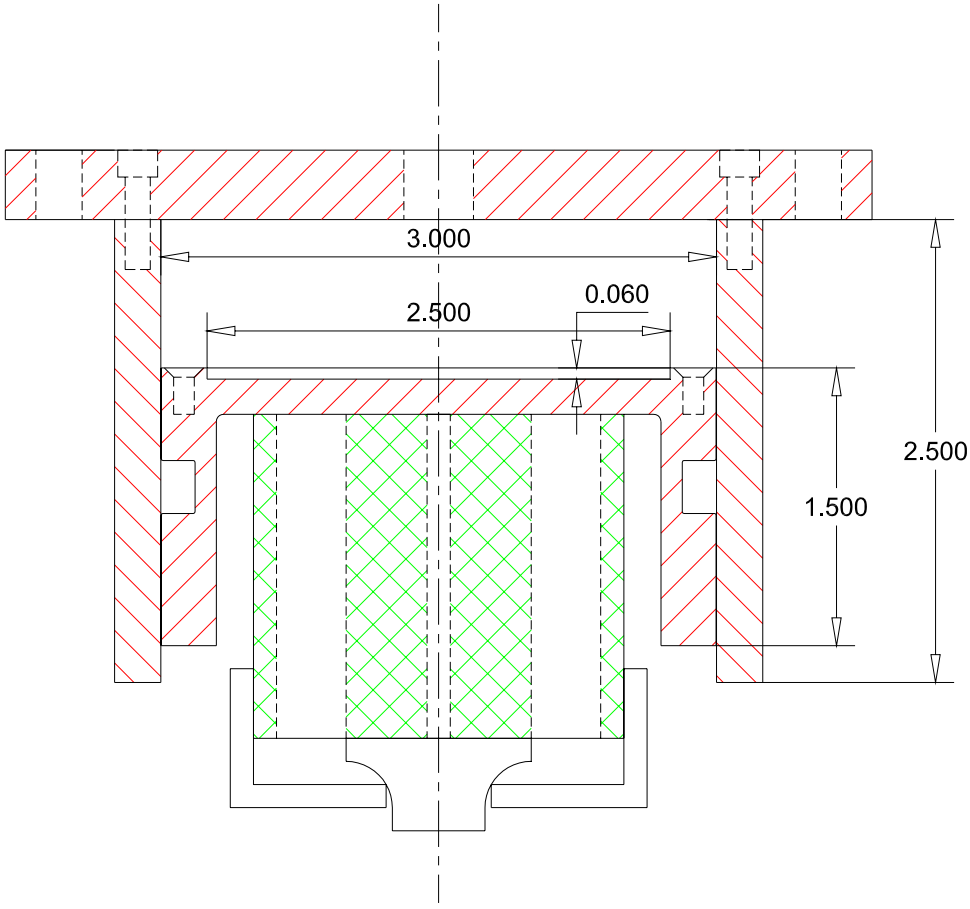

Figure C.1 Assembly view of the CHAMP reactor setup. All dimensions are in inches.

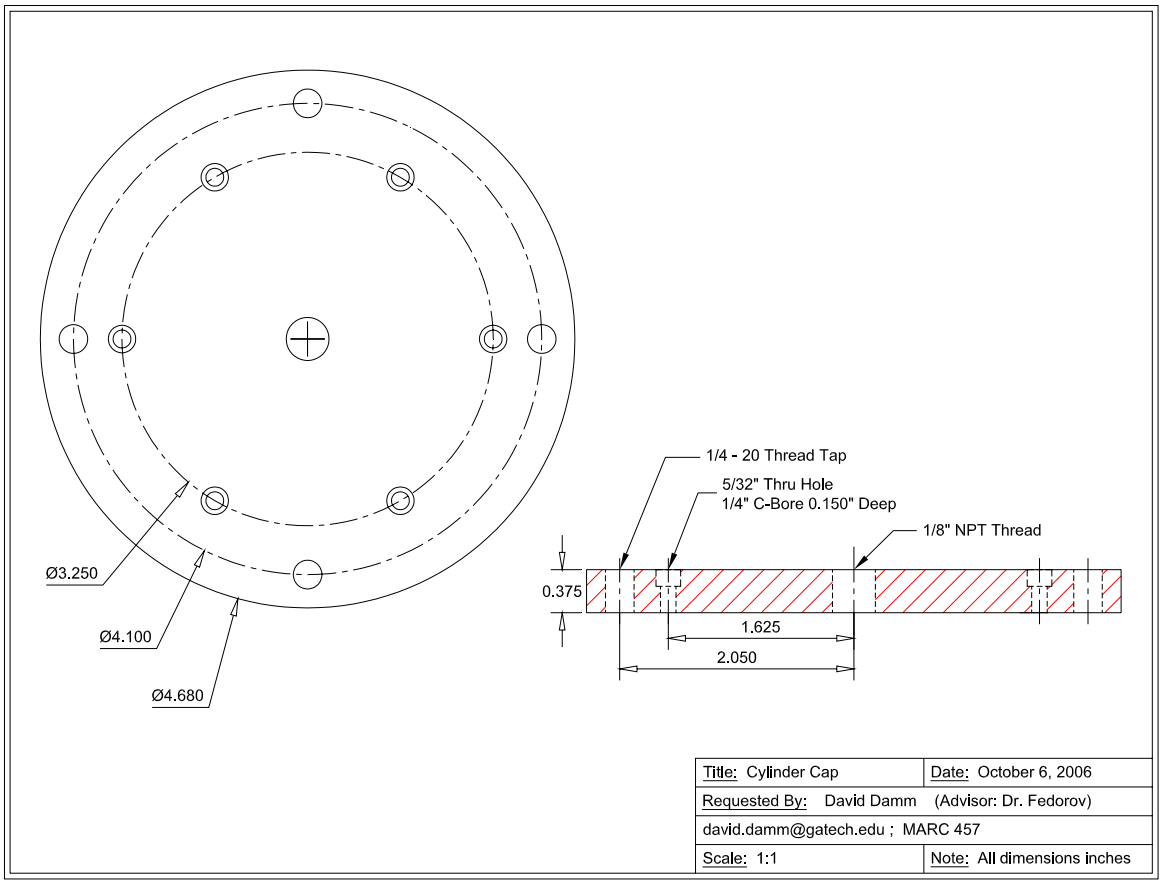

Figure C.2 Cylinder cap detail

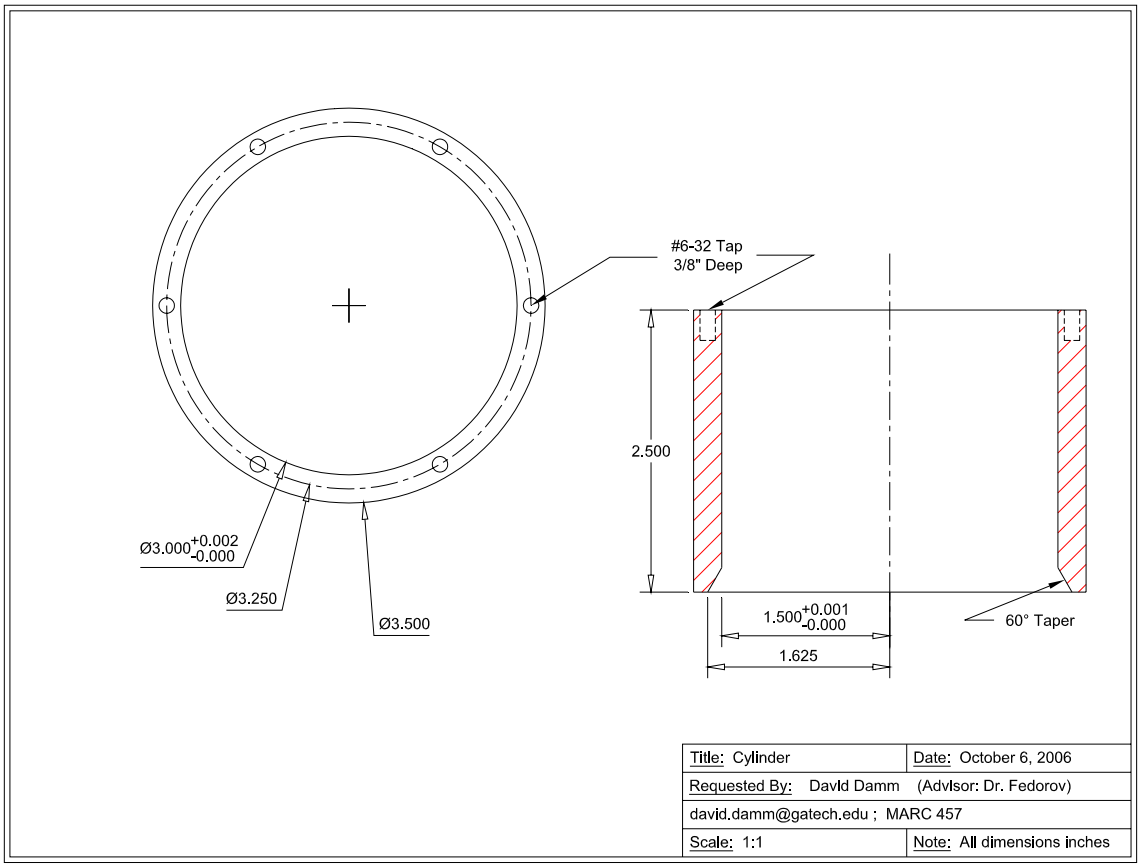

Figure C.3 Cylinder detail

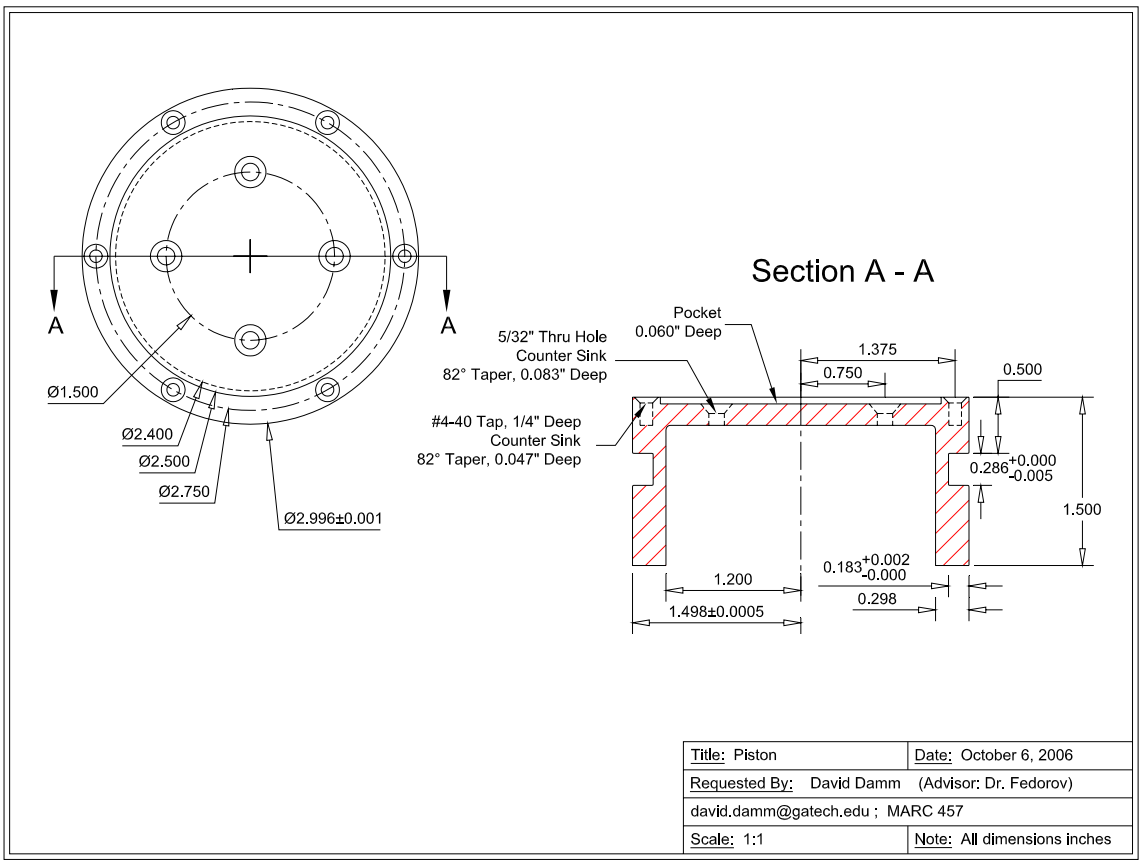

Figure C.4 Piston detail

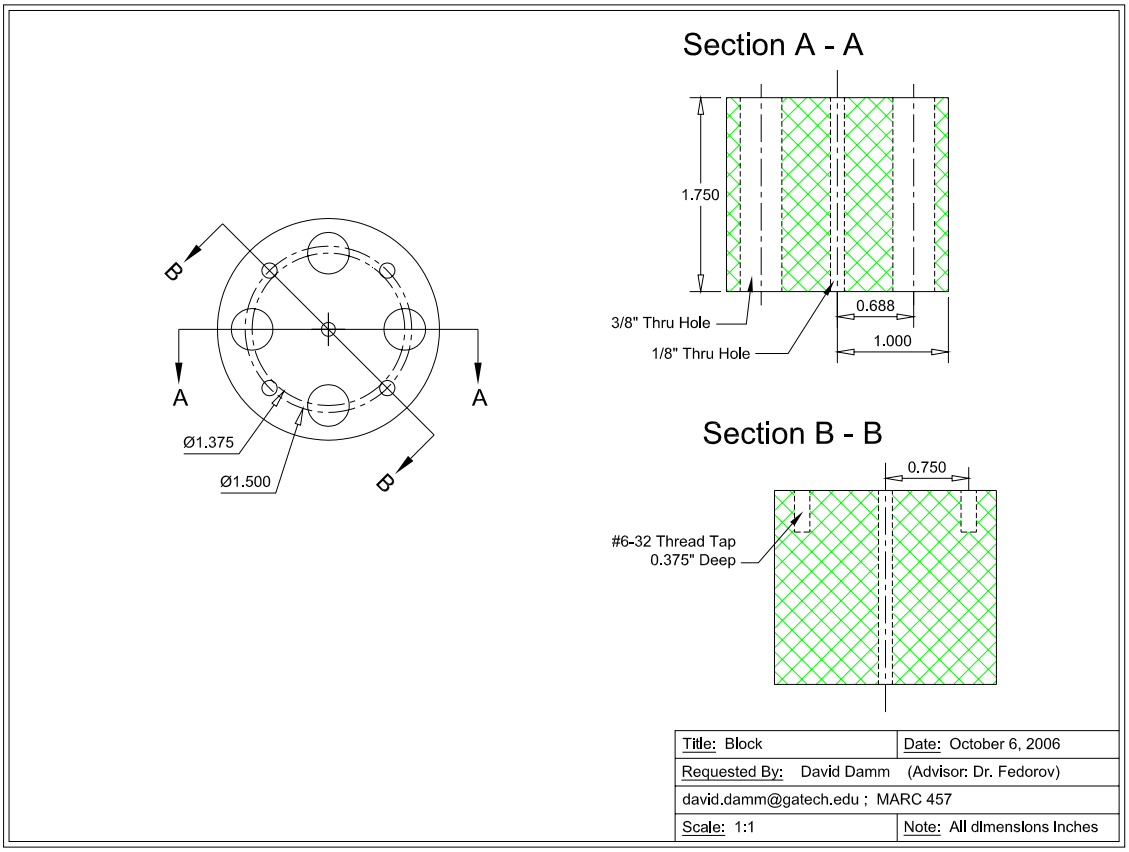

Figure C.5 Heater block detail

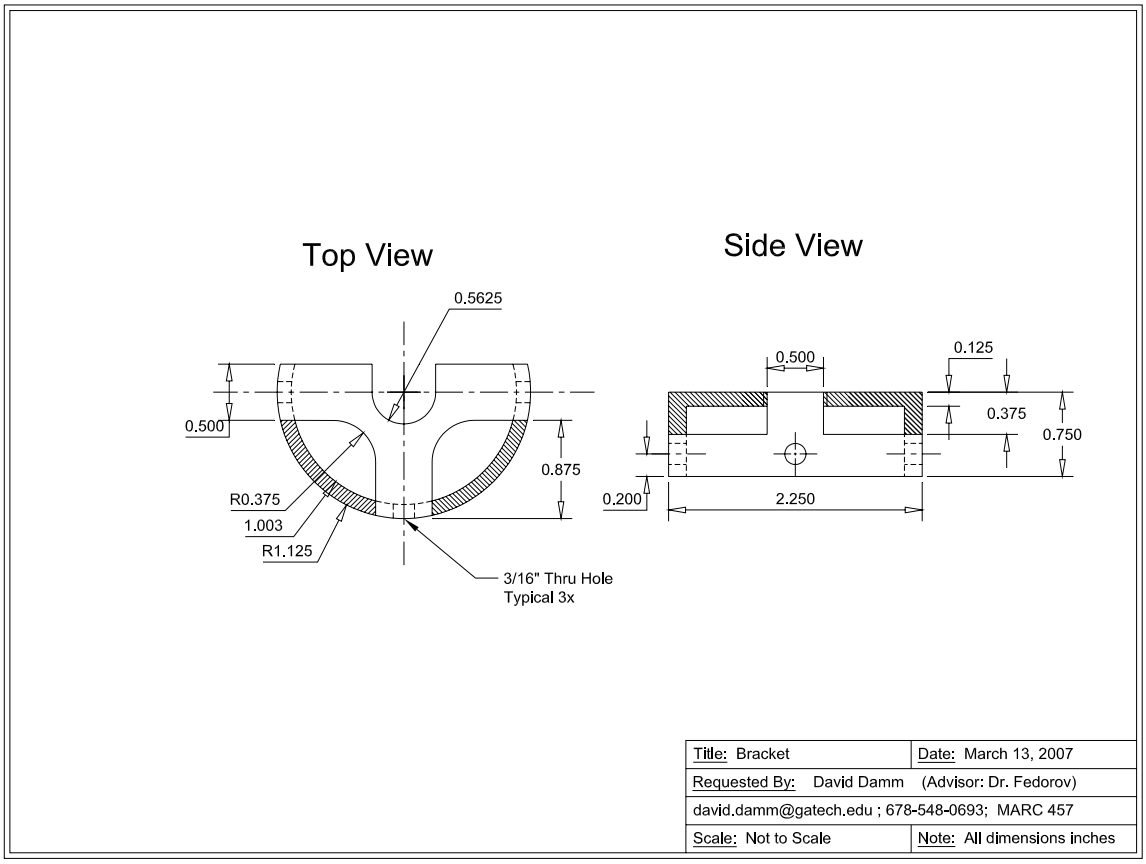

Figure C.6 Bracket detail

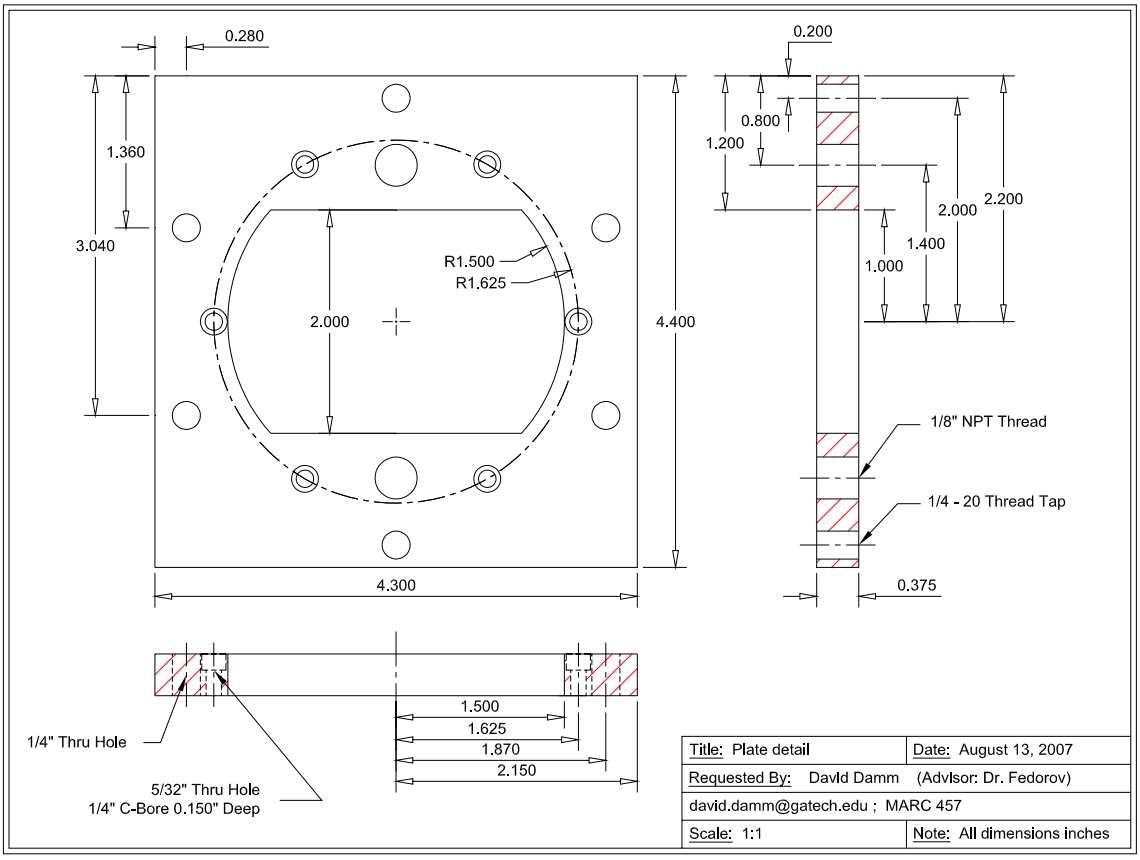

Figure C.7 Modified cylinder cap detail (for membrane reactor).

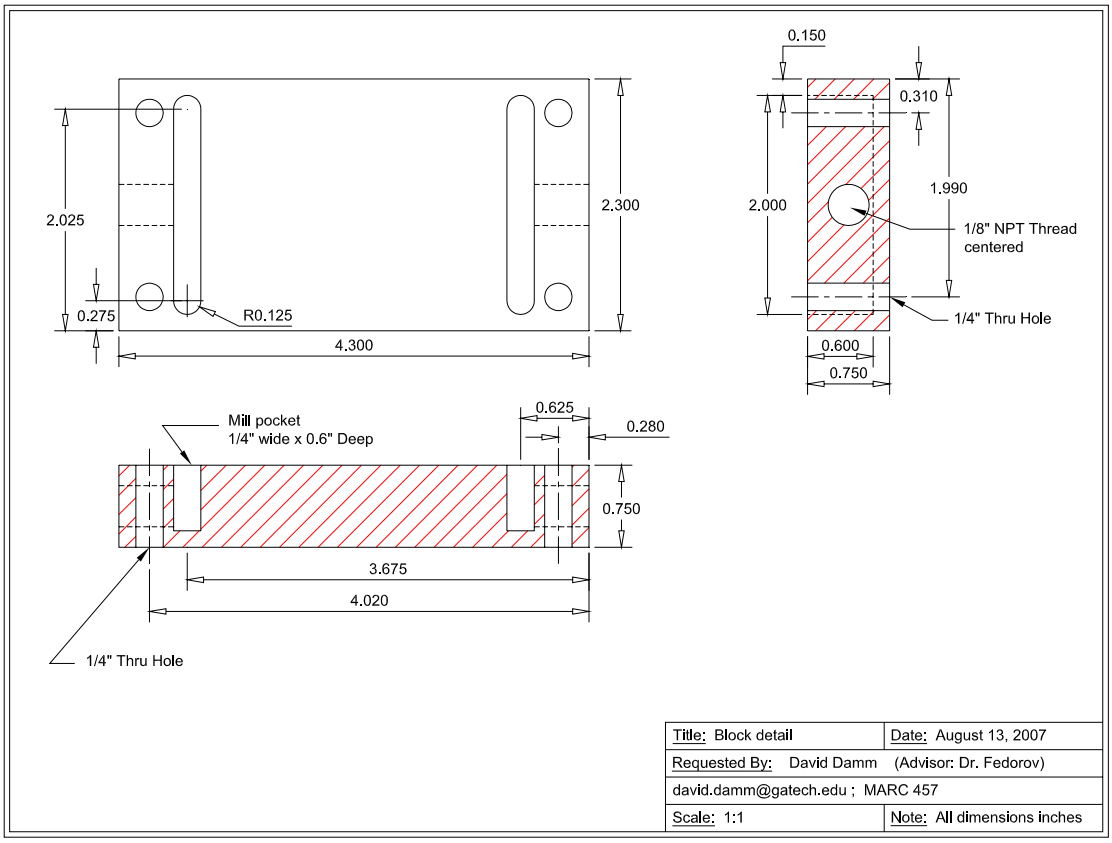

Figure C.8 Sweep gas manifold detail (for membrane reactor).

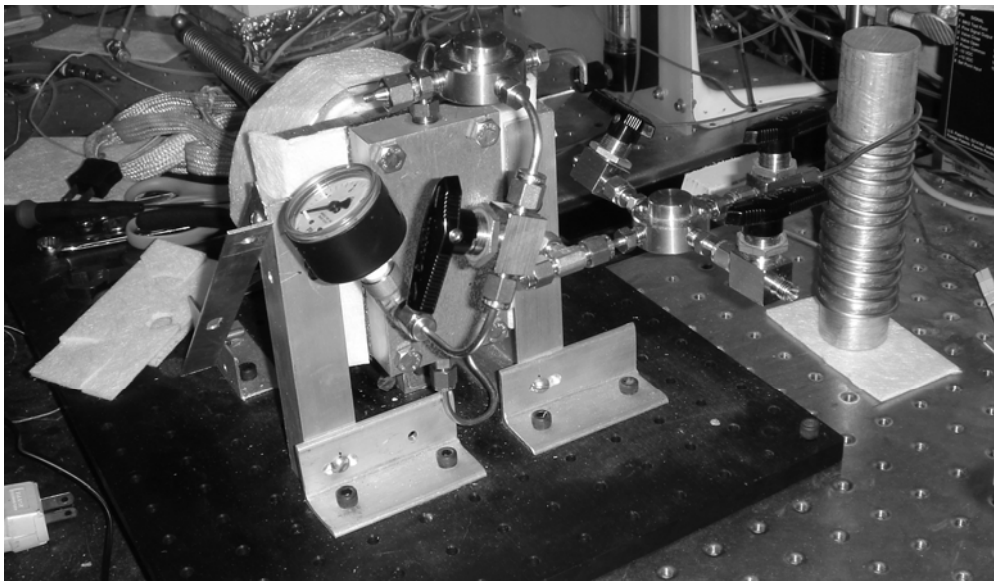

Figure C.9 Photograph of membrane reactor bench setup. Evaporator, valves, sweep gas manifold, and pressure gage are shown in this view. Insulation has been removed to show detail.

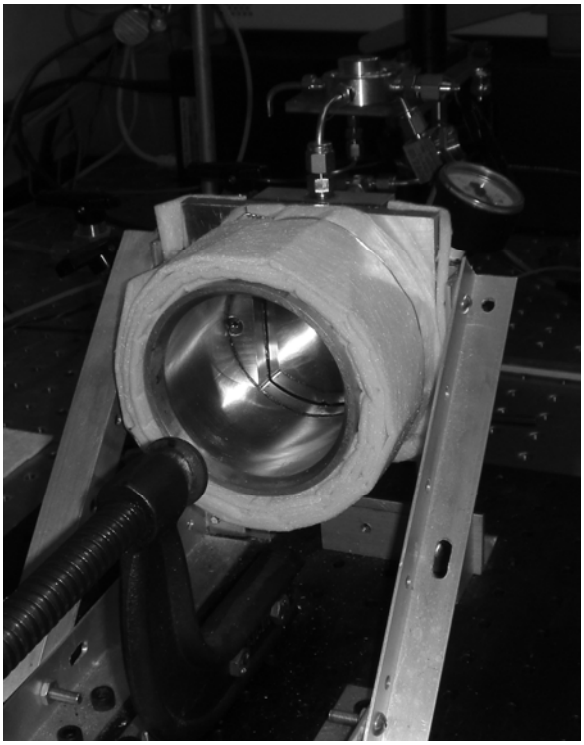

Figure C.10 Photograph of interior of cylinder of membrane reactor. At the top of the cylinder the palladium foil membrane can be seen.

APPENDIX D

EES EQUATIONS

```
//Step 1 (CO2 cooled by heat exchange with fuel mixture)
h1 = enthalpy(carbondioxide, T=250, P = 10)
S1a=Entropy (carbondioxide, T=95,P=10)
h1a=enthalpy(carbondioxide, T=95, P = 100)
heat1=h1-h1a

h1fuel = enthalpy(water, T=25,x=0)+enthalpy(methanol,T=25,x=0)
h2fuel = enthalpy(water, T=85,x=0)+enthalpy(methanol,T=85,x=0)
heatfuelsave1=h2fuel-h1fuel
//Note: temperatures are approximate; 1 mol of CO2 per 1 mol each of water and methanol

//Step 2 (CO2 compressed with 50% isentropic efficiency)
Ts = Temperature (carbondioxide, S=S1a, P = 100)
h2s = enthalpy(carbondioxide, T = Ts, P = 100)
h2=h1a+(h2s-h1a)/0.5
Treal=Temperature(carbondioxide, H=h2, P =100)

Work1=h2-h1a

//Step 3 (CO2 cooled by heat exchange with fuel mixture which begins to vaporize)
MeTsat=Temperature(methanol,P=10,x=1)
//Tsat = 137 C
H2OTsat=Temperature(water,P=10,x=1)
//Tsat = 180 C

h3=enthalpy(carbondioxide, T = 140, P = 100)
heat2 = h3-h2

h3fuel = enthalpy(water, T=140,x=0)+enthalpy(methanol,T=140,x=1)
heatfuelsave2 = h3fuel-h2fuel
//note: heat applied to the fuel by the CO2 cannot be greater than heat2
//fuel will not reach 140 C due to phase change, but CO2 may be cooled to 140 C

//Step 4 (CO2 cooled by heat exchange with ambient)
h4 = enthalpy(Carbondioxide,T=25,P = 100)
heat3 = h4-h3
```

REFERENCES

1. White C. M., Steeper R. R., et al. (2006). "The hydrogen-fueled internal combustion engine: a technical review." International Journal of Hydrogen Energy **31**(10): 1292-1305.

2. (2000). Fuel Cell Handbook (5th Ed.), EG&G Services, National Technical Information Service, U.S. Dept. of Commerce.

3. Demirbas M. F. (2006). "Technological options for producing hydrogen from renewable resources." Energy Sources Part a-Recovery Utilization and Environmental Effects **28**(13): 1215-1223.

4. Gratzel M. (2005). "Mesoscopic solar cells for electricity and hydrogen production from sunlight." Chemistry Letters **34**(1): 8-13.

5. Ewan B. C. R. and Allen R. W. K. (2005). "A figure of merit assessment of the routes to hydrogen." International Journal of Hydrogen Energy **30**(8): 809-819.

6. Turner J. A. (2004). "Sustainable hydrogen production." Science **305**(5686): 972-974.

7. Schultz K. R. (2003). "Production of hydrogen by fusion energy: A review and perspective." Fusion Science and Technology **44**(2): 393-399.

8. Stiegel G. J. and Ramezan M. (2006). "Hydrogen from coal gasification: An economical pathway to a sustainable energy future." International Journal of Coal Geology **65**(3-4): 173-190.

9. Rice W. (2006). "Hydrogen production from methane hydrate with sequestering of carbon dioxide." International Journal of Hydrogen Energy **31**(14): 1955-1963.

10. Azar C., Lindgren K., et al. (2003). "Global energy scenarios meeting stringent CO_2 constraints--cost-effective fuel choices in the transportation sector." Energy Policy **31**: 961-976.

11. McNicol B. D., Rand D. A. J., et al. (2001). "Fuel cells for road transportation purposes -- yes or no?" Journal of Power Sources **100**: 47-59.

12. Ogden J. M., Steinbugler M. M., et al. (1999). "A comparison of hydrogen, methanol and gasoline as fuels for fuel cell vehicles: implications for vehicle design and infrastructure development." Journal of Power Sources **79**(2): 143-168.

13. Satyapal S., Petrovic J., et al. (2007). "The US Department of Energy's National Hydrogen Storage Project: Progress towards meeting hydrogen-powered vehicle requirements." Catalysis Today **120**(3-4): 246-256.

14. Defense U. S. D. o. (2008). "DDR&E Prize Website." 2008, from http://www.dod.mil/ddre/prize/.

15. Halmann M. M. and Steinberg M. (1999). Greenhouse gas carbon dioxide mitigation: science and technology. Boca Raton, FL, Lewis Publishers.

16. Damm D. L. and Fedorov A. G. (2008). "Conceptual study of distributed CO_2 capture and the sustainable carbon economy." Energy Conversion & Management **49**: 1674-1683.

17. Fedorov A. G. and Damm D. L. Hydrogen-Generating Reactors and Methods, U.S. Patent App. 11/708,772, Filed on 02/21/2007.

18. Damm D. L. and Fedorov A. G. (2008). "Comparative assessment of batch reactors for scalable hydrogen production." Industrial & Engineering Chemistry Research **in press**.

19. Edwards N., Ellis S. R., et al. (1998). "On-board hydrogen generation for transport applications: the HotSpot^{TM} methanol processor." Journal of Power Sources **71**(1-2): 123-128.

20. Uemiya S. (2004). "Brief review of steam reforming using a metal membrane reactor." Topics in Catalysis **29**(1-2): 79-84.

21. Lattner J. R. and Harold M. P. (2005). "Comparison of methanol-based fuel processors for PEM fuel cell systems." Applied Catalysis B-Environmental **56**(1-2): 149-169.

22. Wang L. S., Murata K., et al. (2005). "Steam reforming of gasoline promoted by partial oxidation reaction on novel bimetallic Ni-based catalysts to generate hydrogen for fuel cell-powered automobile applications." Journal of Power Sources **145**(2): 707-711.

23. Haryanto A., Fernando S., et al. (2005). "Current status of hydrogen production techniques by steam reforming of ethanol: A review." Energy & Fuels **19**(5): 2098-2106.

24. Schmidt V. M., Brockerhoff P., et al. (1994). "Utilization of Methanol for Polymer Electrolyte Fuel-Cells in Mobile Systems." Journal of Power Sources **49**(1-3): 299-313.

25. Christiansen J. A. (1921). "A reaction between methyl alcohol and water and some related reactions." Journal of the American Chemical Society **43**: 1670.

26. Huang J., El-Azzami L., et al. (2005). "Modeling of CO2-selective water gas shift membrane reactor for fuel cell." Journal of Membrane Science **261**(1-2): 67-75.

27. Agrell J., Birgersson H., et al. (2002). "Steam reforming of methanol over a $Cu/ZnO/Al_2O_3$ catalyst: a kinetic analysis and strategies for suppression of CO formation." Journal of Power Sources **106**(1-2): 249-257.

28. Prasad P. and Elnashaie S. S. E. H. (2004). "Novel circulating fluidized-bed membrane reformer using carbon dioxide sequestration." Industrial & Engineering Chemistry Research **43**(2): 494-501.

29. Yu X. H., Tu S. T., et al. (2005). "On-board production of hydrogen for fuel cells over $Cu/ZnO/Al_2O_3$ catalyst coating in a micro-channel reactor." Journal of Power Sources **150**: 57-66.

30. Cao C. S., Xia G., et al. (2004). "Kinetic studies of methanol steam reforming over Pd/ZnO catalyst using a microchannel reactor." Applied Catalysis a-General **262**(1): 19-29.

31. Fukuhara C., Ohkura H., et al. (2004). "Catalytic properties of plate-type copper-based catalysts, for steam reforming of methanol, on an aluminum plate prepared by electroless plating." Applied Catalysis a-General **273**(1-2): 125-132.

32. Fukuhara C., Kamata Y., et al. (2005). "Catalytic performance of microtube-type copper-based catalyst for methanol steam reforming, prepared on the inner wall of an aluminum tube by electroless plating." Applied Catalysis a-General **296**(1): 100-107.

33. Karim A., Bravo J., et al. (2005). "Comparison of wall-coated and packed-bed reactors for steam reforming of methanol." Catalysis Today **110**(1-2): 86-91.

34. Wild P. J. d. and Verhaak M. J. F. M. (2000). "Catalytic production of hydrogen from methanol." Catalysis Today **60**: 3-10.

35. Pan L. W. and Wang S. D. (2005). "Methanol steam reforming in a compact plate-fin reformer for fuel-cell systems." International Journal of Hydrogen Energy **30**(9): 973-979.

36. Pan L. W. and Wang S. D. (2005). "Modeling of a compact plate-fin reformer for methanol steam reforming in fuel cell systems." Chemical Engineering Journal **108**(1-2): 51-58.

37. Lim M. S., Kim M. R., et al. (2005). "A plate-type reactor coated with zirconia-sol and catalyst mixture for methanol steam-reforming." Journal of Power Sources **140**(1): 66-71.

38. Take T., Yachi T., et al. (2003). "Development of plate-fin-type methanol reformer." Journal of Chemical Engineering of Japan **36**(1): 75-80.

39. Gallucci F., Paturzo L., et al. (2004). "Hydrogen recovery from methanol steam reforming in a dense membrane reactor: Simulation study." Industrial & Engineering Chemistry Research **43**(10): 2420-2432.

40. Kleinert A., Grubert G., et al. (2005). "Compatibility of hydrogen transfer via Pd-membranes with the rates of heterogeneously catalysed steam reforming." Catalysis Today **104**(2-4): 267-273.

41. Lin Y. M. and Rei M. H. (2001). "Study on the hydrogen production from methanol steam reforming in supported palladium membrane reactor." Catalysis Today **67**(1-3): 77-84.

42. Lin Y. M., Lee G. L., et al. (1998). "An integrated purification and production of hydrogen with a palladium membrane-catalytic reactor." Catalysis Today **44**(1-4): 343-349.

43. Itoh N., Kaneko Y., et al. (2002). "Efficient hydrogen production via methanol steam reforming by preventing back-permeation of hydrogen in a palladium membrane reactor." Industrial & Engineering Chemistry Research **41**(19): 4702-4706.

44. Rei B. M. H., Yeh G. T., et al. (2004). "Catalysis-spillover-membrane-2 - The rate enhancement of methanol steam reforming reaction in a membrane catalytic reactor." Catalysis Today **97**(2-3): 167-172.

45. Adhikari S. and Fernando S. (2006). "Hydrogen membrane separation techniques." Industrial & Engineering Chemistry Research **45**(3): 875-881.

46. Cheng Y. S., Pena M. A., et al. (2002). "Performance of alumina, zeolite, palladium, Pd-Ag alloy membranes for hydrogen separation from Towngas mixture." Journal of Membrane Science **204**: 329-340.

47. van de Graaf J. M., van der Bijl E., et al. (1998). "Effect of operating conditions and membrane quality on the separation performance of composite silicalite-1 membranes." Industrial & Engineering Chemistry Research **37**: 4071-4083.

48. Leung Y. L. A. and Yeung K. L. (2004). "Microfabricated ZSM-5 zeolite micromembranes." Chemical Engineering Science **59**: 4809-4817.

49. McLeod L., Degertekin F. L., et al. (2005). Analysis of hydrogen permeation through sub-micron thick palladium alloy membranes. ASME Summer Heat Transfer Conference, San Franscisco, CA, USA.

50. Keurentjes J. T. F., Gielens F. C., et al. (2004). "High-flux palladium membranes based on microsystem technology." Industrial & Engineering Chemistry Research **43**: 4768-4772.

51. McLeod L. S., Degertekin F. L., et al. (2007). "Effect of microstructure on hydrogen permeation through thermally stable, sputtered palladium-silver alloy membranes." Applied Physics Letters **90**(26): 261905.

52. Harold M. P., Nair B., et al. (2003). "Hydrogen generation in a Pd membrane fuel processor: assessment of methanol-based reaction systems." Chemical Engineering Science **58**(12): 2551-2571.

53. Matros Y. S. (1996). "Forced unsteady-state processes in heterogeneous catalytic reactors." The Canadian Journal of Chemical Engineering **74**: 566-579.

54. Kikas T., Bardenshteyn I., et al. (2003). "Hydrogen Production in a Reverse-Flow Autothermal Catalytic Microreactor: From Evidence of Performance Enhancement to Innovative Reactor Design." Industrial & Engineering Chemistry Research **42**(25): 6273-6279.

55. Kaisare N. S., Lee J. H., et al. (2005). "Hydrogen generation in a reverse-flow microreactor: 1. Model formulation and scaling." Aiche Journal **51**(8): 2254-2264.

56. Kaisare N. S., Lee J. H., et al. (2005). "Operability analysis and design of a reverse-flow microreactor for hydrogen generation via methane partial oxidation." Industrial & Engineering Chemistry Research **44**(22): 8323-8333.

57. Kaisare N. S., Lee J. H., et al. (2005). "Hydrogen generation in a reverse-flow microreactor: 2. Simulation and analysis." Aiche Journal **51**(8): 2265-2272.

58. Johannessen E. and Jordal K. (2005). "Study of a H-2 separating membrane reactor for methane steam reforming at conditions relevant for power processes with CO2 capture." Energy Conversion and Management **46**(7-8): 1059-1071.

59. Barbieri G., Violante V., et al. (1997). "Methane steam reforming analysis in a palladium-based catalytic membrane reactor." Industrial & Engineering Chemistry Research **36**(8): 3369-3374.

60. Shu J., Grandjean B. P. A., et al. (1994). "Methane Steam Reforming in Asymmetric Pd-Ag and Pd-Ag/Porous Ss Membrane Reactors." Applied Catalysis a-General **119**(2): 305-325.

61. Peppley B. A., Amphlett J. C., et al. (1999). "Methanol-steam reforming on $Cu/ZnO/Al_2O_3$ catalysts. Part 2. A comprehensive kinetic model." Applied Catalysis a-General **179**(1-2): 31-49.

62. Jiang C. J., Trimm D. L., et al. (1993). "Kinetic Mechanism for the Reaction between Methanol and Water over a $Cu\text{-}ZnO\text{-}Al_2O_3$ Catalyst." Applied Catalysis a-General **97**(2): 145-158.

63. Jiang C. J., Trimm D. L., et al. (1993). "Kinetic-Study of Steam Reforming of Methanol over Copper-Based Catalysts." Applied Catalysis a-General **93**(2): 245-255.

64. Idem R. O. and Bakhshi N. N. (1996). "Kinetic modeling of the production of hydrogen from the methanol-steam reforming process over Mn-promoted coprecipitated Cu-Al catalyst." Chemical Engineering Science **51**(14): 3697-3708.

65. Peppley B. A., Amphlett J. C., et al. (1999). "Methanol-steam reforming on $Cu/ZnO/Al_2O_3$. Part 1: The reaction network." Applied Catalysis a-General **179**(1-2): 21-29.

66. Asprey S. P., Wojciechowski B. W., et al. (1999). "Kinetic studies using temperature-scanning: the steam-reforming of methanol." Applied Catalysis a-General **179**(1-2): 51-70.

67. Lee J. K., Ko J. B., et al. (2004). "Methanol steam reforming over $Cu/ZnO/Al_2O_3$ catalyst: kinetics and effectiveness factor." Applied Catalysis a-General **278**(1): 25-35.

68. Mastalir A., Frank B., et al. (2005). "Steam reforming of methanol over $Cu/ZrO_2/CeO_2$ catalysts: a kinetic study." Journal of Catalysis **230**(2): 464-475.

69. Choi Y. T. and Stenger H. G. (2005). "Kinetics, simulation and optimization of methanol steam reformer for fuel cell applications." Journal of Power Sources **142**(1-2): 81-91.

70. Pfeifer P., Kolbl A., et al. (2005). "Kinetic investigations on methanol steam reforming on PdZn catalysts in microchannel reactors and model transfer into the pressure gap region." Catalysis Today **110**(1-2): 76-85.

71. Agarwal V., Patel S., et al. (2005). "H_2 production by steam reforming of methanol over $Cu/ZnO/Al_2$ catalysts: transient deactivation kinetics modeling." Applied Catalysis a-General **279**(1-2): 155-164.

72. Pattekar A. V. and Kothare M. V. (2004). "A microreactor for hydrogen production in micro fuel cell applications." Journal of Microelectromechanical Systems **13**(1): 7-18.

73. Tonkovich A. Y., Zilka J. L., et al. (1999). "Microchannel reactors for fuel processing applications. I. Water gas shift reactor." Chemical Engineering Science **54**(13-14): 2947-2951.

74. Hines A. L. and Maddox R. N. (1985). Mass Transfer Fundamentals and Applications. Englewood Cliffs, New Jersey, Prentice-Hall, Inc.

75. Press W., Teukolsky S., et al. (1995). Numerical Recipes in C. New York, Cambridge University Press.

76. McLeod L. (2008) Woodruff School of Mechanical Engineering, Georgia Institute of Technology.

77. Amandusson H., Ekedahl L. G., et al. (2000). "The effect of CO and O2 on hydrogen permeation through a palladium membrane." Applied Surface Science **153**: 259-267.

78. Chabot J., Lecomte J., et al. (1988). "Fuel clean-up system: poisoning of palladium-silver membranes by gaseous impurities." Fusion Technology **14**: 614-618.

79. Peters T. A., Stange M., et al. "High pressure performance of thin Pd-23%Ag/stainless steel composite membranes in water gas shift gas mixtures; influence of dilution, mass transfer and surface effects on the hydrogen flux." Journal of Membrane Science **In Press**.

80. (2001). Climate Change 2001: The scientific basis, Intergovernmental Panel on Climate Change.

81. O'Neill B. C. and Oppenheimer M. (2002). "Climate Change: Dangerous Climate Impacts and the Kyoto Protocol." Science **296**(5575): 1971-1972.

82. Hasselmann K., Latif M., et al. (2003). "The Challenge of Long-Term Climate Change." Science **302**(5652): 1923-1925.

83. Hoffert M. I., Caldeira K., et al. (2002). "Advanced Technology Paths to Global Climate Stability: Energy for a Greenhouse Planet." Science **298**(5595): 981-987.

84. (2003). Geologic sequestration of carbon dioxide - An energy resource perspective. USGS Fact Sheet FS-026-03, United States Geological Survey.

85. (1999). Carbon sequestration research and development, United States Department of Energy.

86. Lackner K. S. (2002). "Carbonate chemistry for sequestering fossil carbon." Annual Review of Energy and Environment **27**: 193-232.

87. (2005). Carbon Sequestration Technology Roadmap and Program Plan, United States Department of Energy.

88. Kreith F. and West R. E. (2004). "Fallacies of a Hydrogen Economy: A critical analysis of hydrogen production and utilization." Journal of Energy Resources Technology **126**: 249-257.

89. West R. E. and Kreith F. (2006). "A vision for a secure transportation system without hydrogen or oil." Journal of Energy Resources Technology **128**: 236-243.

90. Van Mierlo J., Maggetto G., et al. (2006). "Which energy source for road transport in the future? A comparison of battery, hybrid and fuel cell vehicles." Energy Conversion and Management **47**(17): 2748-2760.

91. Fernando S., Adhikari S., et al. (2006). "Biorefineries: Current status, challenges, and future direction." Energy & Fuels **20**(4): 1727-1737.

92. Lackner K. S. (2003). "A Guide to CO2 Sequestration." Science **300**: 1677-1678.

93. Golomb D. S. (2003). "Issues of carbon sequestration." Science **301**(5638): 1326-1326.

94. Kato Y., Otsuka K., et al. (2005). "Carbon dioxide zero-emission hydrogen carrier system for fuel cell vehicle." Chemical Engineering Research & Design **83**(A7): 900-904.

95. Kato Y., Ando K., et al. (2003). "Study on a regenerative fuel reformer for a zero-emission vehicle system." Journal of Chemical Engineering of Japan **36**(7): 860-866.

96. Rozovskii A. Y. and Lin G. I. (2003). "Fundamentals of methanol synthesis and decomposition." Topics in Catalysis **22**(3-4): 137-150.

97. Steinfeld A. and Palumbo R. (2001). Solar Thermochemical Process Technology. Encyclopedia of Physical Science & Technology. R. A. Meyers, Academic Press. **15:** 237-256.

98. Bredesen R., Jordal K., et al. (2004). "High temperature membranes in power generation with CO2 capture." Chemical Engineering and Processing **43**: 1129-1158.

99. Bouwmeester H. J. M. (2003). "Dense ceramic membranes for methane conversion." Catalysis Today **82**: 141-150.

100. Lide D. R., Ed. (1995). CRC Handbook of Chemistry and Physics. New York, CRC Press.

101. Span R. and Wagner W. (1996). "A new equation of state for carbon dioxide covering the fluid region from the triple point temperature to 1100 K at pressures up to 800 MPa." Journal of Physical and Chemical reference data **25**(6).

102. Moran M. J. and Shapiro H. N. (2000). Fundamentals of Engineering Thermodynamics. New York, John Wiley and Sons.

103. Basile A., Gallucci F., et al. (2005). "A dense Pd/Ag membrane reactor for methanol steam reforming: Experimental study." Catalysis Today **104**(2-4): 244-250.

104. Wieland S., Melin T., et al. (2002). "Membrane reactors for hydrogen production." Chemical Engineering Science **57**(9): 1571-1576.